

Electrohydrodynamic Enhancement of Extraterrestrial Capillary Pumped Loops for Nuclear Applications

By

Adam Lipchitz

**A Thesis Submitted in Partial Fulfillment of the Requirements for the
Degree of**

Master of Applied Science

In

The Faculty of Energy Systems and Nuclear Science

Nuclear Engineering

University of Ontario Institute of Technology

December, 2010

© Adam Lipchitz, 2010

Abstract

This work examines electrohydrodynamic enhancement of capillary pump loops (CPL) for use in extraterrestrial nuclear applications. A capillary pump uses capillary action through a porous wick to transport heat and mass. The capillary pump is being considered as a method to improve heat transport in extraterrestrial nuclear applications. The work consists of a literature review of electrohydrodynamics, capillary pumped loops and space type nuclear reactors. Current CPLs are assessed for their performance and several design solutions are investigated using theoretical and analytical techniques. Experimental analysis is performed on an electrohydrodynamic gas pump to determine their suitability for implementation into the vapour leg of a capillary pump loop. The results suggest the EHD gas pumps could offer improved performance and it is recommended experiments should be performed in future work with an EHD gas pump in a CPL for verification. A new design for the electrohydrodynamic evaporator is also developed for enhanced performance.

KEYWORDS: Heat Transfer, Electrohydrodynamics, Capillary Pump Loops, Capillary Action, Extraterrestrial, Outer Space, Nuclear, Gas Pumps

Acknowledgments

This thesis could not be completed without the hard work, patience and support of numerous individuals. To all of you I am extremely grateful.

To Dr. Jen-Shih Chang for all of your advice, guidance and considerable help with all things electrohydrodynamic and for graciousness in allowing the use of your laboratory equipment for experimental work. Without your help this project would not be possible.

To Dr. Nozomi Takeuchi for his high voltage and electrohydrodynamic safety training and for his help in guiding the design of the gas pump experiments

To all the members of the nuclear design laboratory research group current and former for their support in group meetings and for lending the occasional hand when needed.

Lastly and most of all I would like to acknowledge my supervisor, Dr. Glenn Harvel for all of your guidance, support and understanding throughout this whole experience and possibly even more importantly thank you for providing me with this opportunity and for me introducing me to the world of electrohydrodynamics.

Table of Contents

| | |
|---|----|
| 1. Introduction..... | 1 |
| 1.1 EHD Devices..... | 3 |
| 1.2 EHD Forces | 5 |
| 1.3 Objective | 7 |
| 2. Literature Review | 8 |
| 2.1 Nuclear Reactors for Outer Space and Extraterrestrial Applications..... | 8 |
| 2.2 Capillary Pumped Loops | 17 |
| 2.3 Capillary Pumped Loops with an EHD Enhanced Evaporator..... | 19 |
| 2.4 Electrohydrodynamic gas pumps | 21 |
| 3. Theory of EHD Enhanced Capillary Pumped Loops..... | 25 |
| 3.1 Capillary Pumped Loop..... | 25 |
| 3.2 EHD Enhanced Capillary Pumped Loop Previous Modifications and Design Issues | 29 |
| 3.3 Electrohydrodynamics..... | 30 |
| 4. EHD Capillary Pumped Loop Design | 39 |
| 4.1 Current Capillary Pumped Loop Design..... | 39 |
| 4.2 Experimental Analysis of Capillary Pumped Loop..... | 42 |
| 4.3 Evaporator Design | 46 |
| 4.3.1 Evaporator Wick | 46 |
| 4.3.2 Evaporator Electrode Design..... | 52 |
| 4.4 Vapour Leg and Condenser | 57 |
| 4.4.1 Cooling Jacket..... | 57 |
| 4.5 EHD Gas Pump | 59 |
| 5. EHD Gas Pump Experimental Apparatus..... | 64 |
| 6. EHD Gas Pump Experimental Study | 76 |
| 6.1 Experimental Details | 76 |
| 6.2 Gas Pump Heat Generation Analysis | 79 |
| 6.3 EHD Gas Pump Characterization | 83 |
| 6.4 Copper Electrode Experiments | 88 |

| | |
|--|-----|
| 6.5 EHD Gas Pump Orientation Effect | 93 |
| 6.6 EHD Gas Pump Humidity Effect | 97 |
| 6.7 Ambient Temperature Effect | 100 |
| 6.8 Effect of Ehd Number..... | 102 |
| 6.9 Free Convection Flow and Temperature Profiles..... | 104 |
| 6.10 Forced Convection Flow Profile | 113 |
| 6.11 EHD Gas Pump for Freon Loop | 115 |
| 7. Concluding Remarks | 116 |
| 8. Recommendations for Future Work..... | 118 |
| 9. References | 119 |

List of Figures

| | |
|--|----|
| Figure 1.1: Heat Flow diagram for a CPL | 4 |
| Figure 1.2: Diagram of EHD forces and their effect on ions in the presence of an electric field..... | 6 |
| Figure 2.1: Concept design of a nuclear power plant for support of a space based facility [12] | 10 |
| Figure 2.2: Concept for a Pebble bed type space reactor for propulsion [34]..... | 11 |
| Figure 2.3: Schematic of the SAIRS concept reactor [34] | 14 |
| Figure 2.4: Schematic of the HP–STMCs concept reactor [34] | 14 |
| Figure 2.5: Schematic of the SCoRe S11 concept reactor [34] | 15 |
| Figure 2.6: Schematic of the S ⁴ CBC concept reactor [34]..... | 15 |
| Figure 2.7: Schematic of the Sterling Engine Reactor concept [12]..... | 16 |
| Figure 2.8: Lithium heat pipe for a HP-STMCs [11] | 16 |
| Figure 2.9: Diagram of inside of the evaporator..... | 20 |
| Figure 2.10: Schematic of a typical wire-convergent plate type EHD gas pump | 24 |
| Figure 3.1: Schematic of Capillary Action appropriate to CPLs | 26 |
| Figure 3.2: Cross Section of an EHD Evaporator showing heat flow and vapour generation | 27 |
| Figure 3.3: Diagram of Inducement of EHD Motion | 31 |
| Figure 3.4: EHD instability on the vapour-liquid interfaces for a) stratified vapour-liquid b) stratified liquid-vapour c) droplets and d) bubble under wire-plate electrodes [17] | 32 |
| Figure 4.1: Diagram of CPL with EHD enhancement | 41 |
| Figure 4.2: Comparison of undamaged wick (left) to damaged wick (right) | 44 |
| Figure 4.3: 180x magnification of a polyethylene wick..... | 44 |
| Figure 4.4: Damaged Wick (a) side view (b) top view..... | 45 |
| Figure 4.5: Neutron Radiograph Setup..... | 49 |
| Figure 4.6: EHD Enhanced Evaporator Components: 1) Evaporator outer shell, 2) spring, 3) Teflon plug, 4) polyethylene wick, 5) end plug, 6) electrode..... | 50 |
| Figure 4.7: Radiograph of evaporator with damaged wick: 1) Evaporator outer shell, 2) spring, 3) Teflon plug, 4) polyethylene wick, 5) end plug, 6) electrode .. | 50 |
| Figure 4.8: Close-up of evaporator end section with gap resolved | 51 |
| Figure 4.9: Schematic of EHD Evaporator for the Capillary Pump Loop | 53 |
| Figure 4.10: Relationship between Electrode diameter (characteristic length) and EHD forces | 54 |
| Figure 4.11: Schematic of Proposed EHD Electrode with Teflon Connectors | 56 |
| Figure 5.1: Schematic of EHD Gas Pump Experimental Apparatus | 69 |
| Figure 5.2: Photograph of EHD gas pump Experimental Apparatus inside Faraday Cage enclosure | 70 |

| | |
|--|----|
| Figure 5.3: Example of Fluctuation Error for Velocity Measurement..... | 71 |
| Figure 5.4: Top) Measurement Grid for Flow Profile Experiments overlaid on EHD gas pump outlet schematic Bottom) Measurement Grid overlaid onto flow profile figure..... | 75 |
| Figure 6.1: EHD Gas Pump Experimental Setup..... | 77 |
| Figure 6.2: Mass Flow and Heat Balance Power vs. Discharge Power for Tsubone's EHD gas pump..... | 81 |
| Figure 6.3: Comparison of Outlet Temperature and Heat Balance Power for Tsubone's EHD gas pump..... | 81 |
| Figure 6.4: Rayleigh Number vs. Temperature for Experimental EHD gas pump | 82 |
| Figure 6.5: Pictures of Corona Formation..... | 85 |
| Figure 6.7: Outlet Temperature Change vs. Applied Voltage for Gen I EHD Gas Pump with Steel String Electrode in Horizontal Orientation | 86 |
| Figure 6.6: VI Characteristics for Gen I EHD Gas Pump with Steel String Electrode | 86 |
| Figure 6.8: Outlet Temperature Change vs. Applied Voltage for Gen I EHD Gas Pump with Steel String Electrode in Horizontal Orientation | 87 |
| Figure 6.9: Peak Spot Velocity vs. Applied Voltage for Gen I EHD Gas Pump with Steel String Electrode..... | 87 |
| Figure 6.10: Comparison of Copper and Steel String Electrode Time Averaged Power vs. Applied Voltage..... | 90 |
| Figure 6.11: Time-averaged-current vs. Applied Voltage for a Copper Electrode at Humidity Range of 50-68% and Ambient Temperature of 23-50°C | 90 |
| Figure 6.12: Peak Spot Velocity vs. Applied Voltage for a Copper Electrode..... | 91 |
| Figure 6.13: Outlet Temperature Change vs. Applied Voltage for a Copper Electrode measured by T-type Thermocouple..... | 91 |
| Figure 6.14: Outlet Temperature Change vs. Applied Voltage for a Copper Electrode measured by Hot-wire Anemometer | 92 |
| Figure 6.15: Comparison of discharge current of an EHD gas pump in horizontal orientation and vertical orientation at 67% humidity and 23°C..... | 95 |
| Figure 6.16: Comparison of discharge power of an EHD gas pump in horizontal orientation and vertical orientation at 67% humidity and 23°C..... | 95 |
| Figure 6.17: Comparison of Peak Spot Velocity of EHD gas pump in Horizontal and Vertical Orientation at 67% humidity and 23°C | 96 |
| Figure 6.18: Comparison of Outlet Temperature Change of an EHD gas pump in Vertical and Horizontal Orientation at 67% humidity and 23°C..... | 96 |
| Figure 6.19: Corona onset and spark discharge with respect to relative humidity | 99 |
| Figure 6.20: Temperature and Flow Velocity vs. Relative Humidity..... | 99 |

| | |
|--|-----|
| Figure 6.21: Comparison of Outlet Temperatures from differing Ambient Temperatures on an EHD Gas Pump in horizontal orientation | 101 |
| Figure 6.22: Comparison of Peak Spot Velocity from differing Ambient Temperatures on an EHD Gas Pump in horizontal orientation | 101 |
| Figure 6.23: Peak Spot Velocity vs. Ehd Number for an EHD Gas Pump | 103 |
| Figure 6.24: Volumetric Flow vs. Ehd Number for an EHD Gas Pump..... | 103 |
| Figure 6.25: Flow Profile for an EHD Gas Pump at 8kV in Horizontal Orientation | 107 |
| Figure 6.26: Flow Profile for an EHD gas pump at 11kV in Horizontal Orientation | 107 |
| Figure 6.27: Flow Profile for an EHD gas pump at 14kV in Horizontal Orientation | 108 |
| Figure 6.28: Temperature Profile for an EHD Gas Pump at 8kV In Horizontal Orientation | 108 |
| Figure 6.29: Temperature Profile for an EHD Gas Pump at 11kV In Horizontal Orientation | 109 |
| Figure 6.30: Temperature Profile for an EHD Gas Pump at 14kV in Horizontal Orientation | 109 |
| Figure 6.31: Flow Profile for an EHD Gas Pump at 8kV In Vertical Orientation | 110 |
| Figure 6.32: Flow Profile for an EHD Gas Pump at 11kV In Vertical Orientation | 110 |
| Figure 6.33: Flow Profile for an EHD Gas Pump at 14kV in Vertical Orientation | 111 |
| Figure 6.34: Temperature Profile for an EHD Gas Pump at 8kV in Vertical Orientation | 111 |
| Figure 6.35: Temperature Profile for an EHD Gas Pump at 11kV in Vertical Orientation | 112 |
| Figure 6.36: Temperature Profile for an EHD Gas Pump at 14kV in Vertical Orientation | 112 |
| Figure 6.37: Forced Convection Air Flow Velocity Profile..... | 114 |
| Figure C.1: Experimental Capillary Pumped Loop..... | 132 |
| Figure C.2: Evaporator Components, Left) Electrode, End Cap, Wick, Teflon Plug, Spring and Metal Casing, Right) Assembled Evaporator with Heater Bands attached..... | 132 |
| Figure D.1: Diagram of Beam Port 3 | 136 |
| Figure D.2: Radiograph of evaporator after image analysis | 137 |
| Figure D.3: Edge detection image of evaporator using a Sobel filter..... | 137 |
| Figure E.1: Data Acquisition System for the CPL | 141 |
| Figure E.2: Temperature vs. Time measured by the DAQ System..... | 144 |
| Figure E.3: Pressure vs. Time using the DAQ system..... | 144 |

Figure F.1: Freon R134a Property Table 148

List of Tables

| | |
|--|-----|
| Table 2.1: Fast Spectra Nuclear Reactor Designs for Space Applications | 12 |
| Table 4.1: Dimensionless Numbers of Electrode Region of Evaporator | 55 |
| Table 5.1: EHD Gas Pump Experiment Components | 68 |
| Table 5.2: EHD gas pump Instrumentation | 68 |
| Table 5.3: Camera Equipment | 72 |
| Table 5.4: Test Matrix | 73 |
| Table 6.1: EHD Gas Pump Experimental Data Sets | 78 |
| Table 6.2: Legend Symbols | 78 |
| Table B.1: Fundamental Equations for EHD and MHD Induced Motion | 130 |
| Table E.1: Data Acquisition System Components | 142 |
| Table F.1: Expected Freon R134a Properties for Experimental CPL | 147 |

List of Appendices

| | |
|--|-----|
| Appendix A: Future Space Missions | 126 |
| A.1 NASA's Shuttle and Rocket Launch Schedule | 127 |
| Appendix B: Electrohydrodynamic Equations and Theory | 130 |
| Appendix C: Capillary Pumped Loop with EHD Enhanced Evaporator | 131 |
| Appendix D: Neutron Radiography Analysis..... | 133 |
| D.1 Frame Average Program | 138 |
| Appendix E: Data Acquisition System | 140 |
| E.1 LabView DAQ Program | 145 |
| Appendix F: Freon 134a Properties..... | 147 |
| Appendix G: Publications and Presentations..... | 149 |

Nomenclature

| | | | |
|----------|--|--------------|---|
| A | Cross Sectiona Area (m^2) | Re | Reynold's Number |
| B | Magnetic Flux | RH | Relative Humidity (%) |
| C_p | Heat Capacity | T | Temperature (K) |
| D | Diffusion constant | T_g | Temperature of a gas (K) |
| D_h | Hydraulic Diameter (m) | T_s | Reference Temperature (K) |
| E | Electric Field (V/m) | T_w | Corona Wire Temperature (K) |
| e | Elementary Charge (1.6×10^{-19} C) | U | Flow Velocity (m/s) |
| Ehd | Electrohydrodynamic Number | V | Voltage (V) |
| E_{se} | Electrostriction Number | Greek | |
| F_{EB} | Electric Field Force (N) | α | Thermal Diffusivity (m^2/s) |
| g | Acceleration due to gravity (m/s^2) | β | Coefficient of Thermal Expansion (K^{-1}) |
| H | Magnetic Field Strength | ϵ_g | Dielectric Constant Gas |
| I_s | Discharge Current (A) | ϵ_l | Dielectric Constant Liquid |
| L | Characteristic Length (m) | ϵ_o | Permittivity of Free Space (8.854pF/m) |
| Md | Masuda Number | κ | Thermal conductivity |
| N | Number Density | μ_g | Dynamic Viscosity (kg/m·s) |
| N_i | Ion Number Density | μ_i | Ion mobility ($m^2/V\cdot s$) |
| P | Pressure (Pa) | ν | Kinematic Viscosity (m^2/s) |
| Q_{EB} | Energy from Electric Field (J) | ρ | Density (kg/m^3) |
| R | Resistance (Ω) | | |
| Ra | Rayleigh Number | | |

1. Introduction

Over the recent decades, advances in satellite and spacecraft technology have transformed space-based applications into a burgeoning international industry that no longer belongs to the world's richest governments with civilian companies racing to be the first to establish commercial space flights [1]. Excitingly, over 40 years after man first landed on the moon outer space is no longer just the domain of the American and Russian space programs. With the completion of the international space station, Japan and the European Space Agency (ESA) have established themselves as significant participants in the space age. Now, China has also started to invest significantly in space flight and space technology. These advances include space-based nuclear applications. Nuclear reactor powered spacecraft and propulsions systems have already been developed by NASA and the Russian Space Agency [2-4]. However, nuclear reactors in space-based applications face different design challenges than terrestrial reactors in several areas, including heat transport. Space-based reactors require their heat transport systems to be efficient in zero gravity and microgravity environments [5,6], to have minimal power requirements, to be able to operate within a confined area, to have a long life span and to have a higher reliability due to difficulty of repairs [7,8]. Increasing the heat transport efficiency of space-based nuclear reactors would allow for more space-based nuclear applications to be developed and improved [9-14].

In order to achieve improved efficiency in extraterrestrial environments, traditional terrestrial nuclear technology such as mechanical pumps need to be replaced with more suitable technology. Such as heat pipes or capillary pumped loops (CPL), devices that use capillary action or pressure gradients to transport heat and mass flow without the aid of gravity or a complicated system of moving parts. Improvement of the heat transport efficiency of these types of devices, especially CPLs, and their application to nuclear power or nuclear propelled space reactors could be the necessary technological and design improvement

with regards to heat and mass transport that allows nuclear technology to be used and adapted by the burgeoning commercial and international space industry.

CPLs still are limited in their ability to transport heat. However, a CPL's heat transport abilities can be enhanced by the application of Electrohydrodynamics (EHD). Electrohydrodynamics concerns the physical phenomena of using electric fields to generate fluids flow, both in terms of mass transport and heat transport [15] In particular, EHD forces, introduced from a high-voltage low current electrical signal or pulse, can be used to induce or enhance fluid flow. EHD has been studied since the early 20th century, but it's not until recently that EHD research has been used in applications such as CPLs and EHD gas pumps. EHD devices have the characteristics that suggest they may be ideal for use in space applications. EHD devices typically have the following characteristics important to space reactor design [16]:

- Lightweight
- No moving parts
- Low power supply
- Function effectively in a zero-gravity environment
- Minimal physical space requirements

The inclusions of EHD devices into heat transport loops of space-type reactors could enhance heat transport to the levels required by a nuclear space-type reactor. The project will study the behaviour of EHD gas pumps to determine their ability to improve the efficiency of heat transport in nuclear space applications; including the addition of EHD gas pumps and EHD enhanced evaporators in capillary pumped loops. EHD enhanced CPLs are a capillary pumped loop system consisting of a hot leg and cold leg where the fluid is heated in an evaporator and pumped through a wick using capillary forces. A typical schematic of a capillary pumped loop is shown in Figure 1.1. The evaporator contains an electrode, where an electric field is applied to enhance the mass flow

rate in the evaporator-wick region. This enhancement has demonstrated increased performance as further explained in Chapter 2.3.

1.1 EHD Devices

The EHD devices of interest to this project are an EHD gas pump and an EHD evaporator. Each design aspect of EHD devices is to be studied as a means to improve heat transport in a CPL. The experimental CPL being used in this project consists of an evaporator section; a condenser, and connected piping. The transport fluid is Freon 134a. Heaters are applied to the evaporator section. The outer channel of the evaporator boils the Freon. Between the outer channel and the inner channel is a porous polyethylene wick with a pore size 20 μ m. As the fluid in the outer channel evaporates, Freon passes through the wick via capillary action.

The evaporated Freon flows to the condenser where it is condensed back to a liquid state. Research has shown [9, 17-18] that natural circulation occurs in this configuration, but is limited by the performance of the capillary action. Dryout of the wick can occur and cause impairment of fluid transport. Additional research [16] has demonstrated that the application of an EHD electrode in the evaporator can enhance fluid transport across the wick.

An electrode is included in the wicked evaporator to enhance fluid transport. To further enhance the fluid transport, an EHD gas pump is considered in the vapour leg of the loop. The presence of a gas pump is believed to help the vapour reach the condenser and enhance the flow from the evaporator by stabilizing the fluid transport. The pump then allows the vapour leg to act as a push-pull system between the evaporator and the condenser. EHD gas pumps currently are not included in the design of CPLs. EHD gas pumps also have an electrode that will generate EHD forces when high-voltage is applied. The forces will initiate a flow in a direction dependent upon the design of the EHD gas pump. There are several EHD gas pump designs to consider. Wire-plate type uses a wire as the corona electrode and a ground plate. The plate can then be either parallel or non-parallel in design [19-22]. Wire-rod type consists of a wire corona electrode

and a rod as the ground electrode [23-25]. Narrow-channel gas pumps have a narrow channel that acts as an inlet to direct the flow [26-29]. These EHD gas pumps designs all have similar characteristics that suggest they would be suitable for inclusion into a CPL [30-32].

Gas pumps could be used to increase flow rates inside CPLs to reduce pressure in certain areas, help control flow rates and improve condenser performance [9, 16-17].

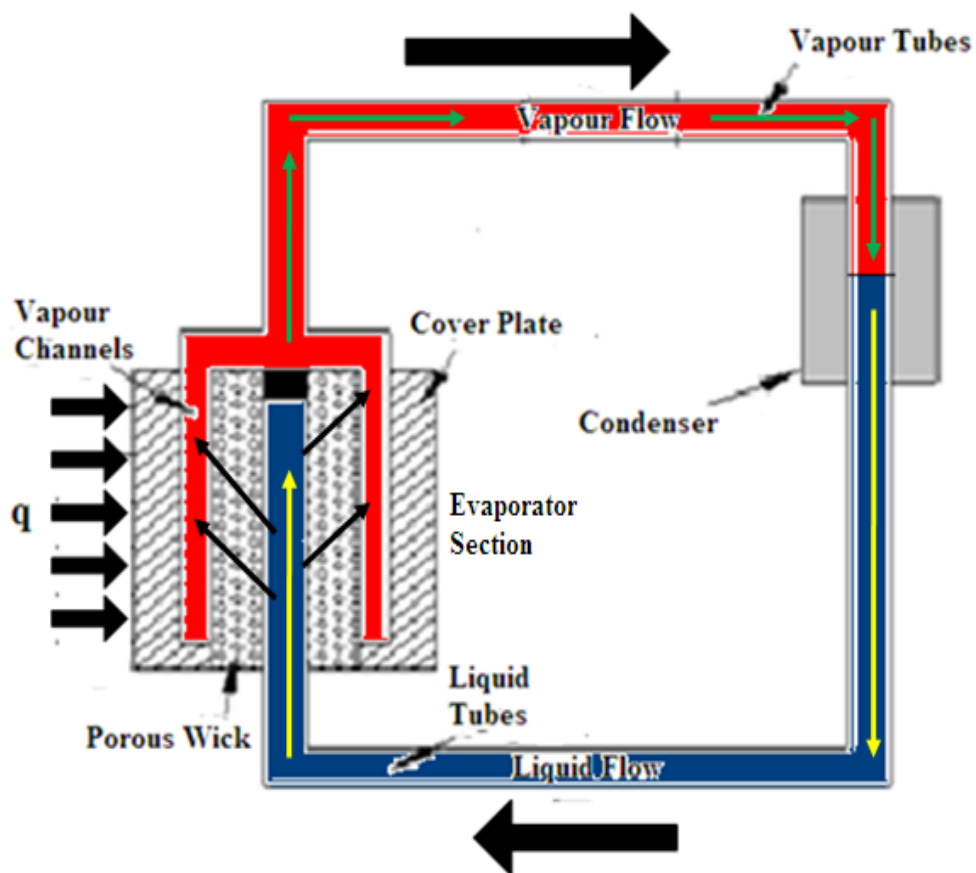


Figure 1.1: Heat Flow diagram for a CPL

1.2 EHD Forces

The desired EHD phenomena (as shown in Figure 1.2) for this study occurs when a high-voltage, low current electric field is applied to an electrode immersed in a fluid. The electric field then ionizes the fluid causing the fluid to become a stable plasma about the electrode, known as the corona. The ions then move either towards or away to the nearest ground or bounds of the electric field depending on their polarity and the direction of the electric field,. Therefore EHD phenomena are directly dependent on the electric field strength and distance from the centre of the electric field. The electric field that generates this type of EHD flow is a special case. The potential difference of the electric field needs to be high enough, usually at least 5kV [17], to create a corona. However, the current needs to be regulated at a low enough level, on the order of microamperes to milliamperes [33], to maintain corona. Too high a current and the corona regime will become unstable and enter the spark region, where the desired EHD phenomena can no longer occur. Therefore the applied electric field is bounded to a specific range of about 5kV -15kV with currents between 50-600 μ A. It should be noted that while both the EHD evaporator and EHD gas pump use applied high voltage electric fields to generate EHD forces the phenomena and dominant forces present in each device are different. A more detailed description of the physics of EHD phenomena and electric fields is present in Chapter 3.3.

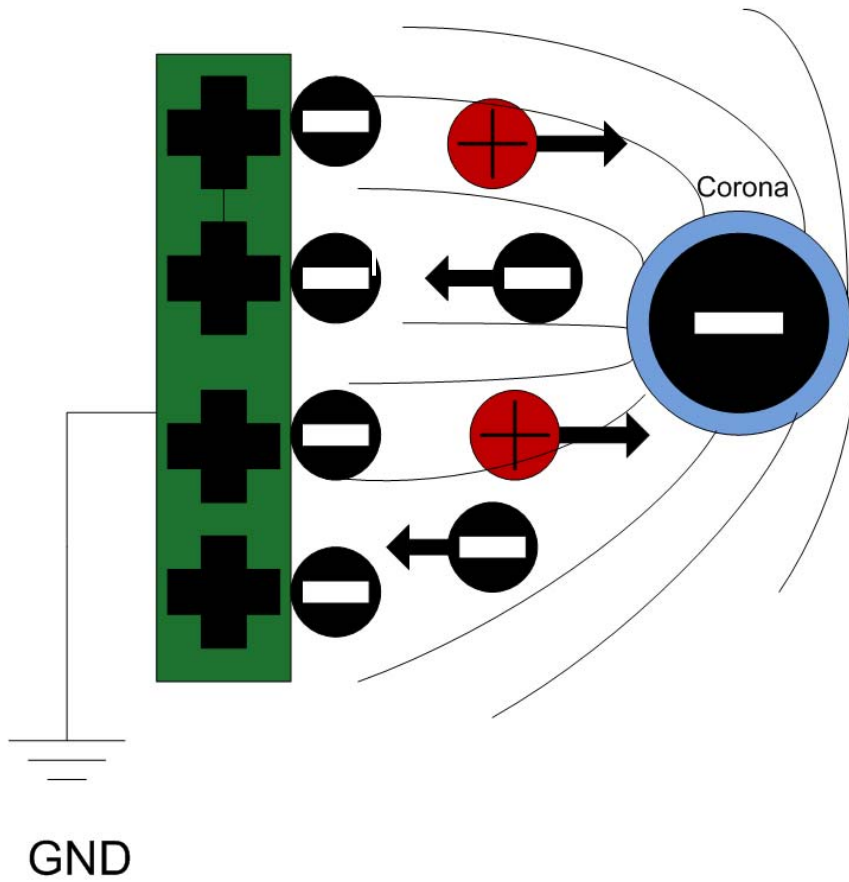


Figure 1.2: Diagram of EHD forces and their effect on ions in the presence of an electric field

1.3 Objective

The addition of EHD forces to a CPL clearly has potential benefits toward heat transfer and performance, especially for space applications. Therefore it is imperative that work be performed to enhance the design of the CPL for space applications. The initial stage of this work should concentrate on experimental work using CPL test sections and EHD devices such as gas pumps in a laboratory setting. The work should be structured with the goal to improve performance in the experimental CPL with the end result leading to a better understanding of how EHD enhancement can improve heat transport and CPL design.

Using the above mentioned goal as a guideline, the research is designed to achieve the following objectives;

- (i) To design an improved EHD enhanced CPL to improve heat transfer.
- (ii) To design an improved evaporator.
- (iii) To assess the performance of EHD gas pumps for applications in the vapour leg of a CPL.

More detail regarding the type of space based reactor design, the theory of CPLs and the theory of EHD gas pumps is given in Chapter 2. A review of theory and previous experimental work is also discussed in Chapter 2. Chapter 3 assesses the theory and design of CPL and EHD gas pumps as well as a detailed description of the physical theory of EHD phenomena. Chapter 4 describes in detail the design work for enhancing the CPL. Chapter 5 describes the experimental apparatus for the EHD gas pump experiment. The experimental results for the EHD gas pumps are presented in Chapter 6. Conclusions and recommendations can be found in Chapter 7 and 8 respectively.

2. Literature Review

This chapter reviews the current state of nuclear space reactor design and establish the need to further improve heat transport methods for nuclear space reactor applications. From here, the theory, current status and design of capillary pumped loops, electrohydrodynamically enhanced evaporators and electrohydrodynamics gas pumps are reviewed to provide a basis of their fundamental operation design and performance.

2.1 Nuclear Reactors for Outer Space and Extraterrestrial Applications

Space vehicles and platforms require large amounts of energy (at least 110kWe [11, 34] and up to 2.8 MWe [35]) for power generation and propulsion depending on the purpose of the spacecraft. Nuclear energy and therefore nuclear reactors or nuclear batteries are being considered for use in future missions and applications; both near Earth orbit (satellite and moon-based) and deep space. Nuclear power is especially being considered for deep space missions as the decreasing solar intensity due to the increasing distance between the spaceship and the sun renders solar power impracticable [26] and thus a greater need for alternative energy sources. Nuclear reactors for space have been studied for over four decades beginning in Russia (then U.S.S.R) in the 1960s where the Russians eventually developed a reactor to power satellites. Between 1970 and 1988 Russia launched several nuclear powered satellites into orbit. Since then several satellites using nuclear reactors have been launched and nuclear reactors have also been used in recent exploratory unmanned missions to Saturn and Pluto [7]. As applications in space increase and exploration ventures further out into the solar system the demand for space reactors will also increase.

Space reactors differ in design and design requirements from traditional reactors on Earth used in power plants, or even those on submarines, due to

the environmental differences between Earth and space. Everything from coolant the being used and the shielding present to the reactor's thermalhydraulics and neutronics must be considered for various space environments. Once in space, the reactors will be difficult to repair so reliability and operational life requirements increase in importance to ensure a mission's successful completion. If power cannot be provided to the ship or outpost it could leave people stranded without the power in the middle of space. So, ensuring operation life and removing any single point failures is a key aspect of space reactor design [34]. Figure 2.1 presents a diagram of the basic systems of a nuclear powered manned spacecraft.

Currently, new designs of space reactors for both power generation and propulsion are being studied and developed around the world including NASA and other space agencies [34, 36]. These studies are focusing on advanced reactor designs such as pebble bed and fast energy spectra reactors [2, 7-8, 11-12, 34-37]. The majority of the designs use various types of lightweight fast reactors to power or propel various applications and are either gas cooled or liquid metal cooled. Figure 2.2 presents a proposed gas-cooled pebble bed nuclear space-based reactor with a 5 year operation lifetime [34]. This reactor is designed for propulsion and not for powering secondary systems or providing electricity. Essentially, hydrogen gas is heated to high temperatures via the nuclear heat generated in the core. The high temperature hydrogen now has enhanced momentum which is transferred to the spacecraft while the hydrogen is ejected from the torus nozzle.

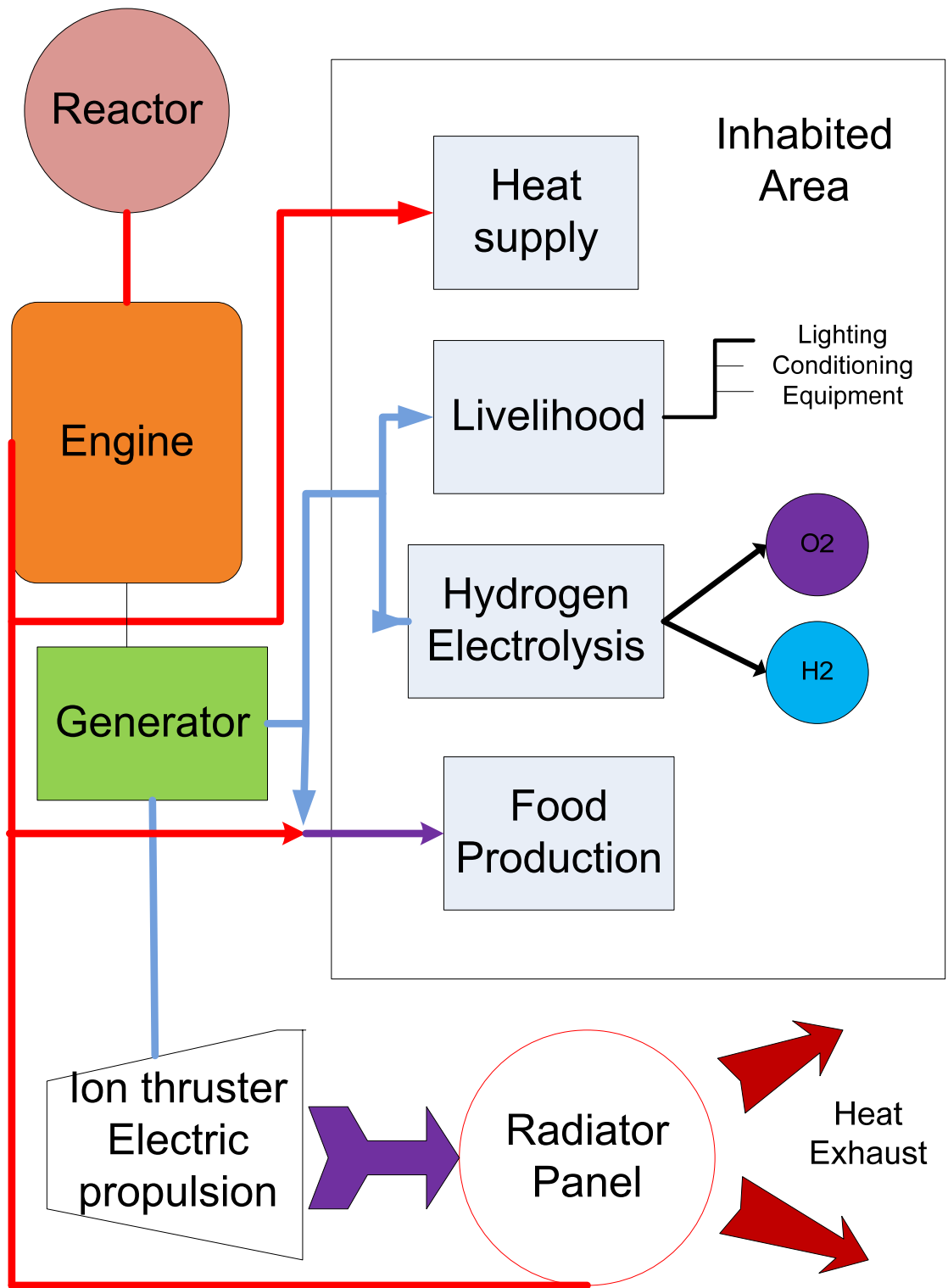


Figure 2.1: Concept design of a nuclear power plant for support of a space based facility [12]

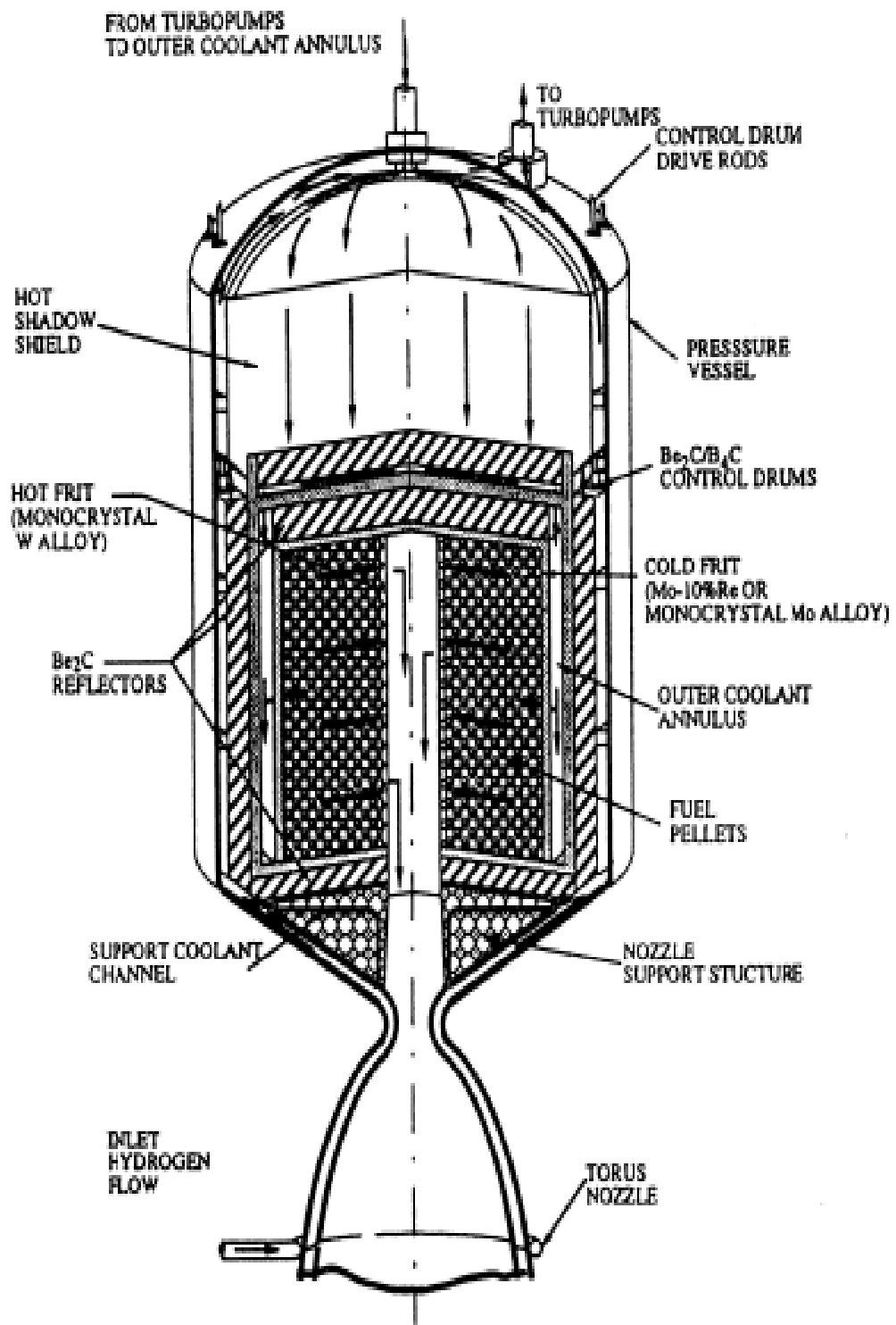


Figure 2.2: Concept for a Pebble bed type space reactor for propulsion [34]

However, Fast Spectra reactors are considered a more viable option due to smaller space requirements and longer lifetime, and because they have been design to eliminate single point failures [7]. Several fast reactor designs have been proposed. Table 2.1 gives an overview of the fast reactor designs for space applications [11, 12, 34]. Figures 2.3-2.7 show schematics for each type of reactor design.

Table 2.1: Fast Spectra Nuclear Reactor Designs for Space Applications [11-12, 34]

| Reactor Design | Lifetime(years) | Power | Cooling Method |
|--|-----------------|---|---|
| SAIRS—Scalable AMTEC Integrated Reactor Space Power system (Figure 2.3) | 10-15 | 30-35We/kg 18, 5.6 -24, 4.2 kWe Amtec Units | Lithium Heat Pipes |
| Heat pipe cooled reactor with segmented thermoelectric Module converters (HP–STMCs) (Figure 2.4) | 10-15 | 110kWe | Lithium heat pipes (Figure 2.8) |
| Sectored, compact reactor (SCoRe) space power system (Figure 2.5) | 4 | 2.5MW thermal | Convectively cooled with circulating liquid NaK |
| Submersion-subcritical, safe space (S ⁴) reactor power System (Figure 2.6) | 10-15 | 471kWth 93kWe | He-Xe Binary mixture |
| Sterling Engine (Figure 2.7) | N/A | 12 MWth 2.8MWe | Lithium cooled heat pipes |

As steam generation and boiling in space are difficult the designs must utilize radiators to reject the heat. The radiators replace the steam generators by acting as the medium to transport the heat from the reactor to the electrical generator. The radiators can use outer space as the heat sink, which can be considered a black body, greatly improving the efficiency of the radiators. The inclusion of the radiator removes the need for water to act as a medium of heat transport. This allows for the designs to consider different modes of heat transport such as liquid metal heat pipes and reactor types such as sodium cooled reactors to be considered because the safety issues of water reacting with some types of liquid metal, especially sodium are no longer a concern [11]. In the case of propulsion, electrical generation may not be necessary but radiators will still be necessary to remove the heat from the reactor and propulsion systems. Figures 2.3 - 2.7 present current suggested designs for nuclear powered or propelled spacecrafts from American and Japanese space agencies and research institutions. The designs vary in detail and in their progress, however they all require some method of heat transport beyond that of traditional terrestrial methods, such as mechanical pumps. In most of the designs liquid cooled heat pipes are considered. Figure 2.8 displays a diagram of a proposed heat pipe design concept.

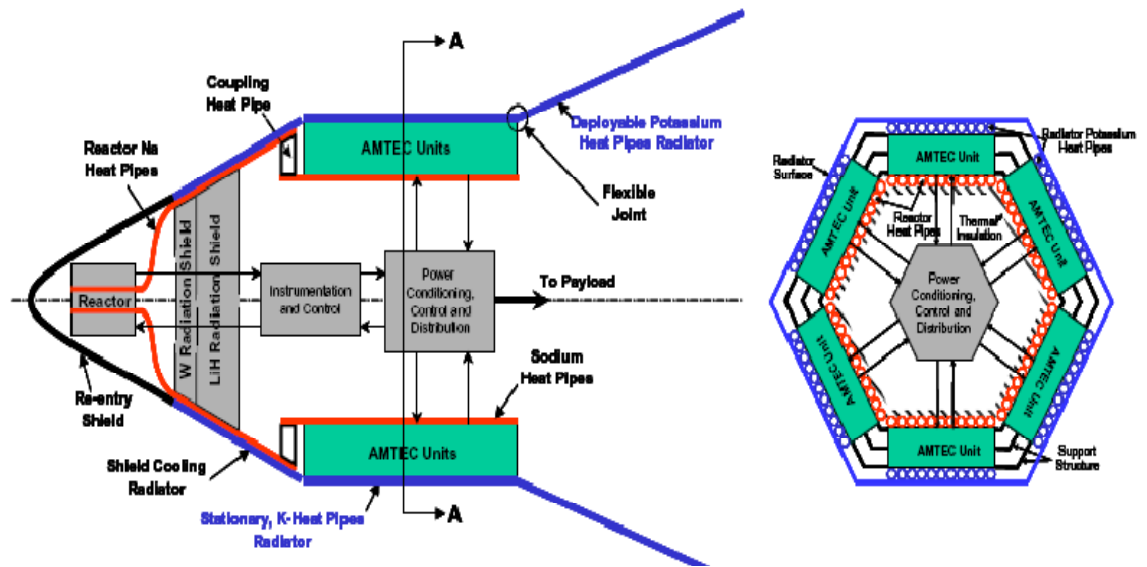


Figure 2.3: Schematic of the SAIRS concept reactor [34]

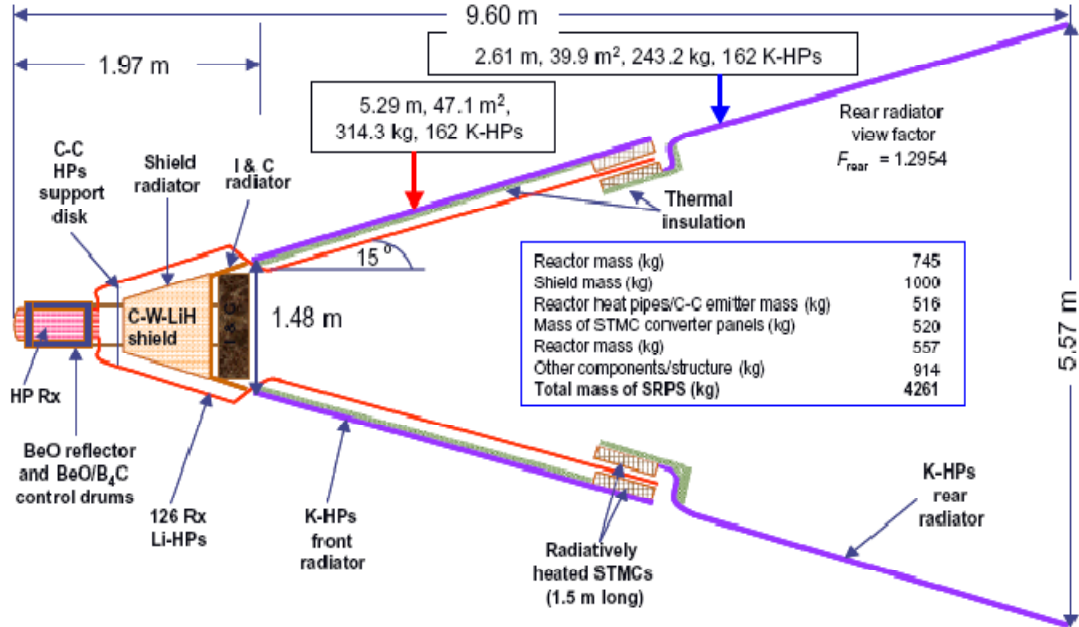


Figure 2.4: Schematic of the HP-STMCs concept reactor [34]

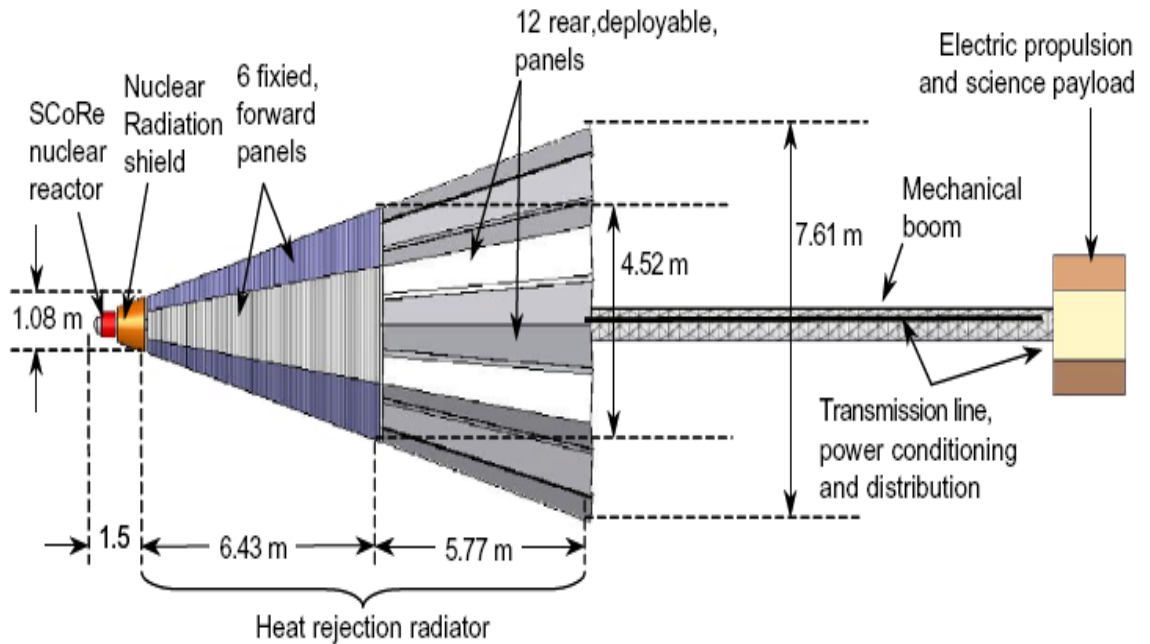


Figure 2.5: Schematic of the SCoRe S11 concept reactor [34]

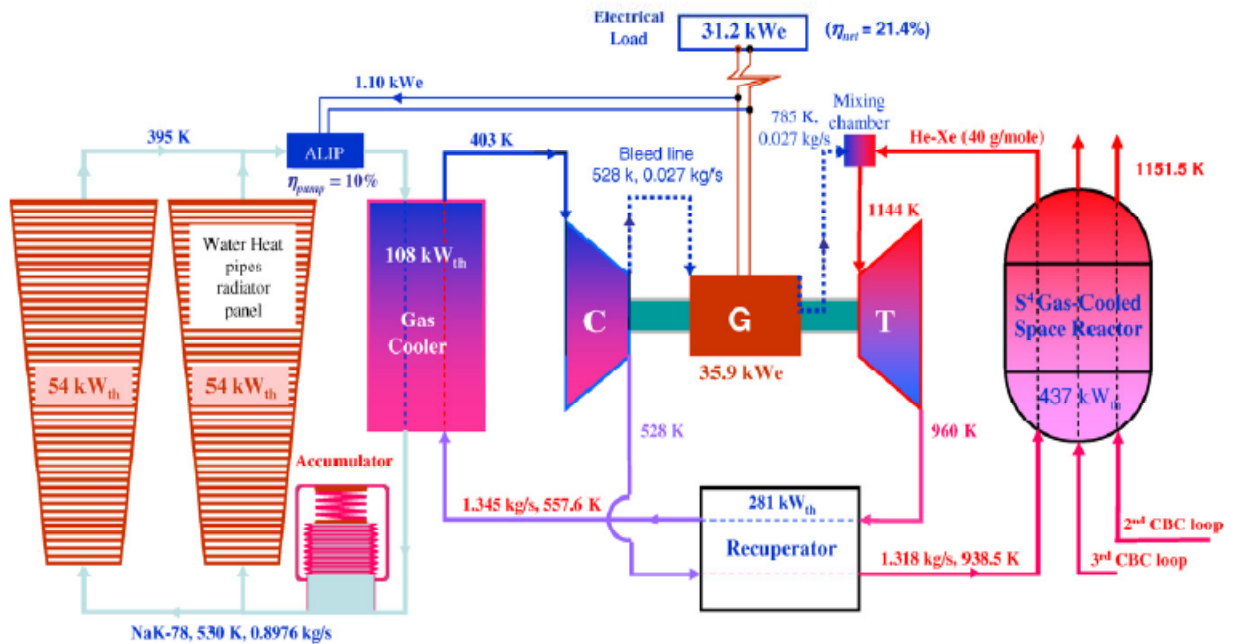


Figure 2.6: Schematic of the S⁴ CBC concept reactor [34]

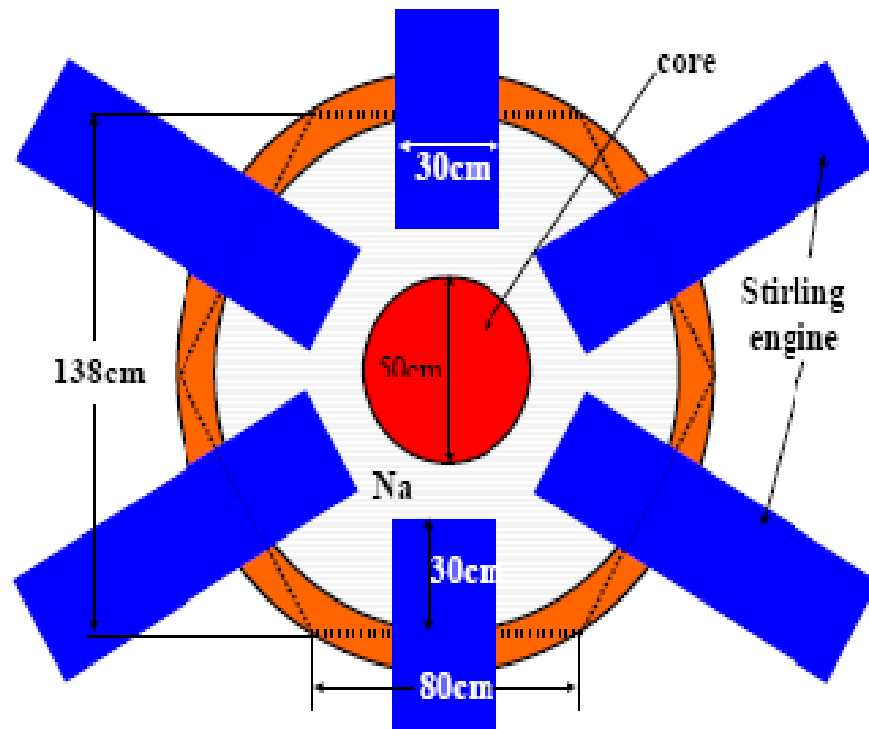


Figure 2.7: Schematic of the Sterling Engine Reactor concept [12]

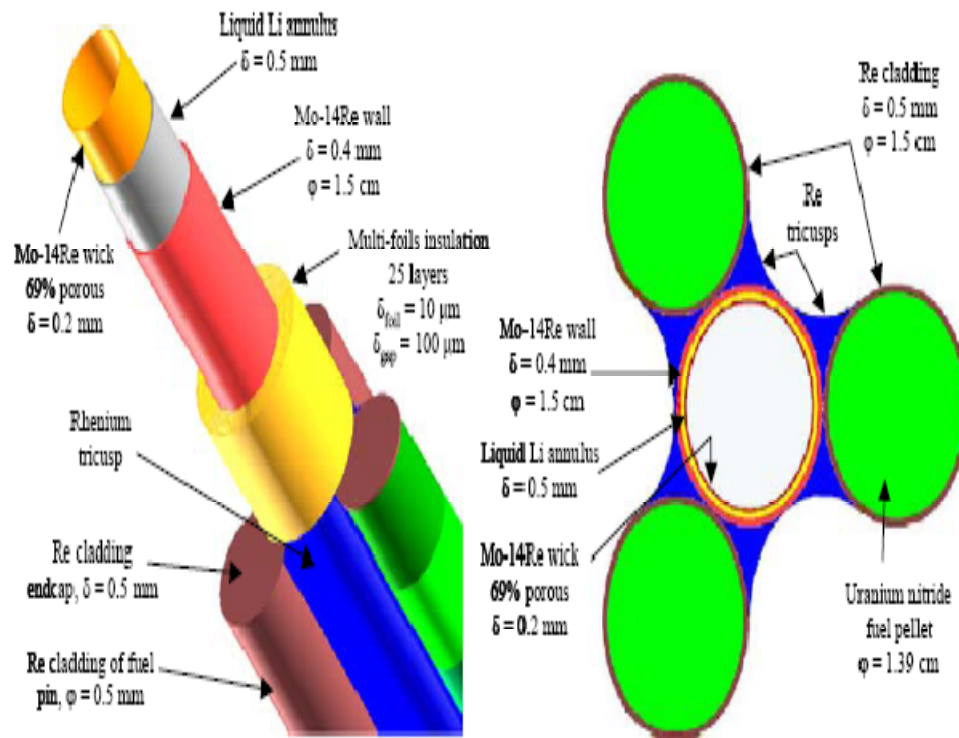


Figure 2.8: Lithium heat pipe for a HP-STMCs [11]

After reviewing the designs and heat transport methods it is apparent traditional systems such as reactivity control, energy conversion and heat transport are still required, and also are being studied and redeveloped so that they are suitable for a space environment. Studies involving heat transfer [32, 38, 39] have shown that these reactors will require new methods of transporting heat that are more suitable to space environments. The difficulty in repairing and maintaining components in space, limited resources and the micro gravity environment require heat transport systems to have minimal moving components, minimal power consumption and be able to operate efficiently in a zero or micro gravity environment. Current studies [10, 39-41] have suggested heat pipes could be used for heat transport in space reactors as they possess the qualities to be effective in outer space. Many of the designs mentioned above consider using lithium heat pipes as the primary cooling method. Heat pipes work on principles similar to capillary pumped loops, including using wicking pressure and capillary action to transport mass and heat. It is important to note though that heat pipes can also vapour lock or dryout and have limitations with regards to heat transfer. These difficulties could be overcome by the use of capillary pumped loops [11, 42]. Additionally, some applications such as cooling of electronics or the reactor could be performed by EHD enhanced devices such as gas pumps, capillary pumped loops or liquid-vapour heat pipes as oppose to liquid metal heat pipes.

2.2 Capillary Pumped Loops

CPLs are one method being studied to improve heat transport efficiency of space based applications. CPLs have been studied for space based applications since the 1960s starting with Stenger [3] and have been heavily studied by NASA and the ESA [9]. Similar work has also been performed on looped heat pipes (LHP) by the Russian Space Agency, however LHPs design differ slightly to CPLs in that LHPs apparatuses uses a multiple wick design. These studies have demonstrated CPLs ability to function in microgravity environments with little or no difference in performance to terrestrial environments [9]. Therefore, due the expense and complexity of experimentation in microgravity and extraterrestrial environments, many of the heat transfer experiments on CPLs were performed in

a terrestrial laboratory setting. Bazzo et al. and others [9, 13, 14] have demonstrated that capillary pumped loops have the capability to be efficient and effective in mass and heat transport. Shelentynsky et al. and Komeili et al., in their work determined that much of the limitations of CPL, including dryout and flow rate may be partially resolved by the introduction of EHD phenomena to CPLs [9, 17].

CPLs in general consist of a liquid leg and a vapour leg. The working fluid enters an evaporator, where it is heated and then the vapour is diffused through a capillary wick into vapour channels as seen in Figure 1.1. The vapour travels to a condenser where the fluid is condensed back to the liquid state and then recirculated through the loop to the evaporator. CPLs work on the principles of capillary action and pumping forces, diffusion and free convection that will allow it to function properly in space environments as well CPLs have low power requirements and no moving components.

CPLs have been shown to be an effective method to thermally manage a system [3, 9, 13-14, 17, 43-44]. A typical capillary pump loop consists of a fluid that is diffused through a wick and heat as it passes through as main mechanism of heat and mass transport. The vapour then diffuses through the wick carrying the heat from the system to vapour channels where it can be removed. The remaining fluid enters a condenser and is recirculated back into the system using free convection.

2.3 Capillary Pumped Loops with an EHD Enhanced Evaporator

Previously, the evaporator section of the CPL was electrohydrodynamically (EHD) enhanced by Komeili et al. in order to improve the efficiency of the diffusion of the vapour through the wick and into the vapour channels and to reduce dry out conditions that occur during operation. Even though, EHD enhanced CPLs have been shown to be effective in increasing efficiency and reducing dry out conditions, further improvement is still possible [17]. The evaporator section of the CPL is enhanced by using EHD forces to help diffuse the fluid by moving it towards the wick as shown in Figure 2.9. Another benefit to enhancing the loop with an EHD evaporator is that the loop can now be designed to move heat without the need of natural circulation. This allows for EHD enhanced CPLs to be used in zero and microgravity environments. A diagram of an evaporator section and a more detailed discussion of EHD CPLs can be found in Chapter 4.1 to 4.3. In general, the evaporator section consists of a central electrode (corona electrode) placed inside the evaporator. The outer tube, a metal, acts as the ground electrode. High voltage is applied directly to the corona electrode and a heat source can be applied to the outer wall if necessary. In between the electrode and the wall is a porous wick. The fluid enters the chamber and is enclosed by the wick. As the fluid evaporates and diffuses through the wick, it usually enters a vapour channel and is removed. However, some evaporator designs do not have vapour channels.

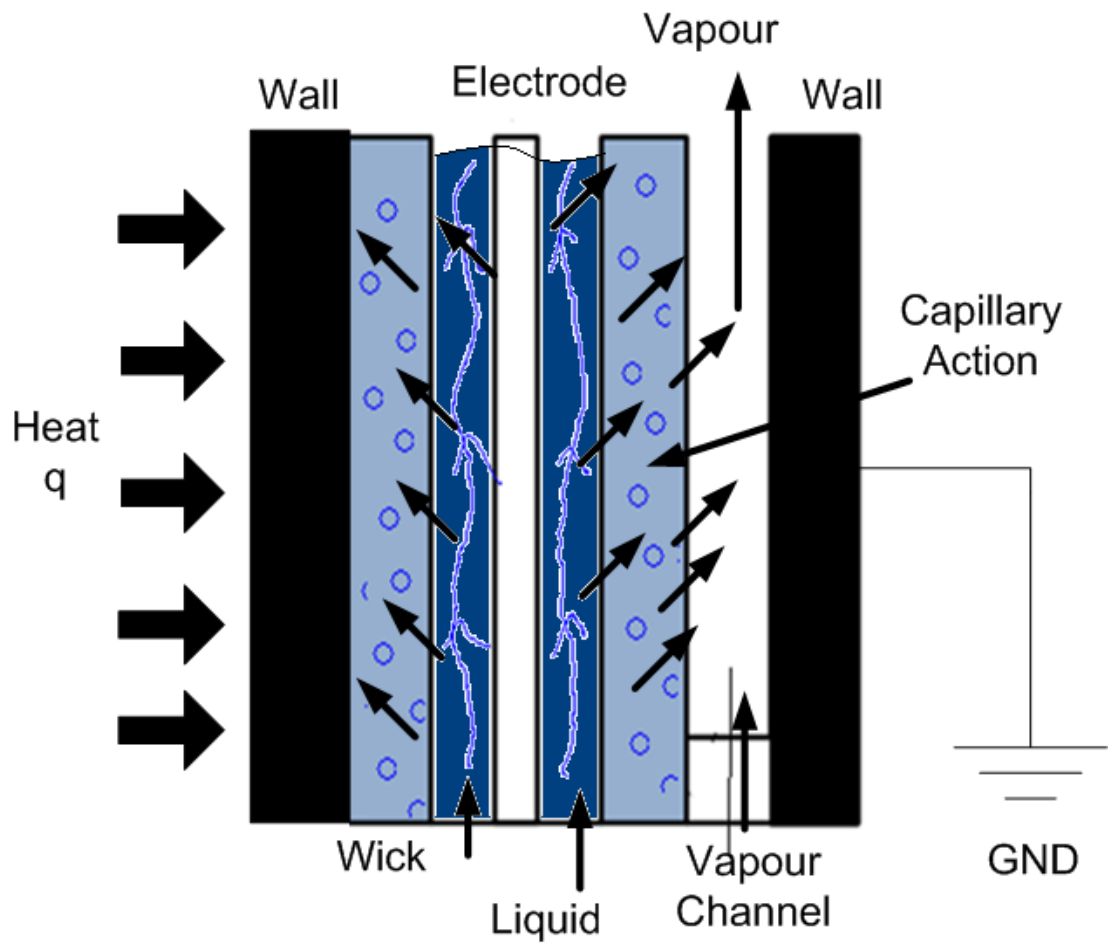


Figure 2.9: Diagram of inside of the evaporator

The location or existence of vapour channels in the design is important from a thermohydraulics standpoint. The fluid entering the evaporator is liquid single phase flow and is heated in the evaporator so that boiling occurs and the fluid reaches a vapour state. The vapour is transferred to a heat sink, making the vapour phase the primary fluid phase used to remove the heat. The flow inside the evaporator is now a two-phase flow. The surface tension of the fluid and capillary action of the wick cause the vapour bubbles to be pulled through the wick and into the vapour channel. The vapour channels lead to a heat sink (condenser) which removes the heat. This creates a pressure differential between the channel and wick, which allows for a continuous flow vapour from the wick to the vapour channel and then to the heat sink. A positive pressure gradient occurs at the interface of the wick and vapour channel as the bubbles are now present in the vapour channel as oppose to the wick [17]. It is the positive gradient acting across the interface that provides the driving force. It is the addition of this driving force in EHD enhanced evaporators that will generate the expected improved flow rates in CPLs.

2.4 Electrohydrodynamic gas pumps

The gas pump is ideal for space applications for several of the reasons mentioned in the previous chapter. EHD gas pumps have no moving parts, are inexpensive, can be used in pipes and can be used on a micrometre scale. However, several basic characteristics of these pumps have only recently been investigated including how polarity, electrode position, and electrode design affect velocity, pressure drop and flow rate. In these studies the working fluid in the gas pump was typically air as oppose to Freon R134a in the experimental CPL [9, 16].

The pumps consist of a corona electrode placed perpendicular to the flow inside a flow chamber. Also in the chamber is a ground or a set of ground electrodes. The corona electrode is either a wire type or a sharp needle type electrode. However, research has demonstrated that the wire type is the preferred design as wire type electrodes have a wider voltage range between corona onset and

spark discharge [9]. The ground electrode can be a cylindrical rod or a set of plates. The plates are either parallel or off set on convergent angles. Previous research suggests non-parallel plates are more effective as an optimum angle can be found to improve different characteristics including velocity and flow rate [16]. Also, the flow rate is lower in parallel plate gas pumps as the symmetry of the pump creates an electric field that generates motion against the flow, therefore not allowing significant unidirectional flow to be generated due to the equal distance between the corona electrode and the ground plates. Even though gas pump designs can vary, the principle used is the same. A high voltage is applied to the electrode so that a corona discharge is created. If the voltage is too high, spark discharge will take place due to the breakdown of the gas and the EHD motion will stop. If the voltage is too low a corona will not form and gas ions will not be created. The corona discharge then creates an EHD effect causing fluid motion in the direction of flow. In most cases, the working fluid in EHD gas pumps is air at room temperature and pressure [9, 15-16, 18-19]. However, in some EHD designs and applications a different dielectric fluid is used as the working fluid. Generally, the fluid is single phase for EHD gas pump applications; however the pump can operate using two-phase flow. The conditions within the pump usually are not conducive to generating a phase change, so the flow would already have to be two-phase when entering the chamber.

The flow generated is usually laminar although turbulent eddies and re-circulation effects have been observed. Wake effects have also been observed from the flow crossing the electrode [9]. However, the flow cannot progress very far past the laminar region as the forces generated by the turbulence are greater than the EHD forces and negate the EHD forces as they become the dominant in the system.

In general, research to date has discovered that polarity, ground electrode distance, rod diameter, discharge current and ground plate angle all affect the performance of the EHD pump. The pump has higher velocities and flow rates

when a negative voltage is applied as opposed to a positive one. Also discharge current, velocity, flow rate and power increases with voltage until a maximum voltage is reached, usually right before the onset of spark discharge. In wire-rod types, velocity increases with rod diameter from increasing discharge current or Ehd number of the wire. Furthermore, smaller rod diameter will allow for a velocity to be achieved with less power [9]. In wire-plate type, the ground electrode location and plate angles can be varied to achieve optimal performance as both location and angle affects pressure drop, velocity and flow rate [16].

EHD gas pumps consist of a corona electrode placed perpendicular to flow inside a flow chamber. Also in the chamber is a ground or a set of ground electrodes. A schematic of a typical wire-plate type gas pump is shown in Figure 2.10. The corona discharge then creates an EHD effect causing fluid motion in the direction of the electric field.

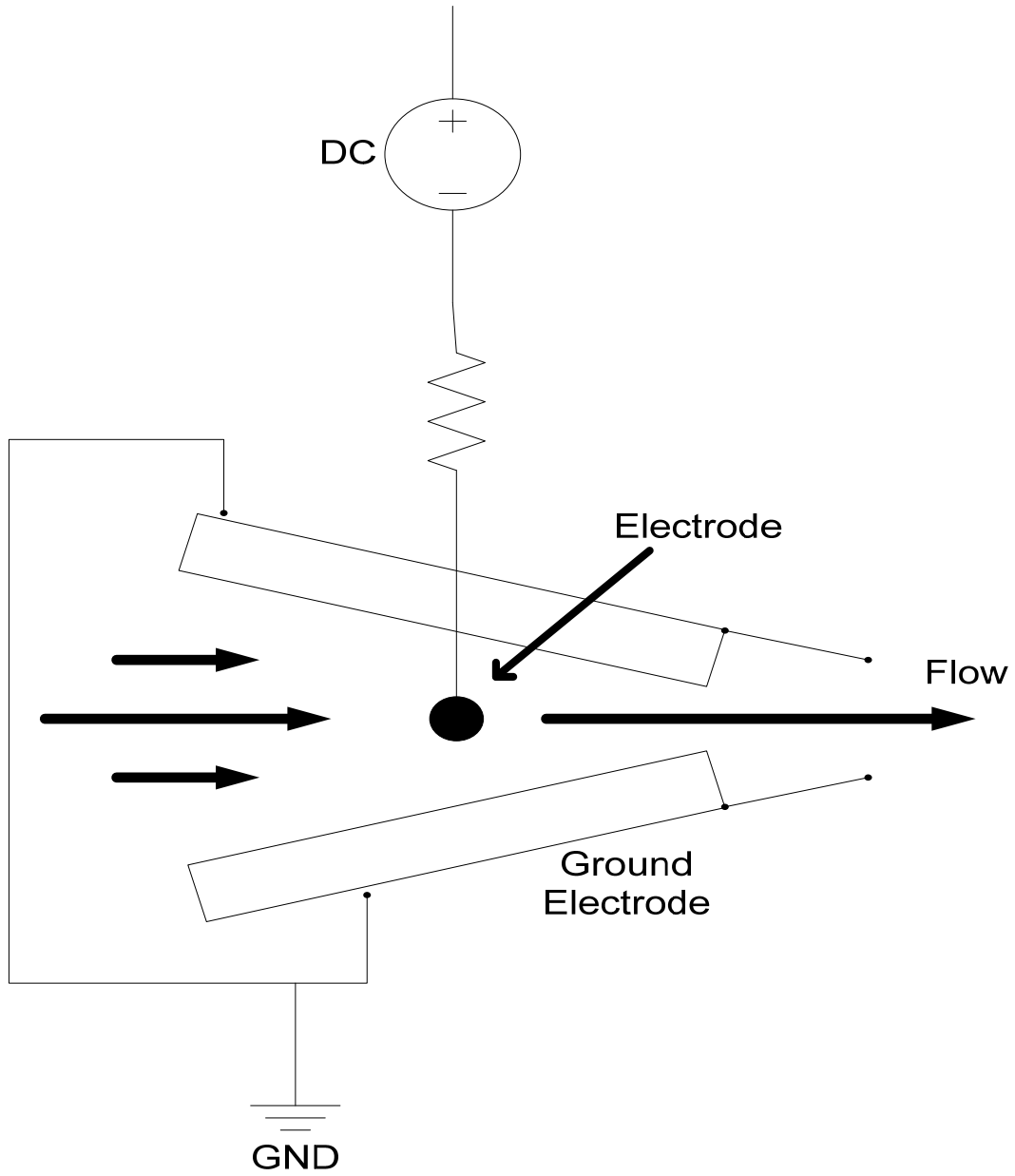


Figure 2.10: Schematic of a typical wire-convergent plate type EHD gas pump

3. Theory of EHD Enhanced Capillary Pumped Loops

In order to enhance heat transport in nuclear related extraterrestrial CPL applications this Chapter will review and assess the current design and theory of capillary pumped loops to determine what aspects of the design should be enhanced by the addition of EHD forces.

3.1 Capillary Pumped Loop

CPLs work on the principle of capillary action. Capillary action is the movement of a fluid through a thin tube called a capillary. Figure 3.1 shows how a capillary system works. The fluid will naturally travel through a capillary despite the presence of gravity, allowing fluids to be transported from one area to another without the use of mechanical pumps or natural circulation. In a CPL the capillaries are a porous wick, in the case of this work; the capillary network is a polyethylene wick. The wick is placed in the evaporator section of the CPL.

A CPL evaporator consists of a stainless steel outer shell, vapour channels, a wick and the working fluid, in this case Freon R134a. Figure 3.2 shows how the evaporator functions in a CPL. CPLs operate by applying a heat load to the outer shell of the evaporator. The fluid is heated causing it to evaporate. The vapour then travels through wick due to capillary action and into the vapour channels. Therefore the porosity of the wick is important as the pores must be large enough for the vapour to travel through easily, as not to become trapped in the wick, but also small enough to prevent the liquid from entering the vapour channels, while still allowing the wick to remain wet. The channels carry the vapour and heat to a condenser where the vapour is condensed into a liquid. The remaining heat then escapes to a heat sink removing the heat from the system. The liquid is returned to the evaporator or a reservoir tank.

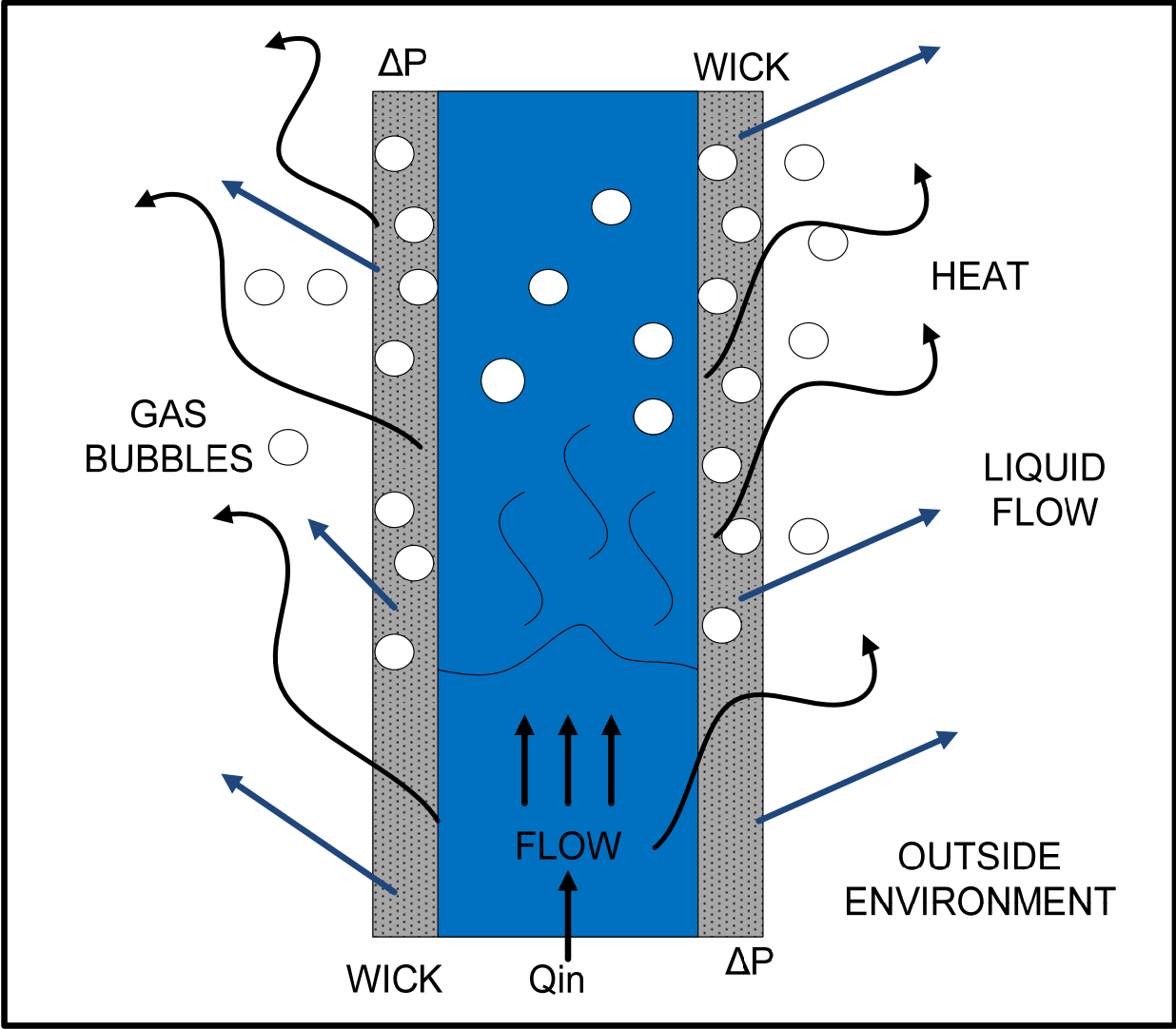


Figure 3.1: Schematic of Capillary Action appropriate to CPLs

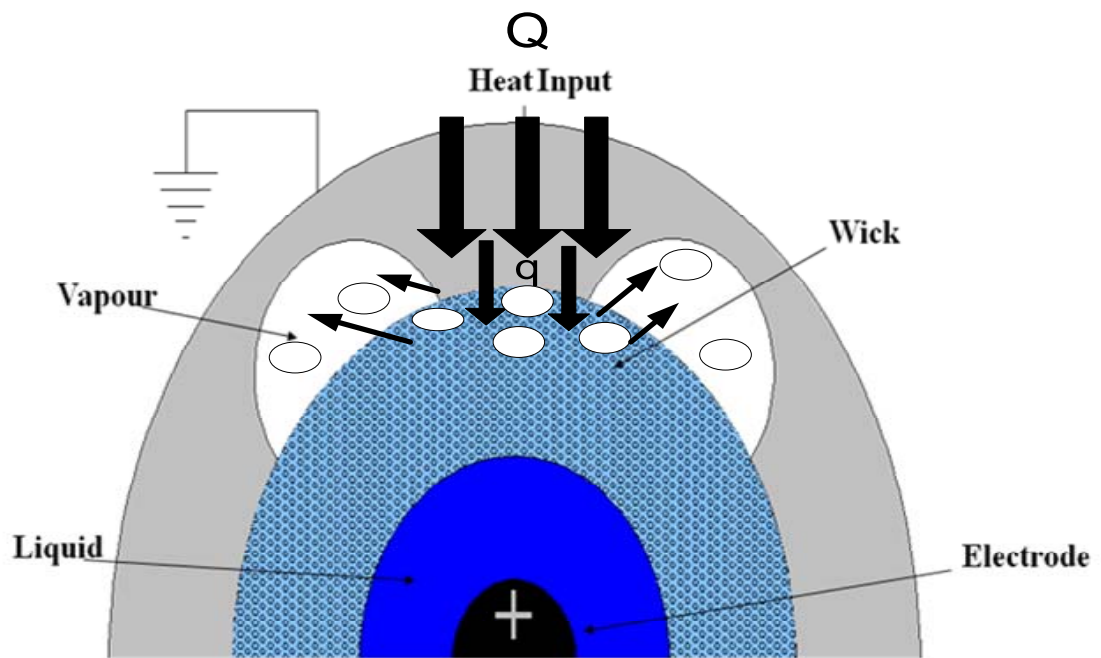


Figure 3.2: Cross Section of an EHD Evaporator showing heat flow and vapour generation

In the evaporator design it is also important to consider what boiling regimes will be present. As the boiling is the main mechanism for heat and mass transport, it must occur at a rate that allows the wick to remain wet, while still maintaining a vapour level in the evaporator that can sustain an effective rate of mass flow to the vapour channels. Importantly, if film boiling develops it can greatly reduce the heat transfer in the system and cause the wick to become dry. Film boiling occurs when bubbles form along an interface and create a film along the boundary between the two surfaces. Ideally, the evaporator would be design so that the vapour would enter the channels as a stratified or single phase flow, with a minimal amount of liquid entering the vapour channels.

The condenser is the other main component of the loop. The condenser is used not only to condense the vapour but in some designs to control the flow. Backpressure from the condenser can be used to control the flow from the evaporator. The design of the condenser is then significant as it is often the dominant component in terms of mass and heat transport. CPLs then can also use an EHD enhanced evaporator to improve the efficiency and performance of the CPL by placing an electrode into the centre of the evaporator. The outer shell then acts as the ground electrode. Next EHD forces are enacted on the working fluid by generating a corona along the centre electrode similar to Figure 3.2. The EHD forces create a charge between the wick and fluid at the interface. This generates a force that enhances the flow through the wick to the vapour channels. Chapter 3.3 explains how EHD forces affect the flow in CPLs, while Chapter 3.2 describes how EHD has been demonstrated to improve current CPL design and discusses its limitations. Other EHD devices such as EHD gas pumps can also be included in CPLs and are also discussed. EHD gas pumps ionize the gas molecules near the corona creating EHD forces that generate motion in contrast to the interfacial EHD forces acting in the evaporator.

3.2 EHD Enhanced Capillary Pumped Loop Previous Modifications and Design Issues

Capillary pumped loops are limited in their ability to transport heat by two key factors; their flow limits and dryout. The CPL's flow is limited in the vapour leg as the flow is controlled by the backpressure generated by the condenser. Improving the flow rates from the evaporator Chapter to the condenser would help improve the flow limits of the loop and increase its ability to transport heat efficiently. Previously, Shetelensky et al characterized and determined the behaviour of CPLs in their work [9]. Their conclusions initiated the concept of the inclusion of EHD forces to the CPL to improve efficiency. From here, further studies, such as Komeili et al, have demonstrated that the addition of EHD forces to the evaporator section can enhance the efficiency of heat transport in CPLs by improving their flow rates by a factor of 3 to 4 times without any significant increase in pressure drop by improving the transfer of fluid through the wick by creating extra force at the wick-fluid interface [17].

The other issue that causes limitations when using CPLs is wick dry out. The heat and pressure of the loop can cause the wick to dry out quickly and become damaged reducing the efficiency of the loop and its heat transport capabilities. The bubbles become trapped between the wick and outer shell and cannot escape to the vapour channels. The addition of EHD forces to the loop has experimentally shown to increase the time before dryout [16, 17]. As the introduction of EHD forces into the evaporator prevent the bubbles from becoming trapped against wick or wall by reducing bubble size and increasing bubble mobility, thus preventing film boiling from occurring. Currently, there are several proposed solutions to alleviate dry out including increasing the surface area of the vapour channels to adding lubricants to prevent dry out [9, 16]. The solution being considered for this work is to increase the EHD forces inside the evaporator. By increasing the EHD forces in the evaporator, the bubbles should be prevented from being trapped by reducing vapour build up and dryout within the wick. Also adding EHD forces outside the evaporator to enhance the flow rate

in the vapour leg is being considered to stabilize the condenser but may indirectly improve evaporator performance as well. However, further research and study is required to determine the extent EHD phenomena can reduce dryout and increase the time before dryout occurs.

3.3 Electrohydrodynamics

EHD motion, which has also historically been called ionic wind or corona wind, is motion induced by particles exchanging charge and momentum from forces generated by an electric field. As the historic names suggest the particles near the corona become ionized and move away from the electrode due to their similar charges and towards the ground electrode, which has the opposite charge of the corona electrode. As the ions move away from the corona electrode they collide with particles causing the particles to exchange momentum and charge. These collisions initiate motion in the direction of the ground electrode. Figure 3.3 displays a diagram of using the Coulomb force induction of EHD motion using a positive corona electrode. The phenomena present in Figure 3.3 are the dominant phenomena present for an EHD gas pump. Figure 3.4 presents the dielectrophoretic force acting at an interface. The phenomena in Figure 3.4 are the dominant phenomena in the EHD evaporator. The forces that influence this exchange of charge and momentum for EHD phenomena are known as EHD forces [9, 17, 60-63, 65].

EHD refers to the motion of a fluid generated by forces induced by an electric field. The EHD forces are generated from the applied electric field of high-voltage applications, for EHD forces to develop a device consisting of a corona electrode and a ground electrode must be connected to the power source. When the high voltage is applied to the corona electrode a corona is created and the resulting forces will then push a dielectric fluid in the direction of the ground electrode. The strength of EHD forces is dependent on several factors but will influence nearby molecules causing them to become ionized. The accelerated ionized molecules collide with neutral particles, exchanging momentum inducing a gas flow away from the electrical source [9, 17,45-49].

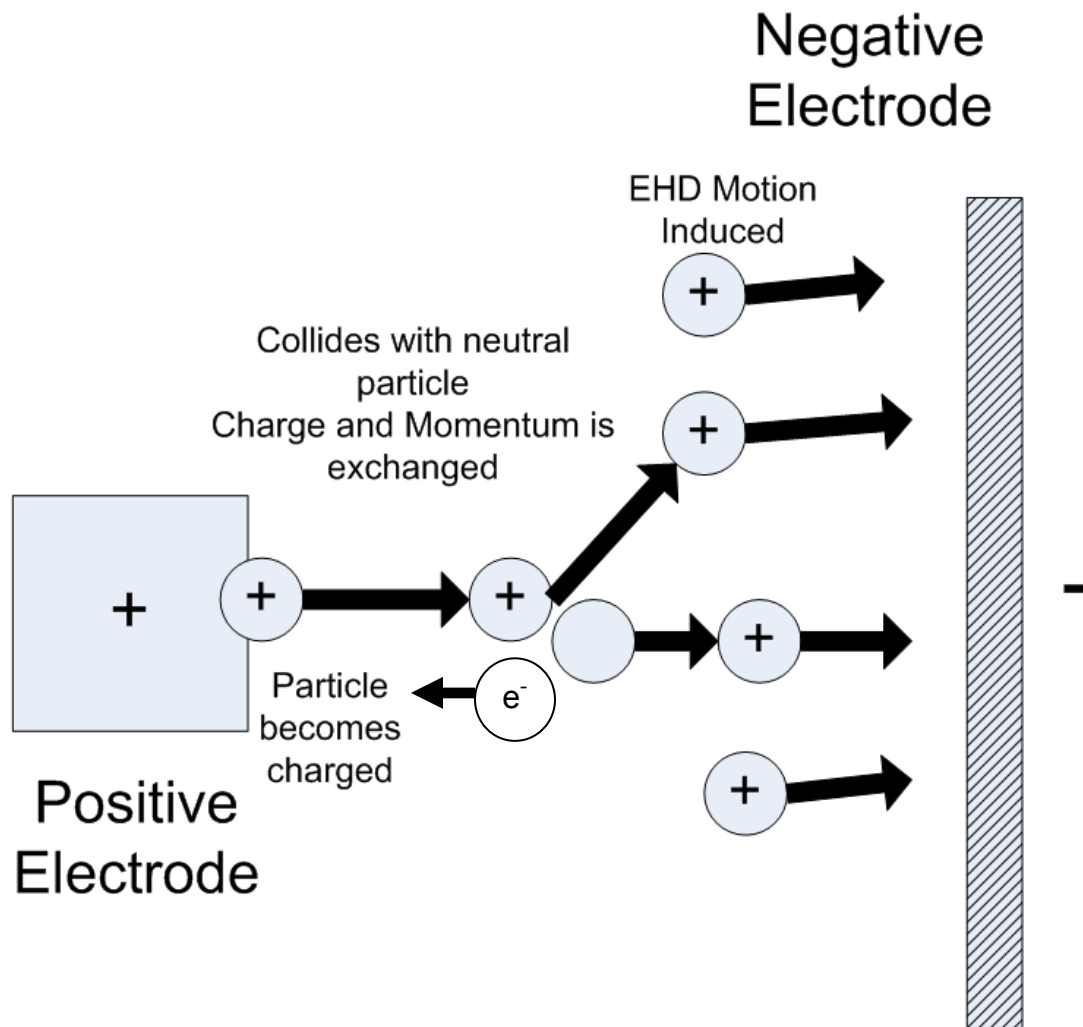


Figure 3.3: Diagram of Inducement of EHD Motion

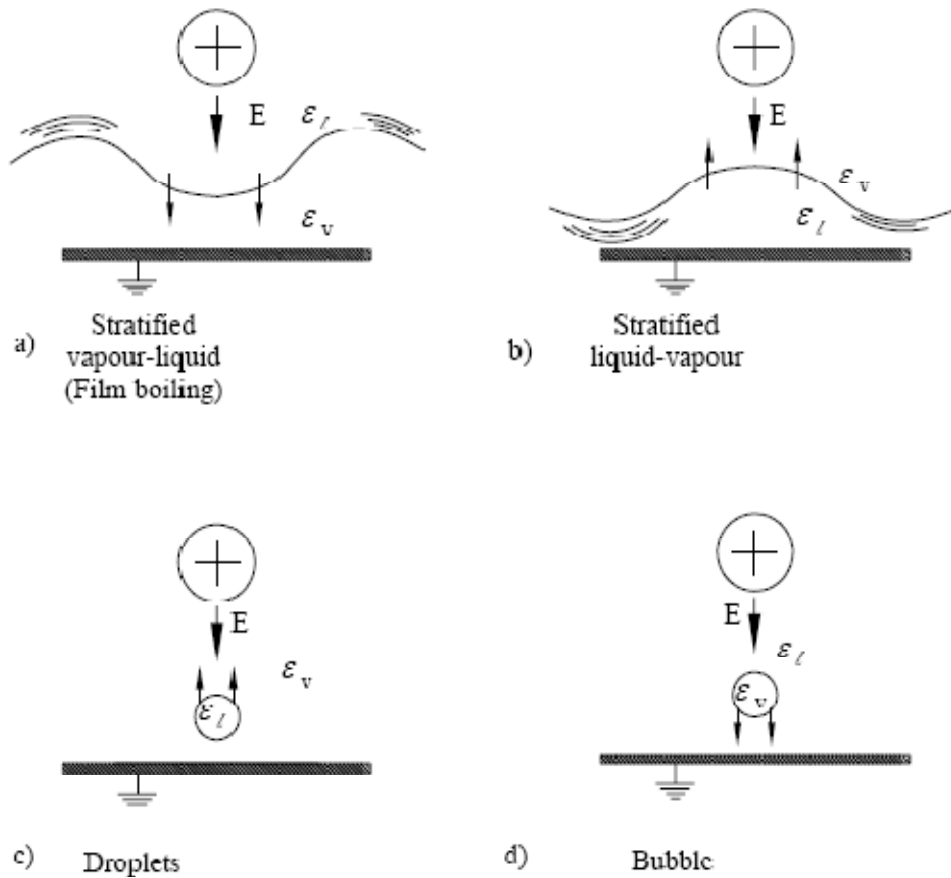


Figure 3.4: EHD instability on the vapour-liquid interfaces for a) stratified vapour-liquid b) stratified liquid-vapour c) droplets and d) bubble under wire-plate electrodes [17]

The electrical field is usually created by applying high voltage to an electrode. Under sufficient applied voltage, a corona type discharge can occur. The current created by a corona inciting the fluid motion in a gas. The force acting on the fluid causing motion is called the electrophoretic force [9, 15-19]. When multiple phases are present in the flow, the dielectric constant for each phase is different, adding additional force to the system known as the dielectrophoretic force.

EHD phenomena are governed by the following equations:

Mass Conservation

$$\frac{\delta\rho}{\delta t} + \nabla \cdot (\rho U) = 0 \quad (3.1)$$

The mass conservation equation has no direct impact on the electric field forces as the electric field is not dependent upon the mass of the material inside the electric field. However, it is an important fundamental equation as the resultant mass flow will be impacted by equation 3.1.

Momentum Conservation

$$\rho \frac{\delta U}{\delta t} + \rho(U \cdot \nabla)U = -\rho g\beta(T - T_s) - \nabla P + \mu_g \nabla^2 U + F_{EB} \quad (3.2)$$

The last term F_{EB} is the electric field force term. Therefore, the momentum while conserved is directly influenced by the electric field.

Energy Conservation

$$\frac{\delta T}{\delta t} + U \cdot \nabla T = \frac{\kappa}{\rho c_p} \nabla^2 T + Q_{EB} \quad (3.3)$$

Q_{EB} is the addition of energy (Joule Heating) from the electric field. This addition is due to the charge of the electric field.

Ion Transport

$$\frac{\delta N_i}{\delta t} = U \cdot \nabla N_i \pm \mu_{i\nabla} \cdot (N \nabla V) - D_i \nabla^2 N_i \quad (3.4)$$

The ion transport equation is an important fundamental equation when considering EHD flow and related phenomena as the ability of the ions to be transported has a direct effect on the strength of the EHD flow that can be generated. Since the ion concentration is proportional to the force induced in the momentum equation.

Poisson Equation

$$\nabla^2 V = \frac{-eN_i}{\varepsilon} \quad (3.5)$$

Equation 3.5 is used to determine the charge density and distribution of the electric field, which is needed to determine the strength of the EHD forces.

The force density changes from the electric field are as follows:

$$F_{EB} = p_{ie}E + J_x B - \frac{1}{2}E^2 \nabla \varepsilon - \frac{1}{2}H^2 \nabla \mu + \nabla \left[\frac{1}{2} \rho E^2 \left(\frac{\delta \varepsilon}{\delta \rho} \right) \tau + \frac{1}{2} \rho H^2 \left(\frac{\delta \mu}{\delta \rho} \right) \tau \right] \quad (3.6)$$

The equation can then be separated into five distinct components:

$$F_{EB} = F_1 + F_2 + F_3 + F_4 + F_5 \quad (3.7)$$

Where $F_1 = p_{ie}E$ is the force density due to the space charge

$F_2 = J_x B$ is the force density due to charged particle motion

$F_3 = -\frac{1}{2}E^2 \nabla \varepsilon$ is the force density due to the dielectric properties

$F_4 = -\frac{1}{2}H^2 \nabla \mu$ is the force density due to the fluid permeability changes

$F_5 = \left[\frac{1}{2} \rho E^2 \left(\frac{\delta \varepsilon}{\delta \rho} \right) \tau + \frac{1}{2} \rho H^2 \left(\frac{\delta \mu}{\delta \rho} \right) \tau \right]$ is the force density due to the electrostriction and magnetostriction effects

The energy terms from the Joule heating effect can be determined as follows:

$$Q_{EB} = (J - \rho_{ie}U)(E + U \times B) + \nabla \cdot [(E + U \times B) \times (H - U \times D)] + [E \frac{d}{dt} \left(\frac{D}{\rho} \right) + H \frac{d}{dt} \left(\frac{B}{\rho} \right)] \rho \quad (3.8)$$

where the first term is the heat generation due to charged particles, the second term is the energy due to the polarization and the third term is the energy due to the displacement current and time-varying magnetic fields. The importance of each term changes depending on the working fluid. Appendix B presents a table of the importance of each term.

As EHD motion is generated using high voltages and a low current, the electric field equation can be simplified for EHD motion by omitting the force terms related to the magnetic field as the electric field is the dominant force. The electric field force is represented by the following equation:

$$\vec{F}_{EB} = \rho_{ie} \vec{E} - \frac{1}{2} E^2 \nabla \epsilon + \nabla \left[\frac{1}{2} \rho E^2 \left(\frac{\delta \epsilon}{\delta \rho} \right)_T \right] \quad (3.9)$$

Equation 3.9 is the fundamental force equation of electrohydrodynamics. Each term represents one of the three forces of EHD. The first term is the Coulomb or electrophoretic force. This force is the primary acting force in an EHD gas pump and is described in Figure 3.3. The second term is the dielectrophoretic force and is the primary acting force in the EHD evaporator and is described in figure 3.4. The third term is the electrostriction force and is also present in the EHD evaporator and represents the EHD force generated by changing temperature or density. At any time in a system the three forces could be acting on the fluid causing motion, however often one force is more dominant at a specific point or region than the other forces [15]. To determine the effect each force has on a particular system, dimensionless numbers have been established to determine each term's influence on the system.

The Ehd number is a ratio that represents the relative strength of the electrophoretic forces compared to the viscous forces in the system. The Ehd number has the following equation:

$$Ehd = \frac{I_s L^3}{A \rho_f \nu_f^2 \mu_i} \quad (3.10)$$

Where I_s is the discharge current (A), L is the characteristic length (m), A is the cross-sectional area (m^2), ρ_f is the fluid density (kg/m^3), ν_f is the kinematic viscosity of the fluid (m^2/s) and μ_i is the ion mobility of the fluid ($m^2/V \cdot s$). For this work, the Ehd number of the EHD evaporator is currently has a value of 0 as the current is extremely small [16]. The effect of EHD number with respect to the EHD gas pump is discussed in Chapter 6.9

The ratio of the dielectrophoretic force to the viscous force is called the Masuda number and is represented by the following equation:

$$Md = \frac{\epsilon_0 E_s^2 L^2}{\rho_f \nu_f^2} \quad (3.11)$$

, where ϵ_0 is the permittivity of free space (F/m) and E_s is the reference electric field (V/m). For this work, the Masuda number has a value of 41.3 in the current EHD evaporator design [16]. For the gas pump as the flow is single phase the dielectrophoretic force is not strong and therefore the Masuda number is not calculated.

The last dimensionless number is the Electrostriction number and is the ratio between the temperature dependence of the dielectrophoretic force and the viscous force:

$$ES_E = \frac{\epsilon_0 E_s^2 L^2}{\beta \Delta T_s \rho_f \nu_f^2} \quad (3.12)$$

Where ΔT_s is the temperature gradient (K) and β is the thermal expansion coefficient (K^{-1}). For this work, the electrostriction number has a value of 65.8 in the current EHD evaporator design [16]. For the gas pump as the flow is single

phase the electrostriction force is also not strong and therefore the Electrostriction number is not calculated.

Often to determine how the forces are affecting the flow, the force components are compared to the EHD Reynolds number, which is a ratio between the inertial forces and the viscous forces and is defined as follows:

$$Re_f = \frac{\rho_f U D_h}{\mu_f} \quad (3.13)$$

Where U is the velocity of the fluid (m/s) and D_h is the hydraulic diameter (m).

The dimensionless numbers are usually compared as a ratio of the force component to the inertial forces. Using the Ehd number as an example, the ratio is usually expressed as $\frac{Ehd}{Re}$ or $\frac{Ehd}{Re^2}$. The ratio for this system using this example is 0, while the ratio between the Masuda Number and the Reynolds number squared is 8.7×10^8 . The ratio is then able to demonstrate that the dielectrophoretic force is acting as the dominant force, while the electrophoretic force is unable to overcome the thermal buoyancy forces in the evaporator [16].

However, as the main design changes being studied are the introduction of an EHD gas pump to the vapour leg and increasing the characteristic length of the electrode. A brief description of the how the theory involving these changes will affect the CPL shall be provided. EHD forces are directly proportional to the characteristic length of the electrode. Therefore, the enlargement of the diameter of the electrode in the evaporator could further improve the heat transport efficiency of the loop, while allowing the EHD evaporator to maintain the favourable design features of CPLs by having no moving components and low power requirements. The addition of an EHD gas pump to the vapour leg is being research as part of this project to improve the heat transport efficiency of the vapour travelling from the evaporator section to the condenser. EHD gas pumps consist of a chamber with an electrode. The ground plates are then designed to create an electric field that will push the vapour from the inlet to the outlet of the pump. The gas pump could allow the flow rate and flow pattern from

the evaporator to the condenser to be stabilized and controlled. A properly designed gas pump could allow for a reduction of backpressure from the condenser and improved heat transport efficiency. The effects of the dimensionless numbers on the EHD gas pump are present and discussed in Chapter 6. However, while in the evaporator the dielectrophoretic force seems to be driving the flow in EHD gas pumps the dominant force is the electrophoretic force.

4. EHD Capillary Pumped Loop Design

This Chapter details the current EHD enhanced CPL configuration, assessment of the deficiencies in the previous work and details the proposed design changes and areas of study for the current work. The current EHD enhanced CPL setup is described in Chapter 4.1. The experimental portion of the design analysis is described and discussed in detail in Chapter 4.2. The design changes that are being studied for implementation in the EHD-CPL are then described in Chapter 4.3 for the evaporator and in Chapter 4.4.1 for the condenser. The assessment will focus on two issues. The first issue is the CPL work performed by others has weak performance during application of EHD conditions. Therefore the evaporator test section needs to be examined to determine the cause of the weak performance. Secondly, the CPL's performance is unstable due to the backpressure generated from the condenser. The entire vapour leg and condenser therefore also needs to be examined for potential areas of improvement.

4.1 Current Capillary Pumped Loop Design

The current experimental CPL apparatus consists of several components. The EHD enhanced evaporator is the primary component of the loop. The evaporator receives the fluid from the charging tank; this section between the charging tank and the evaporator is known as the liquid leg. The liquid enters the evaporator where it boils and leaves via vapour channels and enters a pipe. Electrical heater bands are attached to the outer shell of the evaporator. The bands are the heat source for the evaporator. A condenser is attached to the evaporator by a pipe this is known as the vapour leg. In between there is a valve to prevent the flow from entering the condenser when the working fluid is being recovered. The piping for the vapour and liquid legs is stainless steel. Pressure relief valves are located on the condenser to vent the working fluid to the atmosphere if there is a pressure overload emergency situation. A liquid reservoir tank and a liquid charging tank are located at the beginning of the liquid leg. The reservoir tank is

used to store the working fluid when the loop is not in operation and is attached via piping to the charging tank and the condenser. The section of piping from the condenser to the liquid return tank is known as the liquid return leg. There is a valve in the return leg to isolate the condenser from the reservoir tank, this mostly to allow for a quicker recovery process when draining the tank of the working fluid. The liquid charging tank is then connected to the evaporator using a stainless steel pipe and a small section of Teflon tubing at the evaporator entrance. A schematic of the loop is presented in Figure 4.1. The working fluid for the loop is Freon R134a. The evaporator is of the same design described in Figure 3.2 consisting of a stainless steel electrode, polyethylene wick with a porosity of 20 μ m, and a steel outer shell with vapour channels. The heater bands are attached to the outside the evaporator using a thermal conductive putty. The temperature is measured at the inlet and outlet of the evaporator and the pressure is measured across the evaporator. A sight tube is present in the liquid return leg to observe the flow regime and determine if the flow is two-phase or single phase.

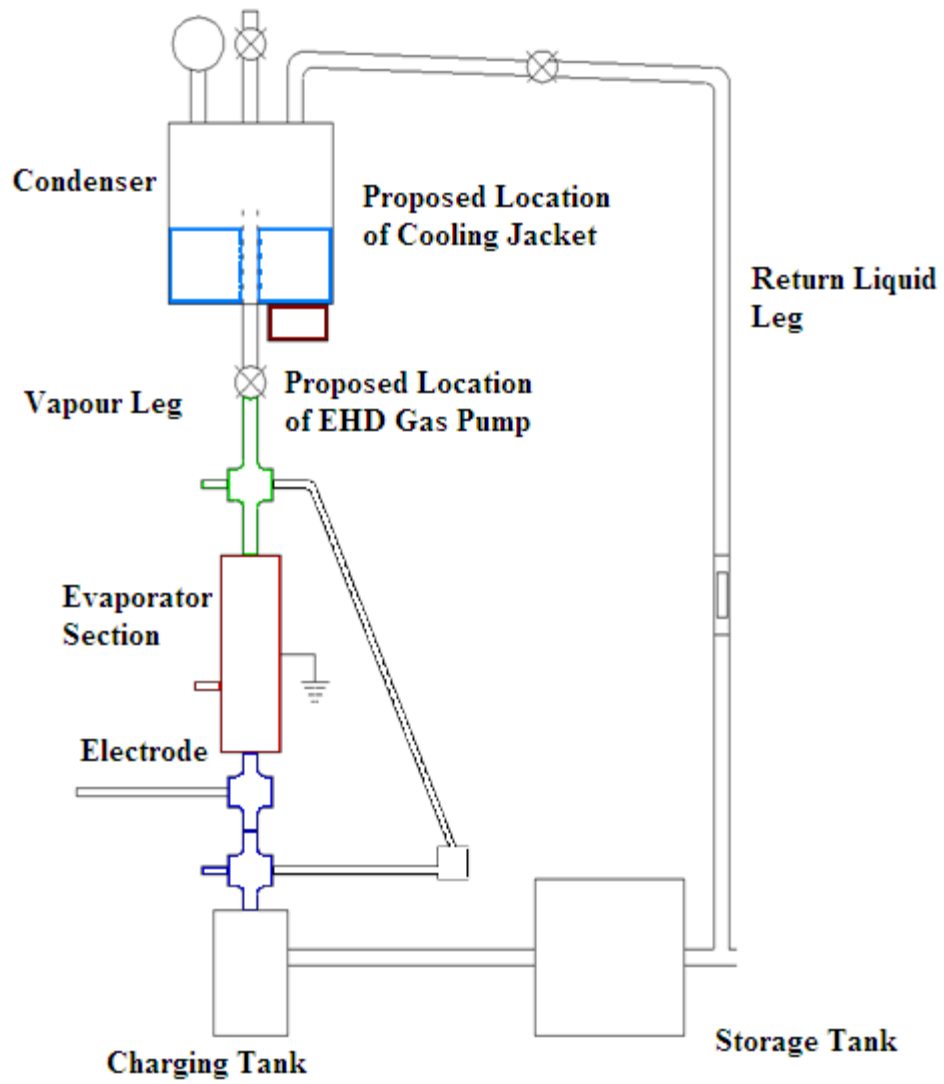


Figure 4.1: Diagram of CPL with EHD enhancement

4.2 Experimental Analysis of Capillary Pumped Loop

Komeili et al. performed experimental studies with the EHD enhanced CPL setup in 3 different operating modes; no EHD, sustained EHD and pulsed EHD [17]. As previously stated in Chapter 2 Komeili et al. demonstrated there was improvement in CPL performance of 3 to 4 times with minimal pressure drop with the addition of EHD forces but this improvement could not be maintained for sustained periods. We performed a review of Komeili et al.'s experimental results to identify the issues for why EHD enhancement could not be maintained. This section will identify the results of this investigation.

Based on these results it was determined there were several limitations in performance with the current design in regards to dry out and mass flow rate. They observed the wick had been dried out and damaged prematurely. Performance of the condenser was found to be unsteady and the performance of the evaporator could not reach steady state conditions. Hence, the impact of adding an EHD force for prolong periods such as during operations in a space type nuclear reactor was unclear. Furthermore, no conclusions were drawn on how to resolve these issues and no further work by Komeili et al was performed. Therefore an initial design analysis is required as part of this work to resolve the issues previously discovered with the experimental loop. The design analysis incorporates several experimental and analytical techniques to identify the cause of these limitations and to decide on methods to resolve these issues. The results of the design analysis are presented in 4.2, 4.3 and 4.4.

The first stage of this work's design analysis is a visual inspection of the damaged wick to confirm Komeili et al.'s observations and to determine the cause of the damage. The wick clearly has burn damage along the outside and at the ends and also shows signs of heat damage. An image of the damaged wick and an undamaged wick is presented in Figure 4.2, while examples of the damage found is displayed in Figure 4.4. From Figure 4.2 it is clear the damaged wick is much smaller and more worn than the undamaged wick. The size difference is due to the damaged wick had been cut to a smaller size. Still it is

apparent the wick has suffered severe heat damage. Looking at Figure 4.4 burn marks can be seen running axially along the wick where the wick contacts the metal shell of the evaporator. Burn marks are most noticeable at the end of the wick where the heat has also caused deformation. The wick is no longer circular Figure 4.4b clearly displays the deformities of the wick and the eccentricity of its current shape.

Next an internal investigation of the wick's structure was performing using a scanning electron microscope at 180x magnification. An image of the internal structure of the damaged wick under magnification is displayed in Figure 4.3. The general internal structure and porosity was determined to be more than adequate more for the purposes of the CPL. However, while the porosity channels exist some are sealed due to heat damage reducing the available pathways through the wick. The wick must be replaced and precautions taken to prevent future heat damage.

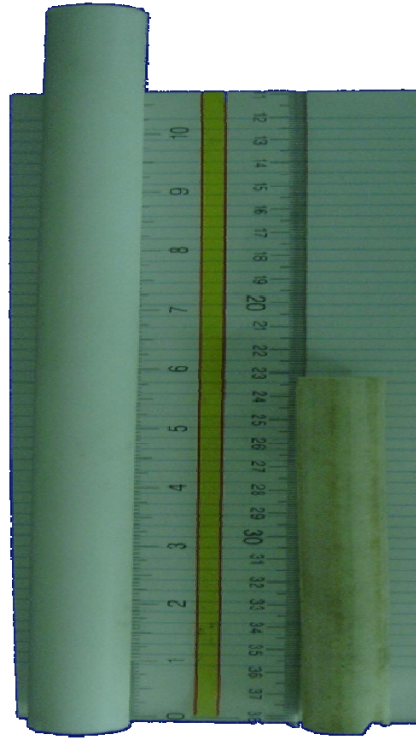


Figure 4.2: Comparison of undamaged wick (left) to damaged wick (right)

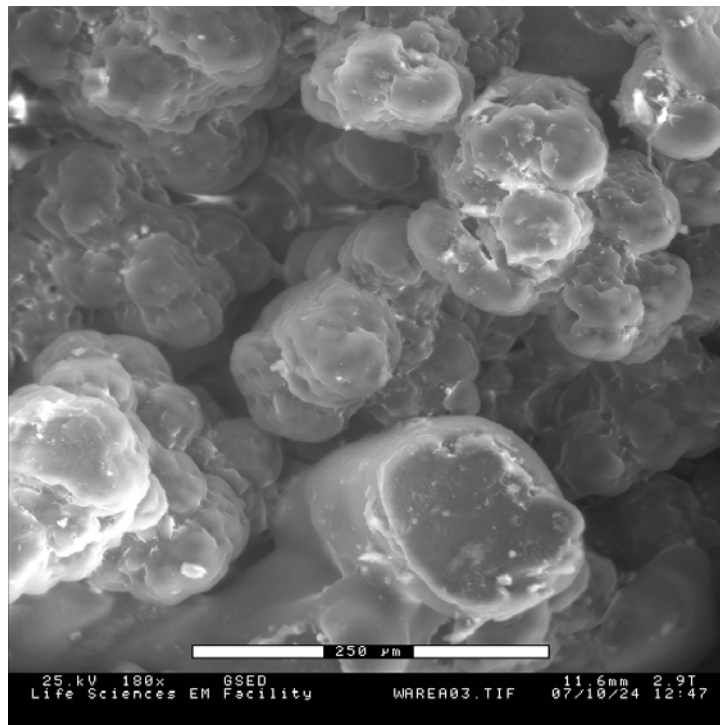


Figure 4.3: 180x magnification of a polyethylene wick

:

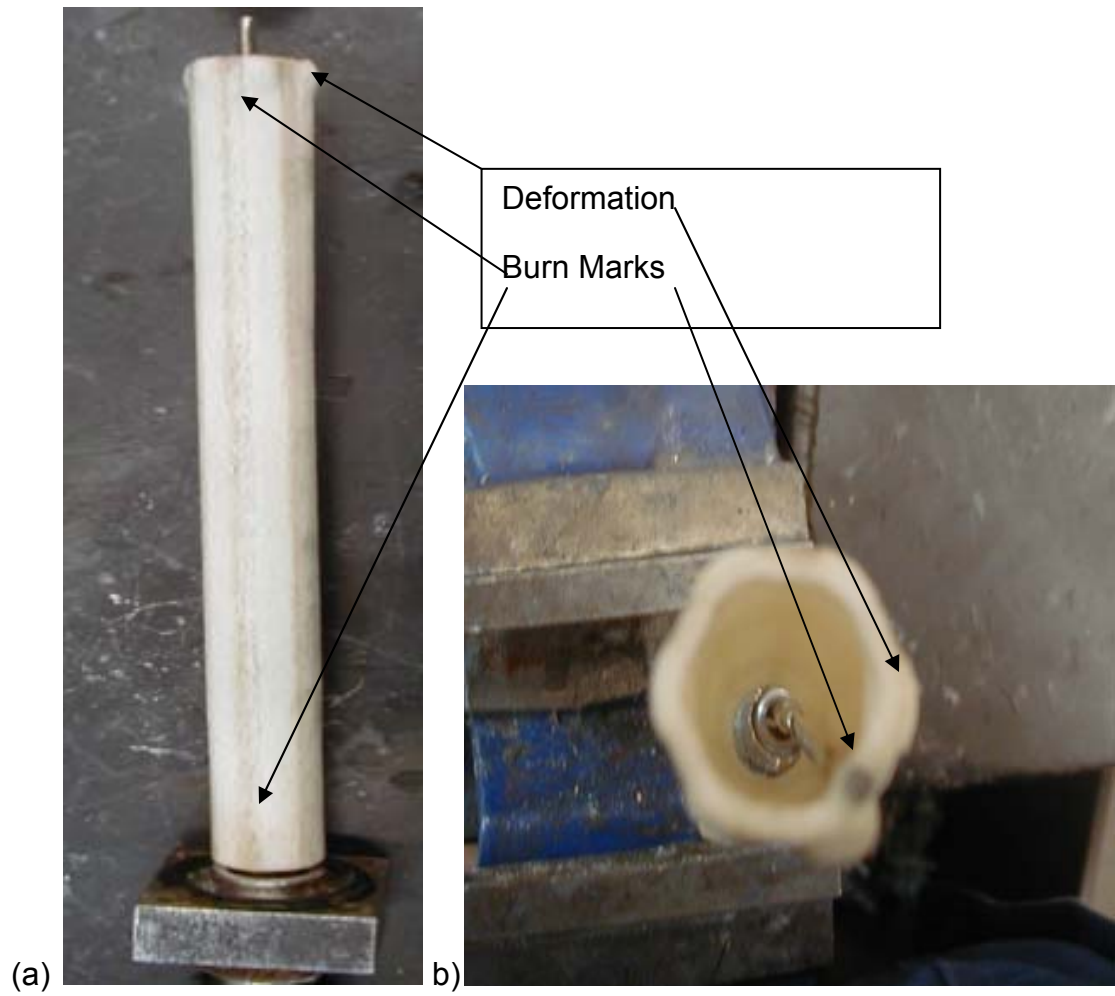


Figure 4.4: Damaged Wick (a) side view (b) top view

4.3 Evaporator Design

The evaporator is the key component of the loop responsible for boiling the liquid and then transporting the vapour and heat to the condenser. This Chapter will look at changes made to the evaporator design with respect to the wick and its positioning and to the design of the electrode and its diameter.

4.3.1 Evaporator Wick

The visual inspection of the wick confirmed the wick-outer shell contact was causing the wick to become damaged and causing the wick to have poor performance. However, the visual inspection did not determine any evidence of the mechanisms causing this damage and it did not fully explain the evaporator's weak performance. One proposed explanation is the spring present in the evaporator, which is used to form a tight seal between the wick and inlet of the evaporator, had been weakened by the Freon and is not strong enough to form a tight seal. The next step was to examine the internal structure of an assembled evaporator to ensure there is a proper fit. A non-destructive testing technique will be used to determine if a proper fit was achieved. In this case neutron radiography was considered the most appropriate technique available [50-56].

Neutron radiography is an established non-destructive testing technique similar to an X-ray radiography that creates an image of the internal components of an object. However, instead of X-rays penetrating the object neutrons are used. The neutrons travel through some types of material and are absorbed in other types of materials. Therefore an area with high neutron absorption appears black while in area where neutrons completely penetrate an object appears white. A camera indirectly then measures the neutron intensity and generates an image called a radiograph. Neutron radiography is particularly useful in this case as it can penetrate steel objects such as the evaporator while an X-ray could not [50-51]. Figure 4.6 displays a photograph of a disassembled evaporator and components, while the radiography apparatus used is displayed in Figure 4.5.

First radiographs of the evaporator were taken with the damaged wick inside. The radiograph of the evaporator with the damaged wick can be seen in Figure 4.7. The radiograph was taken at McMaster University. For the methodology used in the radiography process see Appendix D.

The initial investigation by neutron radiography found a gap between the inlet and the wick, which was determined to be the principal cause of the premature dryout at the top of the wick and a significant contributor to the mass flow rate being limited. The gap was measured to be 3.5mm. In order to resolve the gap a new longer wick was added and a longer Teflon plug was inserted to remove the gap. Again the assembled evaporator was taken to McMaster University for neutron radiography to see if the design changes had been effective. Radiographs of the evaporator with the undamaged wick and longer Teflon plug are presented in Figure 4.8 and 4.9. In the second set of radiographs a heater band is present while in the first set the heater bands were removed. The addition of the heater band had no impact on the quality of image or analysis. The evaporator and its subcomponents are easily identifiable.

Upon initial inspection of the processed image the components of the evaporator: end fittings, metal shell, inner polyethylene wick, heater band and Teflon plug are all clearly visible. A diagram identifying the components is seen in Figure 4.8. The image was then compared to the initial radiograph displayed in Figure 4.7. Two obvious differences are apparent besides the present of a heater band in Figure 4.8 and the presence of the electrode in Figure 4.7. The setup lacks the spring present in the initial image between the plug and the right end fitting. The missing spring was not discovered until the radiographs were compared. The second is the space or gap between the wick and the left end fitting. In the previous design this gap was determined to have dryout effects causing damage to the wick during operation. In the new design the radiograph shows the gap is considerably smaller. Using visual inspection the gap issue appears to have

resolved. In order to confirm this observation a line profile analysis of the gap was performed. The line profile is consistent across the gap and is measured at 6 pixels. The consistency suggests the gap is of a consistent material. The pixels can be used to approximate the size of the gap using the following equation:

$$\text{Size} = \text{Pixels/Resolution} \quad (4.1)$$

The gap size is then approximated as $6\text{px}/300\text{ppi} = 0.5 \text{ mm}$ compared to the gap in Figure 4.7 which was measured to be 3.5mm. The error in this calculation is considered +/- 0.1mm. Therefore the line profile analysis confirms that the design change has resolved the gap. The inclusion of a new spring in the design to replace the missing one is expected to close the gap entirely creating a tight seal between the wick and the end fitting.

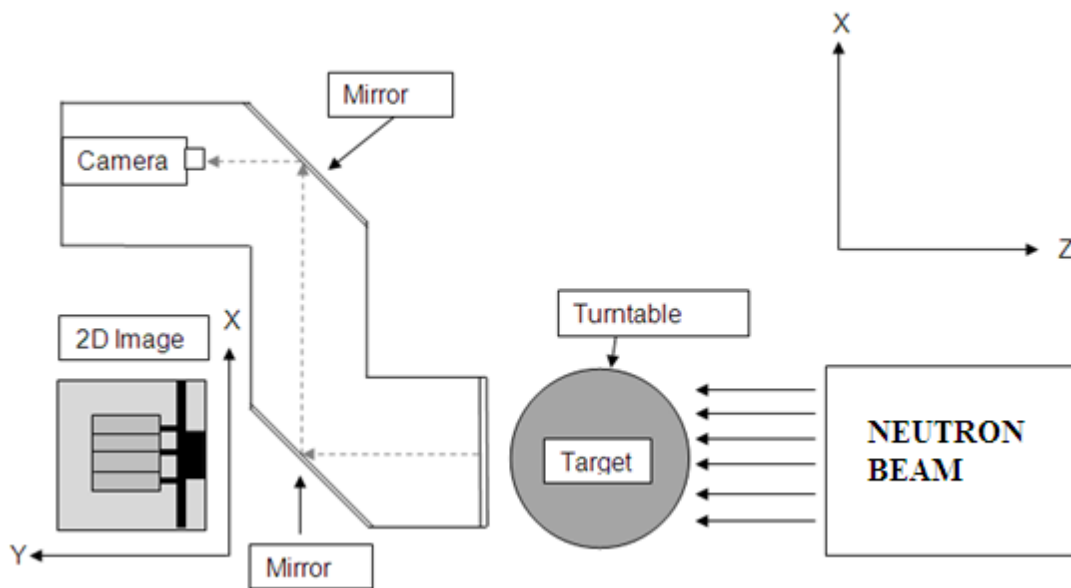


Figure 4.5: Neutron Radiograph Setup

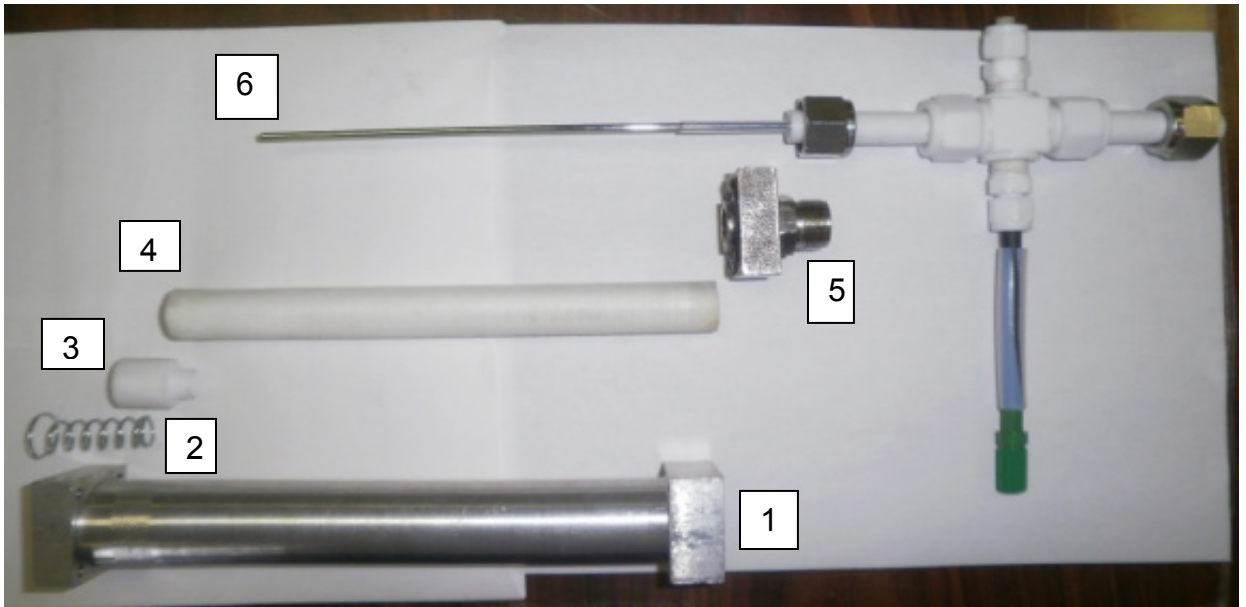


Figure 4.6: EHD Enhanced Evaporator Components: 1) Evaporator outer shell, 2) spring, 3) Teflon plug, 4) polyethylene wick, 5) end plug, 6) electrode

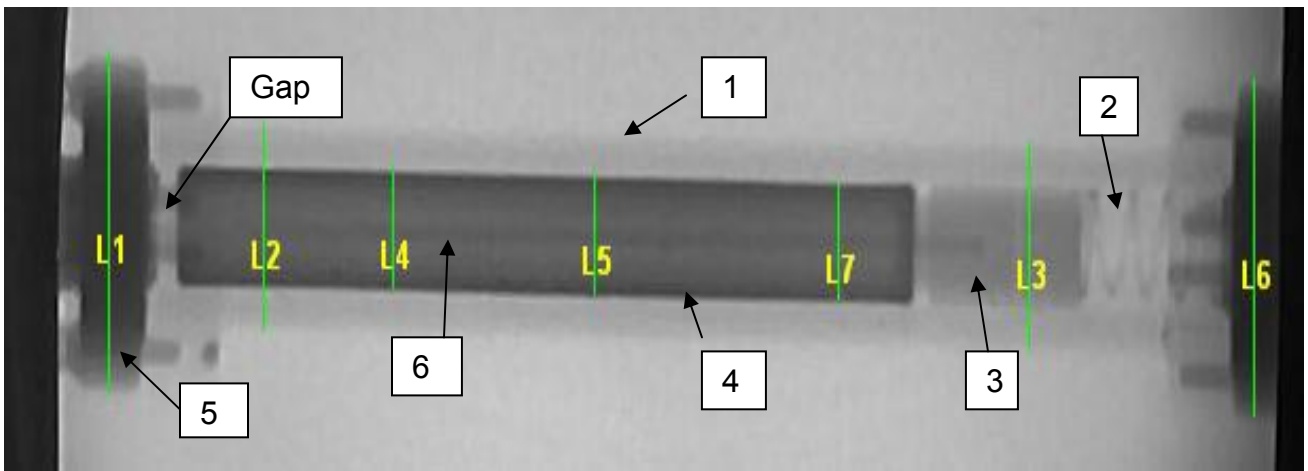


Figure 4.7: Radiograph of evaporator with damaged wick: 1) Evaporator outer shell, 2) spring, 3) Teflon plug, 4) polyethylene wick, 5) end plug, 6) electrode

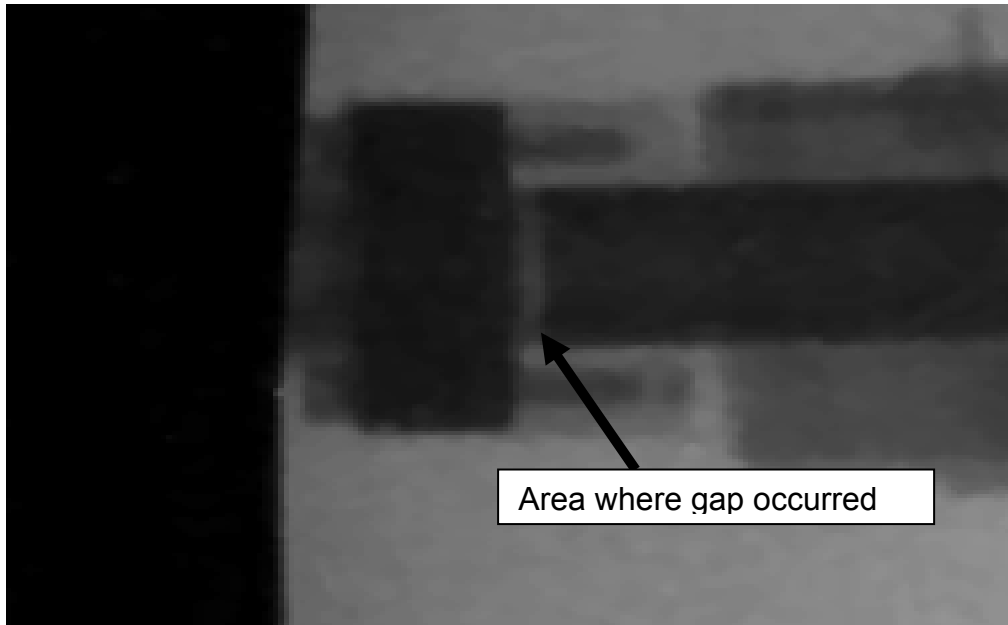


Figure 4.8: Close-up of evaporator end section with gap resolved

4.3. 2 Evaporator Electrode Design

The electrode design will be changed based on the design analysis to increase the EHD forces and phenomena occurring in the electrode region of the evaporator and thereby increase the EHD forces in the entire evaporator. The simplest and most effective way to increase EHD forces is to increase the characteristic length of the electrode as this improves the strength of the Ehd number to the 3rd power, the Masuda number to the 2nd power, and the Electrostriction number to the 2nd power as shown in Equations 3.10 to 3.12. Using the dimensionless numbers to demonstrate Figure 4.10 presents the relationship between the characteristic length and EHD forces. The figure clearly displays a strong dependency between the Masuda number and Electrostriction number in respect to increasing characteristic length. The Ehd number is 0 at all lengths as it has been determine that there is no significant discharge current occurring in the electrode region of the evaporator and the electrophoretic force or the effect of space charge is weak in this case.

In the case of the evaporator electrode the characteristic length is the diameter of the electrode. The key dimensions of the evaporator section of the CPL are presented in a schematic of the evaporator in Figure 4.9. The inlet and outlet around the electrode is 12.7mm. Therefore, the increase in diameter is restricted by the diameter of the inlet. Another consideration is if the diameter is too large it would reduce the flow area to an insufficient level causing the flow rate to be limited and also cause an increase in pressure. Therefore an electrode with a diameter 6.4mm, which is about 50% of the flow area but is a 100% increase in electrode diameter, is recommended. An added benefit of choosing a 6.4mm diameter is most metal rods come in a stock size of 6.4mm instead of choosing a diameter where a custom rod would need to be machined.

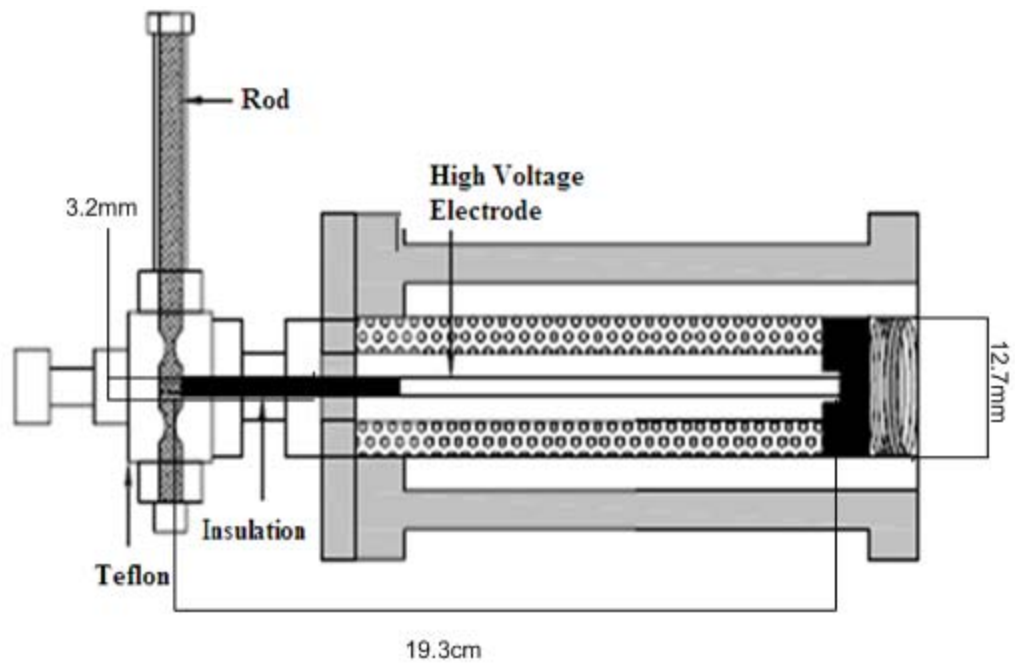


Figure 4.9: Schematic of EHD Evaporator for the Capillary Pump Loop

EHD Dimensionless Numbers vs. Characteristic Length for the Electrode Region of a EHD Enhanced CPL

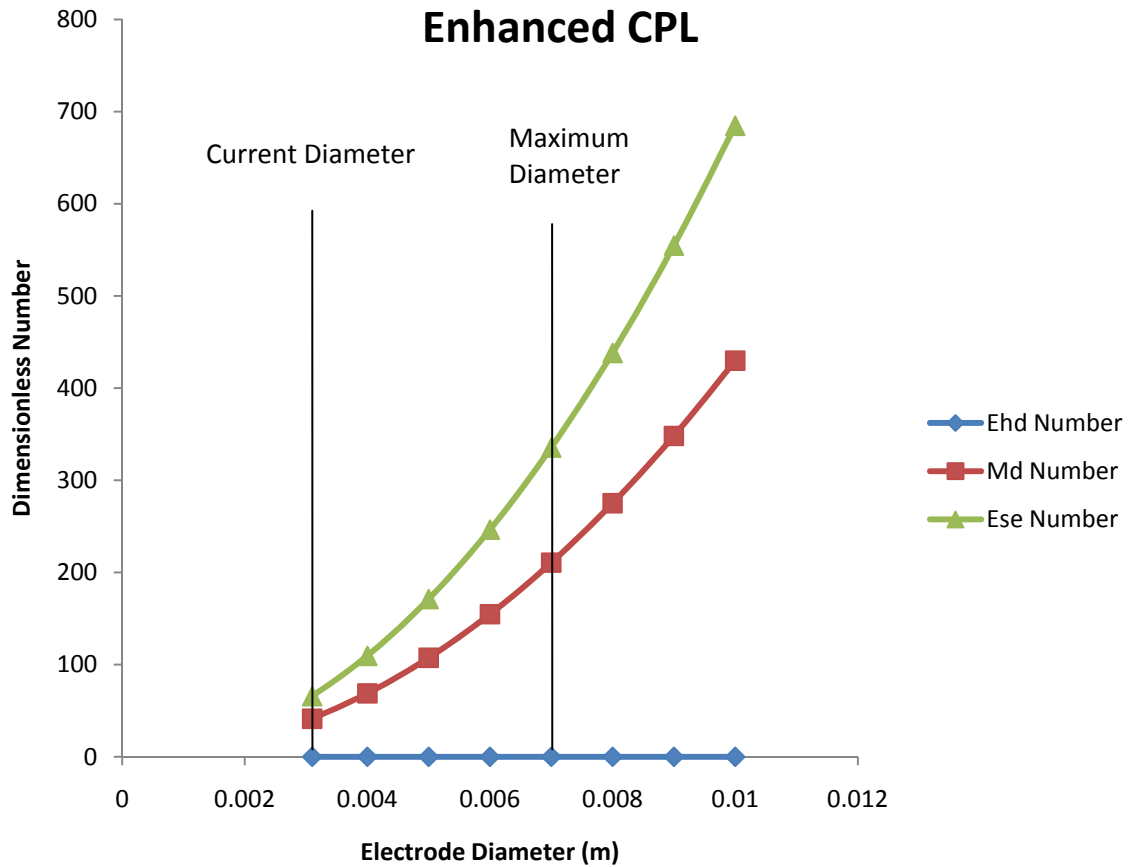


Figure 4.10: Relationship between Electrode diameter (characteristic length) and EHD forces

Table 4.1: Dimensionless Numbers of Electrode Region of Evaporator

| Dimensionless Number | 3.2mm (Current Diameter) | 5(mm) | 6.4mm (Maximum diameter using current evaporator) |
|----------------------|-----------------------------|---------|---|
| Ehd | 0 | 0 | 0 |
| Md | 41.3 | 107.4 | 176 |
| Es_E | 65.8 | 171.2 | 280.5 |
| Md/Re^2 | 8.7E+08 | 2.3E+09 | 3.71E+09 |

Next, in order to determine the optimal balance between flow area and electrode diameter experimental analysis will have to be performed. It is thus a recommendation that the electrode diameter should be adjustable so that various diameters can be investigated. The electrode will be made adjustable by having the majority of the electrode (7cm) screw off from the base, which is attached to the support rod. The new electrode will support diameters of 3.1mm, 4.8mm and 6.4mm, however other diameters can be supported from machining of wire stock. Diameters greater than 6.4mm would require an increase in the size of the support rod for it be achievable. Secondly the current electrode is poorly constructed in such a way that the electrode is not fixed and the connection between the support rod and the electrode is not sufficiently secure. In both cases, these issues could be sufficiently significant enough to cause a reduction in efficiency. The new electrode's support rod will be fixed at both ends as to prevent movement of the electrode. The base of the electrode will be soldered to the support rod in the new design to improve the security and connection of the electrode. These two additions to the design will improve the overall improvement of the evaporator. Figure 4.11 is a schematic of the proposed electrode design for future experiments. The electrode is ready to be built and tested to validate and verify the design changes and to study the effect of electrode diameter on the efficiency of an EHD enhanced CPL. Once the research on the gas pump is complete then the integrated system can be tested.

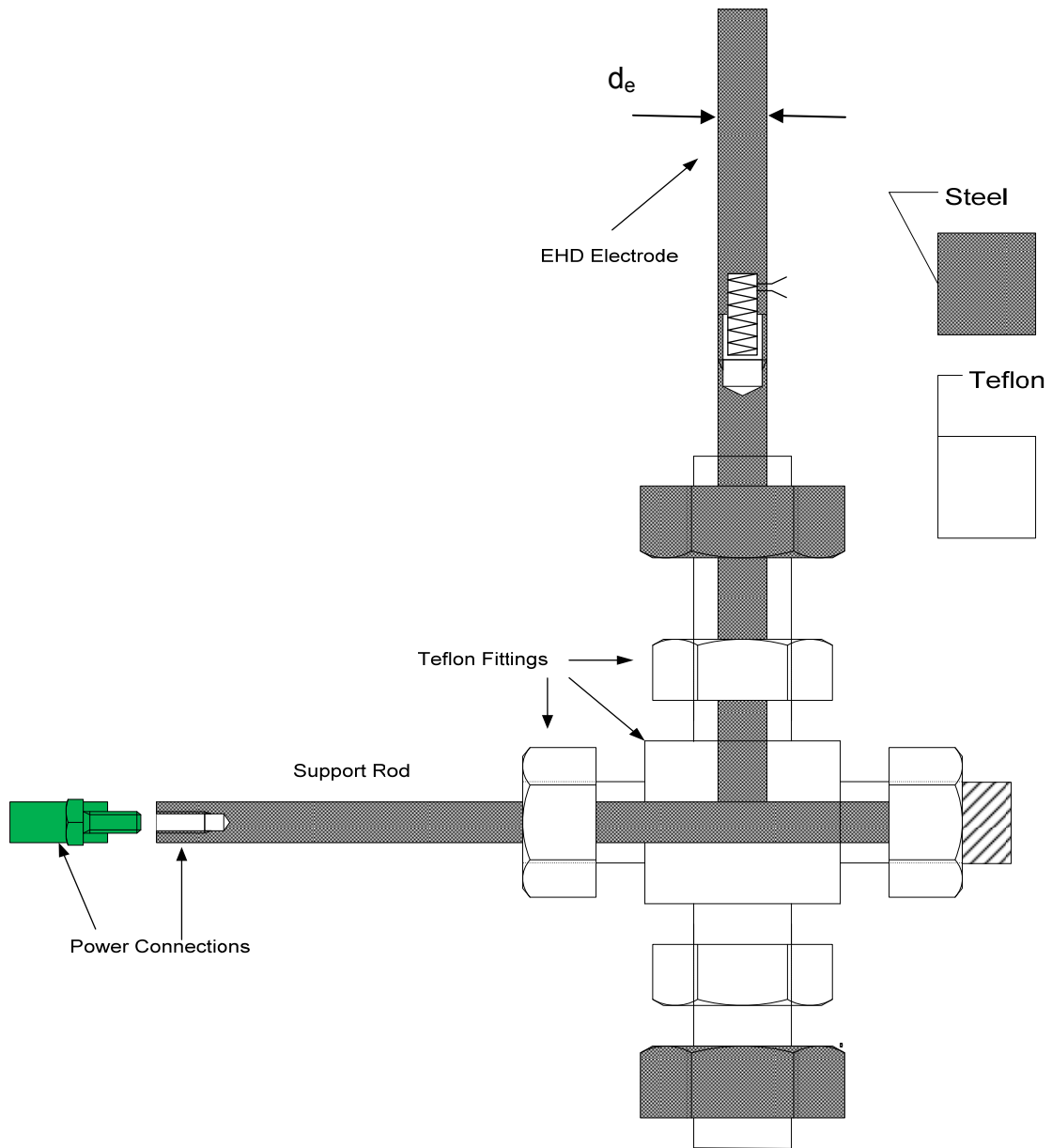


Figure 4.11: Schematic of Proposed EHD Electrode with Teflon Connectors

4.4 Vapour Leg and Condenser

The condenser is a critical component of the loop. Having a sufficient flow rate to the condenser is crucial to the loop and the evaporator operating more efficiently and effectively. This Chapter will look at the design changes to the vapour leg and the condenser.

4.4.1 Cooling Jacket

In the previous work there was a significant disparity between the condensation and evaporation rates, which was affecting the performance of the CPL [17]. In order to improve the performance and control of the condenser a cooling jacket was added to the condenser to reduce the wall temperature. Plastic tubing is wrapped around the outside of the condensation tank. The tube is attached to a water source and a reservoir tank. The condenser outer wall is cooled with ice packs to about 12-16°C before operation. During operation depending upon the heat being applied, the jacket wall temperature can reach up to 25°C with an average of 20°C. The water running through the jacket during operation is 16°C. However, it is dependent upon the water source. Initial results have shown the jacket can cool the condensate tank during the filling and recovery process although there is a need to improve the efficiency and performance of the jacket and cooling process for future experiments. The main issue seems to be the jacket is unable to cool the condenser quickly enough to compensate for the heat gained during charging of the loop and experimentation. If the condenser and jacket begin at a cooler temperature this could alleviate the issue. After charging the experimentation usually begins at 20°C. If the jacket could maintain the condenser at a temperature of 16-18°C there would be improved performance as the R134a can begin to boil at the current temperature and pressure. The easiest solution to this issue would be to increase the surface area of the cooling jacket and use colder water, preferably 4-8°C. Figure 4.12 shows a photograph of the cooling jacket attached to the condensate tank.

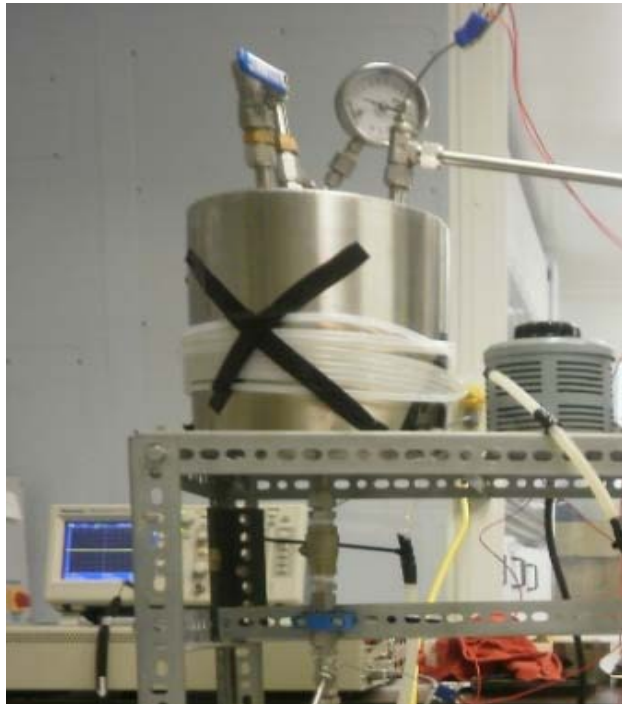


Figure 4.12: Picture of Condenser with Cooling Jacket

4.5 EHD Gas Pump

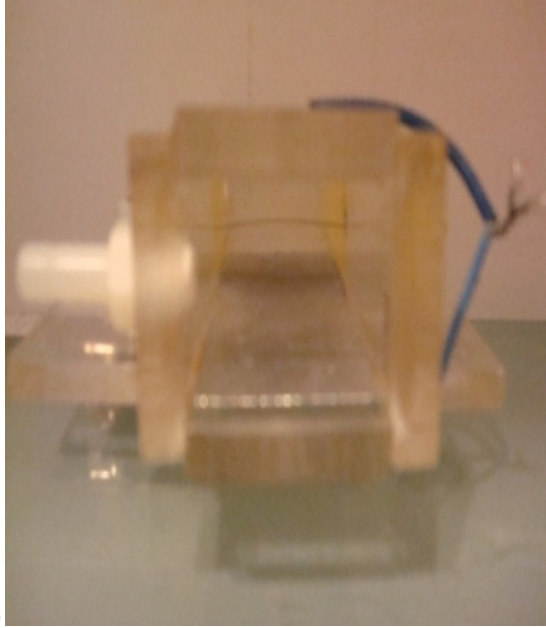
In the experimental EHD enhanced CPL for a space nuclear reactor the gas pump is to be placed in the hot leg or vapour section of the loop to transfer the vapour from the evaporator to the condenser. Figure 4.13 shows a picture of a typical EHD gas pump.

Before the EHD gas pump can be added to the loop the desirable qualities and limitations of the gas pump in a CPL for extraterrestrial applications need to be established as well as the requirements and the design of the EHD gas pump for the experimental EHD enhanced CPL also needs to be determined. Figure 4.14 shows the general vicinity in which an EHD gas pump will be located.

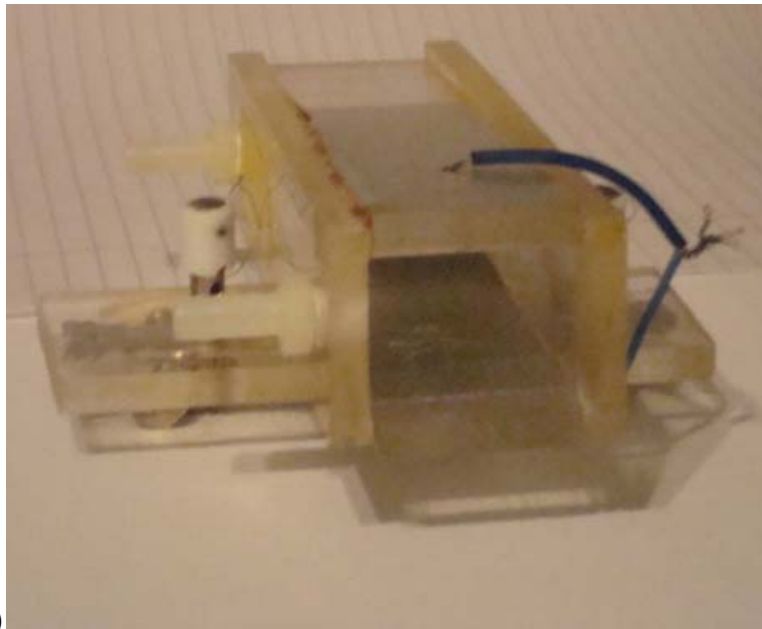
The main requirement for the inclusion of an EHD gas pump in an CPL for an extraterrestrial nuclear reactor is that the addition of the pump does not affect the factors mentioned in Chapter 1 that make a CPL a desirable design for extraterrestrial applications. Therefore the EHD gas pump must accomplish these following requirements:

- Does not significantly increase the power requirements of the CPL
- Does not significantly increase the weight or space requirements of the CPL
- Functions in zero or micro-gravity
- Contains no moving parts

Basic inspection of current EHD gas pump designs confirms that an EHD gas pump would meet all these requirements [5-6, 16]. Now that gas pumps are determined to be a suitable option for an extraterrestrial nuclear reactor the requirements needed to include an EHD gas pump in the experimental CPL need to be determined. However, there is not enough experimental data on EHD gas pumps in regards to flow patterns and heat generation to finalize a list of requirements or a design. It is necessary to perform experimental work, presented in Chapters 5 and 6, to determine what aspects of an EHD gas pump are suitable for an EHD enhanced CPL.



(a)



(b)

Figure 4.13: Picture of an EHD gas pump (a) side view, (b) end view

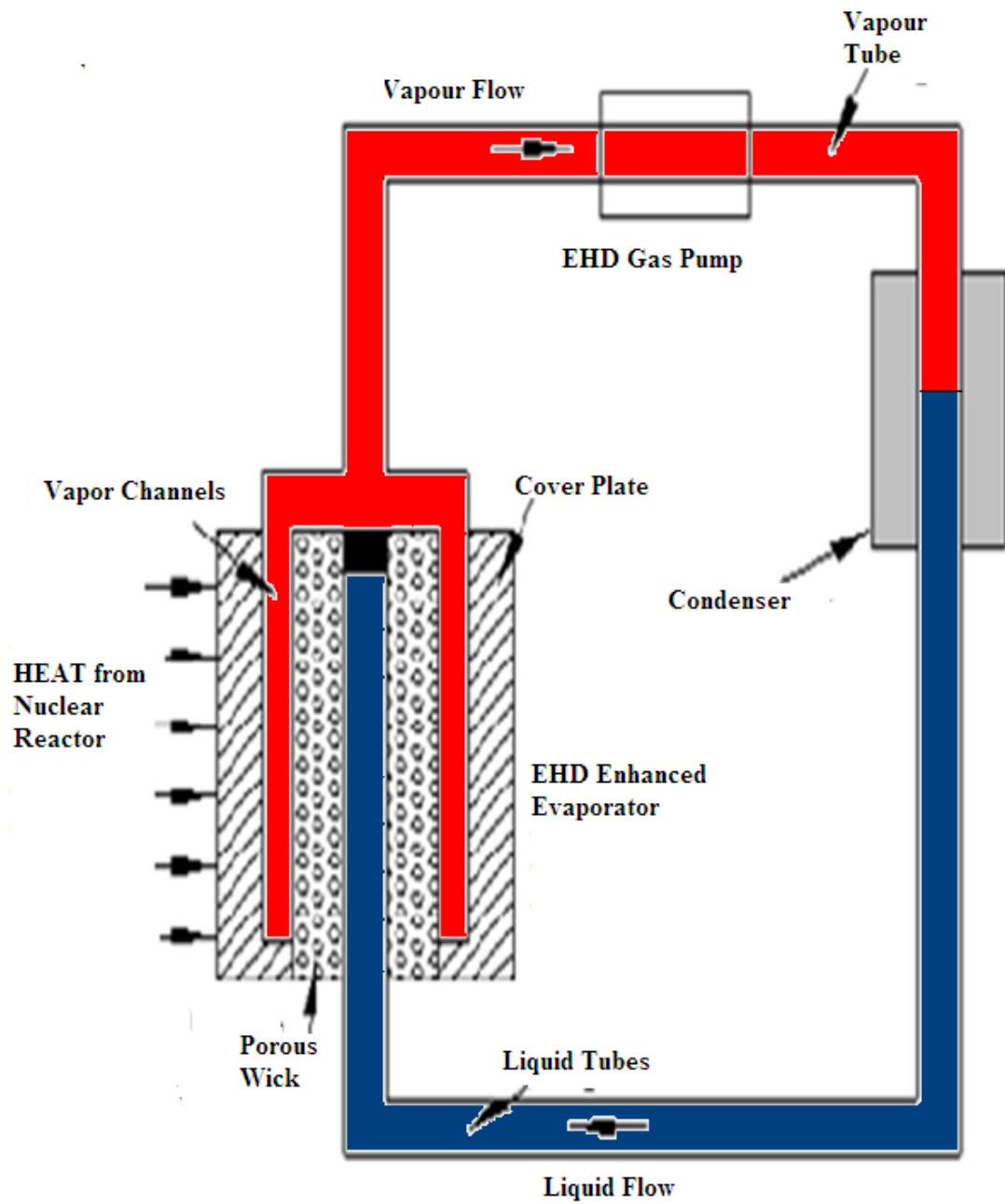


Figure 4.14: CPL for Extraterrestrial Nuclear Reactor with EHD Gas Pump

A detailed description of the experimental apparatus is given in Chapter 5, while the experimental results are described in Chapter 6. From previous research and experiments the effects of polarity, ground plate angle, and ground plate and electrode geometry have been successfully determined. However, there are several factors which need further research that are the target of this investigation.

- Orientation of gas pump with respect to gravity (Horizontal, Vertical, Angled)
- Flow pattern (Free Convection, Force Convection)
- Corona pattern
- Effects of heat generation
- Electrode material
- Effects of Humidity
- Effects of Ambient Temperature
- Effects of Applied Voltage
- Effects of Buoyancy

Each of these factors will be investigated to determine their affect on gas pump performance with conclusions to be made about which factors are important to future gas pump design and inclusion into an experimental CPL. The experiments will be part of a parametric analysis of these factors using air as the working fluid. These experiments will be used to characterize important factors in gas pump design so a final design for the gas pump in a CPL can be achieved in the future. After the parametric analysis is complete the final consideration is the use of R-134a as the working fluid of the CPL. Can R-134a be a suitable medium for an EHD gas pump to operate in? Studies investigating other types of EHD applications have generated EHD flow in R-134a [40]. As long as the material chosen does not cause a breakdown of the R-134a, the evidence suggests that an EHD gas pump would operate in R-134a. Therefore, a significant consideration in the design of the CPL EHD gas pump is to choose materials, geometries, and electric field operating conditions that are suitable to operating in

R-134a. The next step is in future work to then take the experimental results of this project combined with the information gathered on EHD gas pumps and design to build and test an EHD gas pump in a R-134a experimental CPL with an improved evaporator and condenser.

5. EHD Gas Pump Experimental Apparatus

The project involves two distinct experimental apparatus. The primary apparatus is the gas pump experimental apparatus which is described in this chapter. The secondary apparatus is the CPL experimental apparatus which is described in Appendix C. Each chapter will describe the general apparatus used and its components. Variations of the EHD gas pump apparatus specific to a set of experiments will be described in Chapter 6.

The EHD gas pump experiment will use air as the flow medium as stated in Chapter 4. Importantly, with air as the working fluid a more flexible experimental design and apparatus can be used. Also it allows for a more cost effective experiment, accurate instrumentation to be used and for a better comparison on performance as the majority of experimentation involving EHD gas pumps use air as the working fluid. The results can then be adapted to determine the expected effects of using Freon R134a as the working fluid for design purposes. The EHD gas pump experimental apparatus consists of a plate-wire type EHD gas pump, a Faraday cage, a protection resistor and a high-voltage power supply. Both the Faraday cage and the gas pump are grounded via ground wires and a grounding strap. The grounding strap is connected to a grounding stick that allows the operator to ensure that the Faraday cage and gas pump have been discharged before handling. The ground is connected to a wall plug through a surge protector. Grounding is necessary to ensure safety when using high voltage equipment. The purpose of the Faraday cage is to act as an electrical shield between the device and other sources of electromagnetic fields which may influence the device performance. The purpose of the protection resistor is to limit the current in the system to below that of the high voltage power supply and hence protect the power supply from failure.

The high-voltage travels through the protection resistor and is then applied directly to the corona wire electrode. During the experiment the potential

discharges through the ground. After the experiment the power supply is shut off and the equipment is discharge using a grounding stick. The experimental EHD gas pump is a wire-plate convergent angle type gas pump, with a 3° angle for each plate electrode. The experimental EHD gas pump is 120mm length, 50mm width and 35mm height. The inlet is rectangular in shape with dimensions of 35mm width and 30mm height. The dimensions of the outlet are 35mm width and 15mm height and the shape is rectangular. The corona wire has a diameter of 0.22mm. The ground plates are aluminum with dimensions of 75mm in length, 35mm width and 0.08mm thickness. Figure 5.1 displays a schematic of the apparatus.

The EHD gas pump experiment used several different instruments to measure the various parameters. All the measurements were recorded manually and entered into a computer spreadsheet. The Table 5.1 is a list of the components and the equipment used in the experiments, while Figure 5.2 is a photograph of the experimental apparatus. The gas pump experiment measured several parameters. For more detail on the parameters and instrumentation, including their accuracies and uncertainty see Table 5.2.

Importantly the uncertainties listed for the air velocity and temperature measurements are significant. In some cases the differences between measurements are less than the calculated uncertainty. However, the basis of this is a parametric analysis is to discover trends for design purposes and as long as the range of data is significantly greater (a factor of 2) than the uncertainties the trend is considered real and valid. The uncertainty value is determined from the accuracy, bias and disturbance or fluctuation of the instrument. As each data point is relative to each other and is measured with the same instrumentation. The bias and accuracy in each case is the same at each data point in all experiments. Therefore the uncertainty in the measurement relative to each data point is the fluctuation term. So, while there is uncertainty in each measured value that uncertainty is relative to the measured value but not the trend. For example for velocity the uncertainty is 0.1 m/s; which is the measured fluctuation

during experimentation. Figure 5.3 presents an example of this type of error. If the all data points are increasing then velocity is increasing even if the exact increase or value at each point cannot be determined without uncertainty. This technique is sufficient for the level of detail in the analysis required by the design of an EHD gas pump for an extraterrestrial nuclear application. The uncertainty for each measured parameter is listed in Table 5.2. The uncertainty associated with the other measured parameters is not considered to significantly affect the data or the analysis.

Air velocity was measured using a hot-wire anemometer. The anemometer was moved about the outlet at a distance approximately 5mm until a peak velocity was determined. Using the hot-wire anemometer, a temperature would also be recorded at this location. Alternatively in some experiments the outlet was split into a grid system of 12 regions and in each region the peak temperature and air velocity in region was recorded. A diagram of this experimental setup is presented in Figure 5.4. Temperature was also recorded using a T-type thermocouple from a fixed location in the centre of the gas pump exit. The discharge current was measured using the ammeter function on a multimeter. The current was measured in series from the gas pump to the ground.

The applied voltage is recorded from the gauge on the power supply. The discharge voltage is then calculated using the following equation:

$$V_{\text{discharge}} = V_{\text{applied}} - I_{\text{discharge}} * R_{\text{protection}} \quad (5.1)$$

The humidity and ambient temperature is measured using a wireless thermometer placed inside the Faraday cage. The ambient temperature of the cage was also altered for some experiments. First the cage is thermally insulated by covering all open space in the cage with thermal hard board foam insulation. When the cage required heating a heat gun was used to raise the temperature and dry the cage. Once the desired temperature was reached the gun is turned off and removed from the cage. For cooling the Faraday cage is filled with ice

and ice packs to reduce the temperature. The gas pump is raised so that the ice and packs are not touching any part of the gas pump experimental apparatus besides the Faraday cage. The ice is left in the cage during the experiment and removed afterwards. The experiments were also recorded on video to observe corona formation pattern using a camera and recording equipment. The camera was a low light camera mounted about 50-75 cm from the outlet of the gas pump to record the corona. The video was then converted to a digital file using a video digital converter and then edited using software. Finally it was recorded onto DVD using a DVD player/recorder. Table 5.3 lists the camera specifications and its related equipment. The camera used has low light level capability to be able to visualize the light interactions associated with corona glow. Lastly Table 5.4 presents a test matrix identifying each experiment, the parameters that were measured and the purpose of each experiment. The test matrix provides the general purpose of each experiment, the parameters measured and the order of the experiments, while the experimental details of each experiment is presented in Chapter 6. The text matrix also clearly shows the development of the experiments and their increasing complexity.

Table 5.1: EHD Gas Pump Experiment Components

| Component | Manufacturer | Make | Additional Information |
|------------------------------|---------------------|---------------|------------------------|
| EHD wire-plate type gas pump | McMaster University | None | Wire electrode |
| 40kV Power Supply | Glassman | EW 40R15.0-11 | |
| 10kV Power Supply | Glassman | EL 10R04.0 | |
| Faraday Cage | Dr. Ikeda | None | |
| 3.5 MΩ resistor | | | |
| Grounding Stick | UOIT | None | |
| Grounding Strap | UOIT | None | |
| Surge Protector | UOIT | | |

Table 5.2: EHD gas pump Instrumentation

| Parameter | Instrumentation | Accuracy | Uncertainty |
|--------------------------|--|------------|-------------|
| Inlet/Outlet Temperature | -T-type thermocouple with Fluke 116 multimeter | +/- 0.1°C | +/- 2.5°C |
| | -Extech 40119a hot-wire anemometer | +/- 0.1°C | +/- 2.5°C |
| Flow Velocity | Extech 40119a hot-wire anemometer | +/-0.04m/s | +/-0.1m/s |
| Current | Fluke 287 Multi-meter Ammeter function | +/-7.5μA | +/-100μA |
| Humidity | La Crosse WS9124U Wireless Thermometer | +/-0.1%RH | +/-1%RH |
| Ambient Temperature | La Crosse WS9124U Wireless Thermometer | +/-0.025°C | +/-0.1°C |
| Applied Voltage | Glassman power supply | +/-10V | +/-100V |

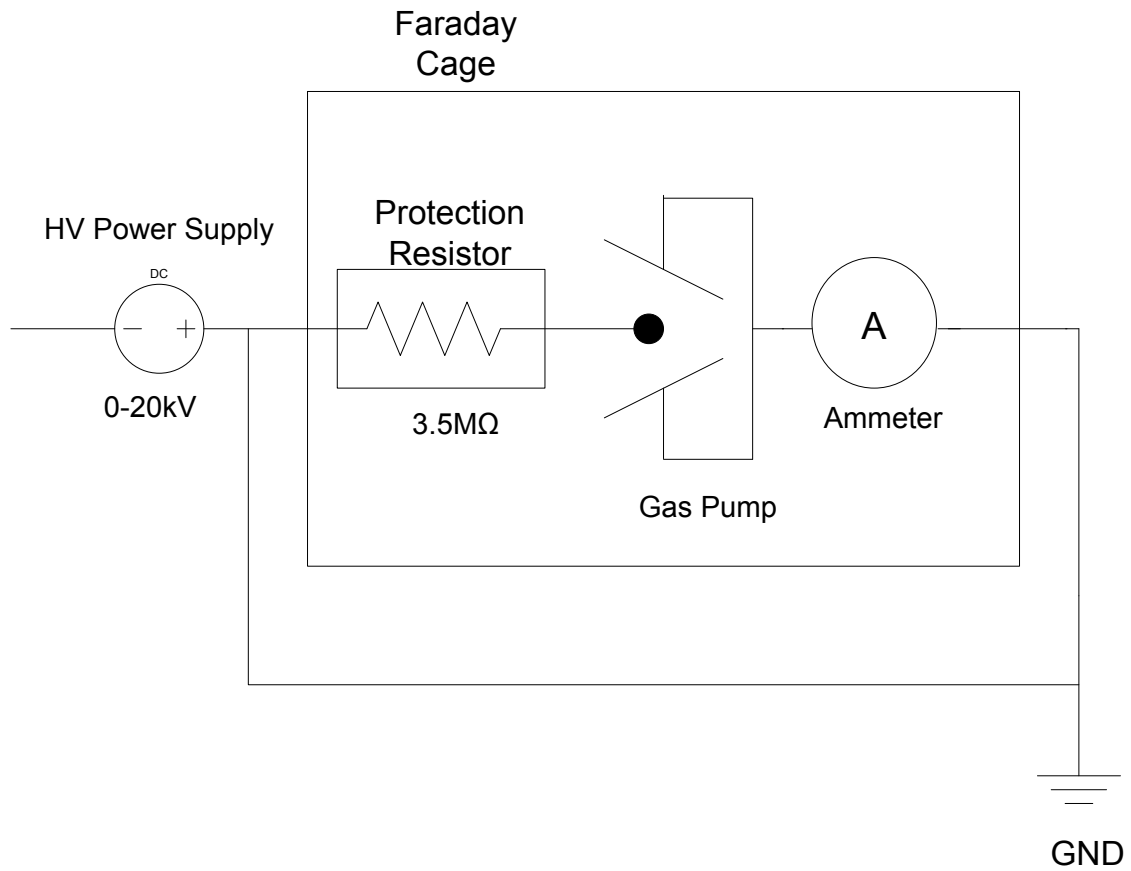


Figure 5.1: Schematic of EHD Gas Pump Experimental Apparatus



Figure 5.2: Photograph of EHD gas pump Experimental Apparatus inside Faraday Cage enclosure

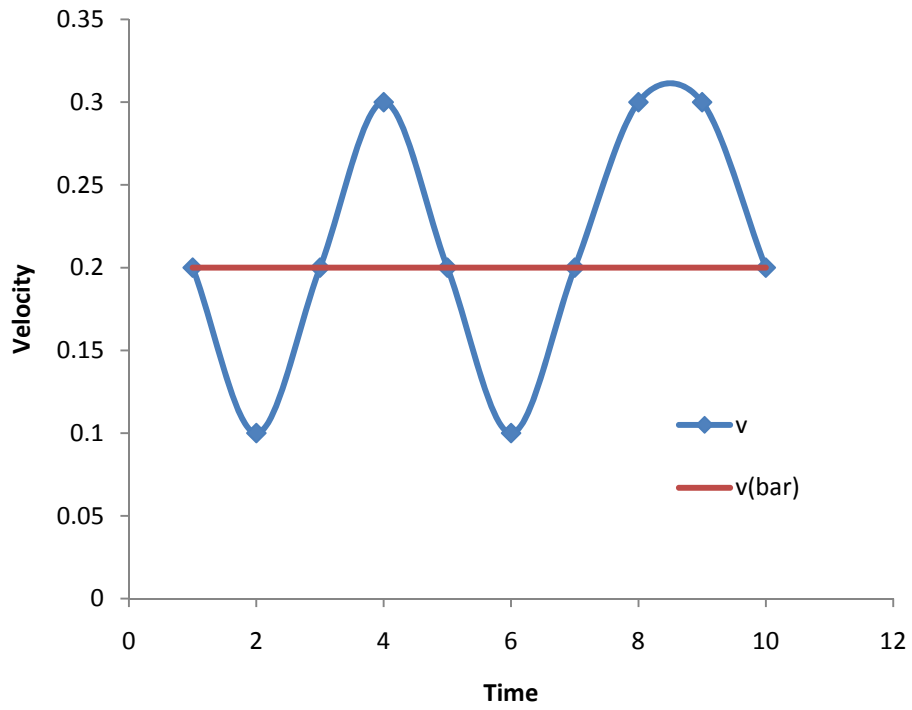


Figure 5.3: Example of Fluctuation Error for Velocity Measurement

Table 5.3: Camera Equipment

| Instrumentation | Specifications |
|--|--|
| Cohu Camera 4912-2000/0000 | <p>Format: 1/2" interline transfer CCD, NTSC or RS-170</p> <p>Active Picture Elements: RS-170A: 768 (H) x 494 (V) CCIR: 752 (H) x 582 (V)</p> <p>Resolution: RS-170A: 580 horizontal TVL, 350 vertical TVL CCIR: 560 horizontal TVL, 450 vertical TVL</p> <p>Sensitivity (faceplate): 0.65 lux at full video, AGC off; 0.02 lux at 80% video, AGC on</p> |
| Toshiba D-VR5 DVD player and recorder | |
| BK Precision 1670A Power Supply | 0-30Vdc 0-3A |
| Honestech My Vid Box video recorder | |
| VHS to DVD 4.0 Deluxe Video Recording Software | |

Table 5.4: Test Matrix

| Experiment # | Purpose | Outlet Temperature | Peak Spot Velocity | Discharge Current | Other Measurements | Video Recorded |
|--------------|---|--------------------|--------------------|-------------------|--------------------------------------|----------------|
| 1 | Characterization of Gas Pump | Yes | Yes | No | Applied Voltage, Ambient Temperature | No |
| 2 | Characterization of Gas Pump | Yes | Yes | No | Applied Voltage, Ambient Temperature | No |
| 3 | Characterization of Gas Pump | Yes | Yes | No | Applied Voltage, Ambient Temperature | No |
| 4 | Characterization of Gas Pump | Yes | Yes | No | Applied Voltage, Ambient Temperature | No |
| 5 | Study Orientation Effect, Humidity Effect and Current-voltage Characteristics | Yes | Yes | Yes | Applied Voltage, Ambient Temperature | No |
| 6 | Study Orientation Effect, Humidity Effect and Current-voltage Characteristics | Yes | Yes | Yes | Applied Voltage, Ambient Temperature | No |
| 7 | Study Orientation Effect, Humidity Effect and Current-voltage Characteristics | Yes | Yes | Yes | Applied Voltage, Ambient Temperature | No |
| 8 | Study Orientation Effect, Humidity Effect and Current-voltage Characteristics | Yes | Yes | Yes | Applied Voltage, Ambient Temperature | Yes |
| 9 | Study Orientation Effect, Humidity Effect and Current-voltage Characteristics | Yes | Yes | Yes | Applied Voltage, Ambient Temperature | Yes |
| 10 | Study Gas Pump at High Temperature | Yes | Yes | Yes | Applied Voltage, Ambient Temperature | No |
| 11 | Study Gas Pump at Low Temperature | Yes | Yes | Yes | Applied Voltage, Ambient Temperature | No |
| 12 | Determine Free Convection Profiles | Yes | Yes | Yes | Applied Voltage, Ambient Temperature | Yes |

| Experiment # | Purpose | Outlet Temperature | Peak Spot Velocity | Discharge Current | Other Measurements | Video Recorded |
|--------------|--------------------------------------|--------------------|--------------------|-------------------|--------------------------------------|----------------|
| 13 | Determine Free Convection Profiles | Yes | Yes | Yes | Applied Voltage, Ambient Temperature | Yes |
| 14 | Determine Forced Convection Profiles | Yes | Yes | Yes | Applied Voltage, Ambient Temperature | No |

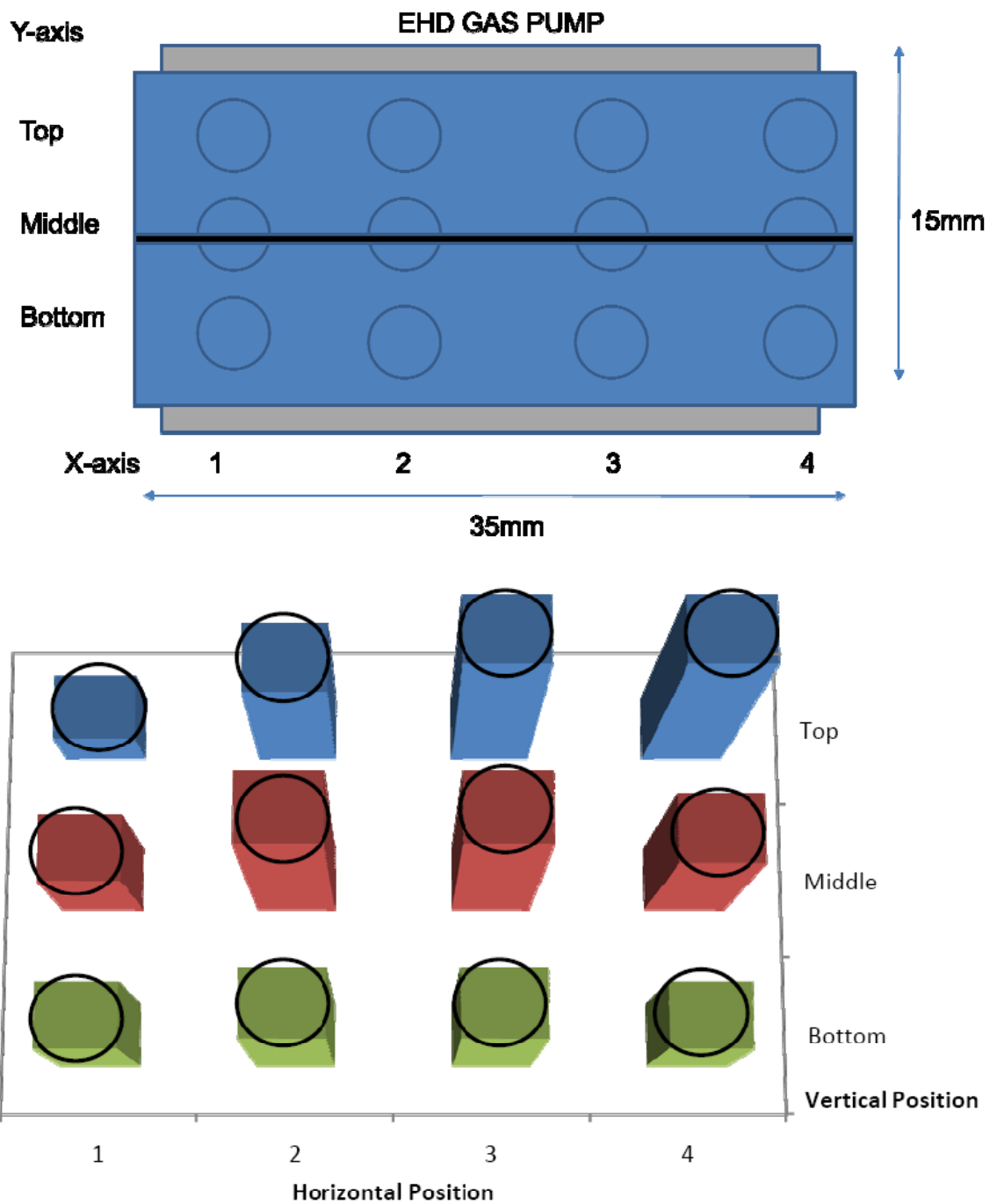


Figure 5.4: Top) Measurement Grid for Flow Profile Experiments overlaid on EHD gas pump outlet schematic Bottom) Measurement Grid overlaid onto flow profile figure

6. EHD Gas Pump Experimental Study

The genesis of this research began with the analysis of previous research [16, 19, 20] to determine the heat generation effects of that specific gas pump design as discussed in Chapter 2. The review showed that some effects such as humidity, temperature and orientation have not been adequately studied. Hence a design for the Freon loop cannot be optimized without addressing these gaps in the research. A schematic of the design is displayed in Figure 6.1. A generation I gas pump from McMaster University was acquired and the experimental apparatus discussed in Chapter 5 was designed to perform in-house experiments to further the analysis and to begin new research geared towards gas pump design of capillary pumped loops for extraterrestrial nuclear applications.

The EHD Gas Pump experimental study is a series of experiments performed using the convergent plate rectangular gas pump and the experimental apparatus described in Chapter 5. The experiments were designed to measure the temperature gradient across the pump, ambient temperature and humidity, air velocity, applied voltage, time-averaged current and time-averaged power. This chapter describes experimental results and explains the phenomena occurring during the experiment. A discussion on the applicability of the EHD gas pump for improving the efficiency of the CPL is also performed.

6.1 Experimental Details

The experiments use the apparatus and instrumentation described in Chapter 5. Table 6.1 displays the various experiments and their general setup and instrumentation. Also there are several symbols used in the legends of the figures to represent certain features of the data. Table 6.2 lists these symbols and what parameters they represent.

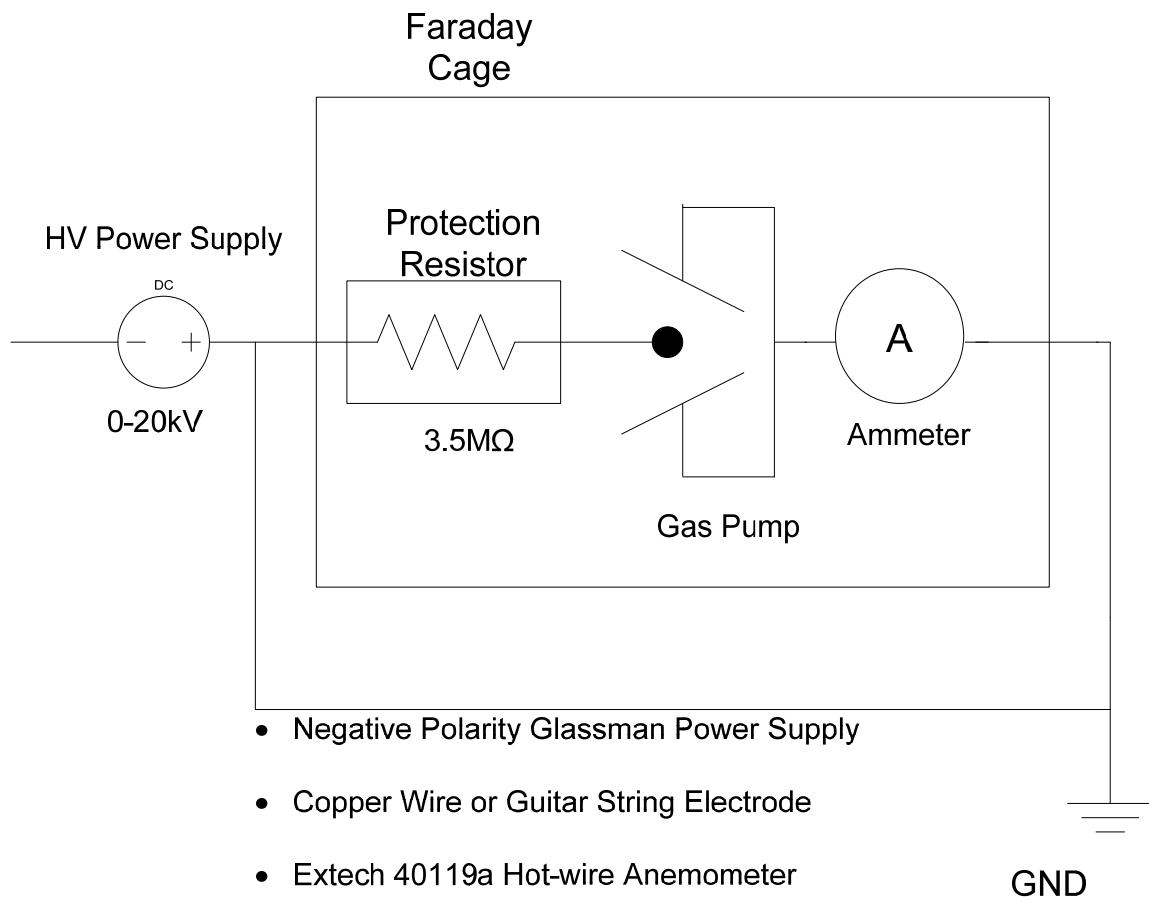


Figure 6.1: EHD Gas Pump Experimental Setup

Table 6.1: EHD Gas Pump Experimental Data Sets

| Experiment | Electrode Type | Orientation | Faraday Cage | Power Supply | Instruments Used | Insulated |
|--------------------------------|----------------|-------------------------|--------------|--------------|-----------------------------|-----------|
| Temperature Generation | Steel String | Horizontal and Vertical | Yes | 10kV | No ammeter No anemometer | None |
| Flow Velocity | Steel String | Horizontal and Vertical | Yes | 10kV | No ammeter | None |
| Humidity Test | Steel String | Horizontal and Vertical | Yes | 10kV | All Instruments | None |
| IV Characteristic Test | Steel String | Horizontal | Yes | 40kV | No Anemometer | None |
| Humidity Test 2 | Copper Wire | Horizontal | Yes | 40kV | All Instruments | None |
| Humidity Test 3 | Copper Wire | Vertical | Yes | 40kV | All Instruments | None |
| High Temperature-Low Humidity | Copper Wire | Horizontal | Yes | 40kV | All Instruments | Yes |
| Room Temperature-High Humidity | Copper Wire | Horizontal | Yes | 40kV | All Instruments | Yes |
| Cold Temperature | Copper Wire | Horizontal | Yes | 40kV | All Instruments | Yes |

Table 6.2: Legend Symbols

| Symbol | Full Name |
|------------|--|
| TC | T-type Thermocouple |
| A | Anemometer |
| V | Vertical Orientation |
| H | Horizontal Orientation |
| Legend Key | Date-Orientation-Relative Humidity-Ambient Temperature |

6.2 Gas Pump Heat Generation Analysis

Before experimentation began, previous experimental results from Tsubone et al [16, 19, 20] were analyzed to determine if the heat generation in the gas pump is first significant and second caused from the introduction of EHD phenomena into the system. The work used Tsubone's gas pump to examine flow profiles and mass flow rate, but the effects of heat generation and heat transfer were not analyzed. From Figures 6.2 and 6.3 it can be determined that there are heating generation effects present during the operation of an EHD gas pump and that these effects are related to the onset of corona and the introduction of EHD forces. Figure 6.2 displays the mass flow rate and the heat balance power, while Figure 6.3 compares the flow exit temperature to the heat balance power. The primary observation is that as the applied pump power increases the temperature and mass flow rate rise. However, the mass flow rate and heat balance power will reach a maximum level and then decrease while power increases further due to increasing discharge current. The temperature will continue to rise with the discharge power. From this analysis it is determined that the exact cause and effects of these heat generation effects is unclear and further investigation in this area is required to determine exactly how this temperature increase will affect EHD gas pump performance and how that relates to CPLs. The velocity, flow patterns, outlet temperature and temperature distribution all need to be investigated to evaluate how they affect gas pump performance.

The Rayleigh number is also calculated as part of the analysis. The Rayleigh number is defined as the product of the Prandtl and Grashof numbers, but physically is the ratio of buoyancy forces to the viscous forces. The Rayleigh number is determined using the following equation.

$$Ra = \frac{g\beta|T_w - T_g|L^3}{\nu_g\alpha} \quad (6.1)$$

Where, g is the acceleration due to gravity, β is the coefficient of thermal expansion, T_w is the temperature of the corona wire, T_g is the temperature of gas,

L is the characteristic length, ν_g is the kinematic viscosity and α is the thermal diffusivity.

In this case β is approximately $3.3 \times 10^{-3} \text{ K}^{-1}$, ν_g is $1.66 \times 10^{-5} \text{ m}^2/\text{s}$, and α is $2.28 \times 10^{-5} \text{ m}^2/\text{s}$. The characteristic length from the electrode to ground is 17.5mm. Figure 6.4 shows the calculated Rayleigh number relative to the temperature gradient induced via Joule heating. Note that the Rayleigh number is not significant for applications in air until it reaches values greater than 10^5 . The analysis of the Rayleigh number showed that while the Rayleigh number is having no dominant effect on the flow, buoyancy forces are present. This result is important as it suggests that buoyancy and joule heating alone are not responsible for the behaviour of the mass flow rate and that the EHD forces are contributing to the mass flow and temperature increase. However, in smaller gas pumps, where the characteristic length is reduced, there is an expected significant decrease in value in the Rayleigh number and buoyancy forces. In Tsubone's gas pump for example, which is a narrow capillary type EHD gas pump, the Rayleigh number is calculated to be in the 10^1 magnitude range with a characteristic length of 0.175mm. The EHD gas pump for the experimental CPL will be in a section of piping 6.4mm in diameter with a characteristic length significantly smaller than the experimental EHD gas pump, so it is important to note this scaling effect.

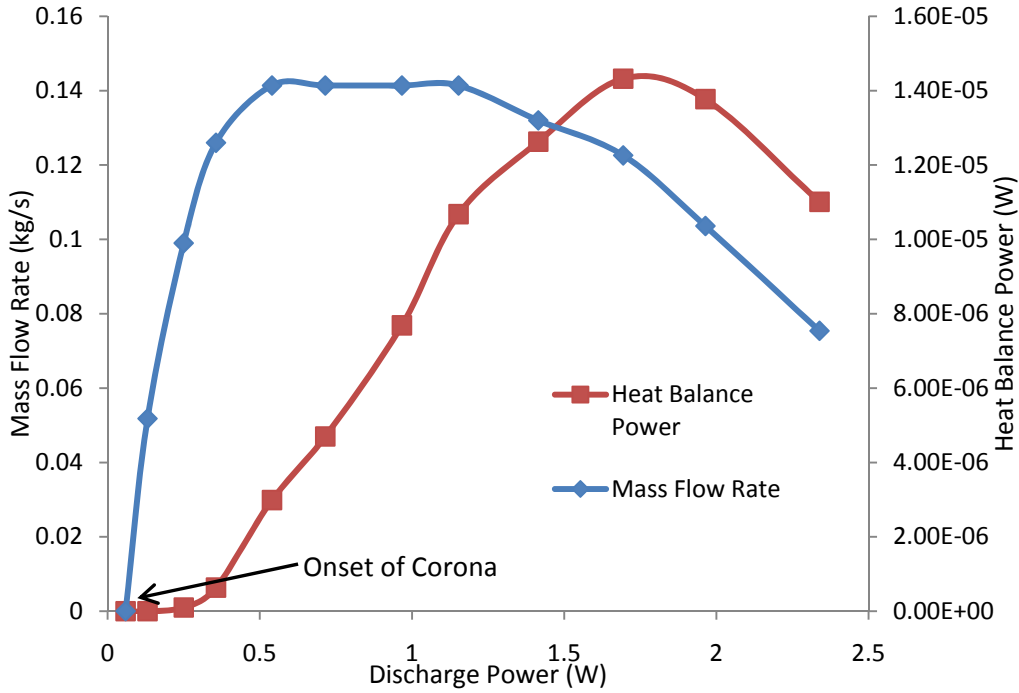


Figure 6.2: Mass Flow and Heat Balance Power vs. Discharge Power for Tsubone's EHD gas pump

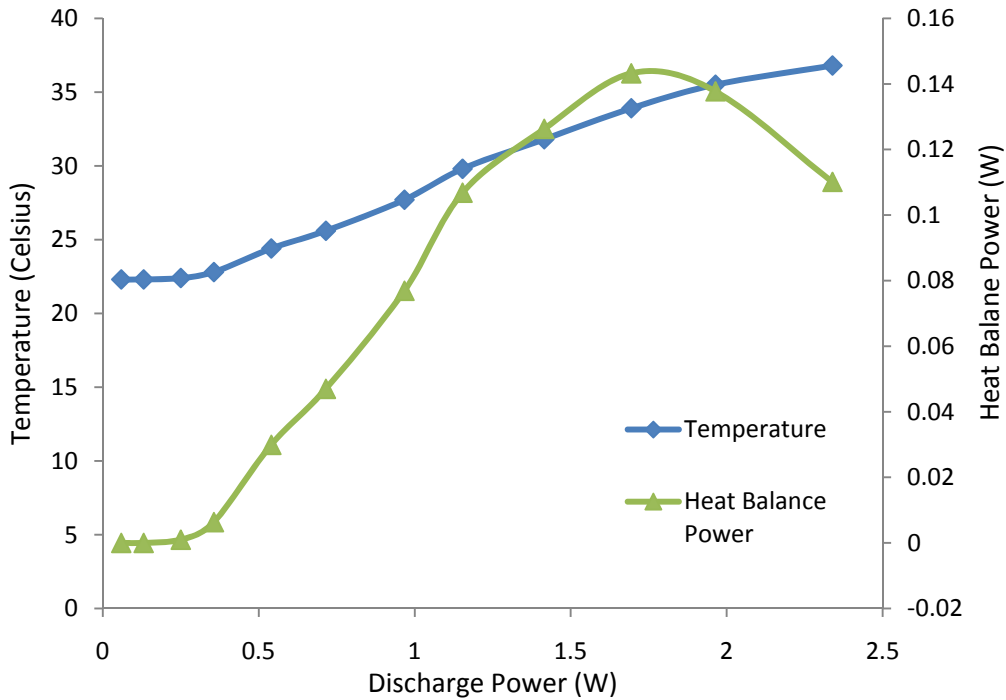


Figure 6.3: Comparison of Outlet Temperature and Heat Balance Power for Tsubone's EHD gas pump

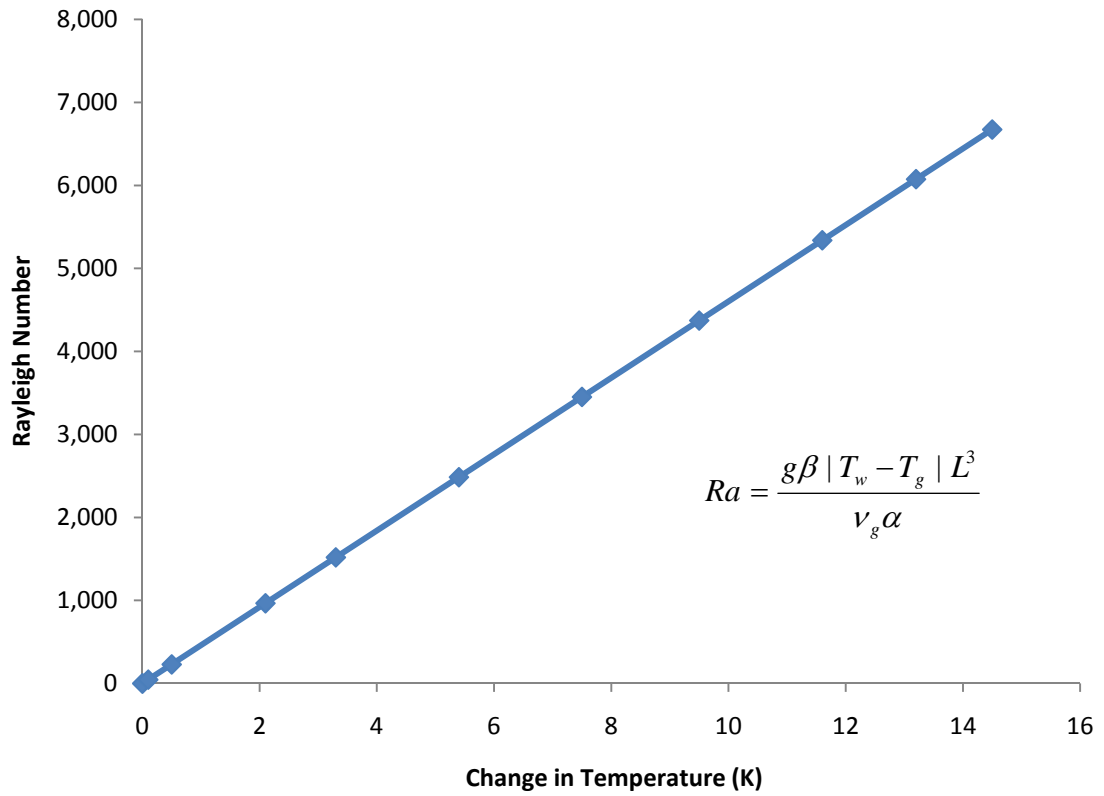


Figure 6.4: Rayleigh Number vs. Temperature for Experimental EHD gas pump

6.3 EHD Gas Pump Characterization

Figure 6.5 is a series of photographs of the gas pump at corona onset, a low voltage setting, a high voltage setting, and spark discharge. At onset there is little corona or glow, because the corona is yet to fully form, but EHD effects are measurable. At lower voltages the corona is brighter, but still not fully formed when compared to a fully formed along the entire length of the wire corona at a higher voltage; the difference in appearance is noticeable. Lastly, at spark discharge the current will reach a level where the corona will become unstable and the device will begin to spark and the corona will break down with the gas pump is left on. Physically, at this current-voltage level the gas pump electric field has moved into a range called the spark region as to before where it was in a glow corona region. The gas pump can only operate in a glow corona region without damage to power supply.

The current-voltage characteristics of the gas pump are important to characterize the electric field and EHD effects occurring at each voltage level. Figure 6.6 displays the current and voltage characteristics of the EHD gas pump. The corona onset for the pump with a steel string electrode (guitar wire) in this set of experiments occurred at 6kV and spark discharge occurred at 15kV. However, the experiment was only performed to voltages of 10kV. The time-averaged-current peaked at a spark discharge value of 620 μ A.

The first set of experiments compared the effects of orientation on peak velocity and outlet temperature in the low voltage region (6kV-10kV). The data is relatively consistent showing a gradual increase from the onset of corona to about 9kV. From here the temperature increase is slightly steeper until 10kV when this set of experiments was stopped due to limitations of the available power supply. The temperature gradient ranged from 1.5- 2.5 K except for Run 3 and Run 7 when the experiment was performed in a much cooler room.

Figures 6.7-6.9 display the temperature and velocity results for this data set. The horizontal orientation dataset is presented in Figure 6.7. Figure 6.8 displays the results for the change in outlet temperature in the vertical orientation. In Figure 6.7 the temperature gradient fluctuates, even decreasing from the onset of corona until approximately 8-9kV. From here the temperature gradient steadily increases. The fluctuations are present in the horizontal orientation but not in the vertical orientation, which suggest the vertical orientation may help to stabilize the flow to the buoyancy forces under low applied voltages. Figure 6.5 visually displays the difference between low applied voltages (<10kV) and high applied voltages (>10kV). The point between 8-9kV is where the temperature gradient increases and is believed to occur when the EHD flow is stabilized due to a stable corona along the entire length of the wire. Run 3 takes longer to heat and has a lower temperature gradient compared to the other experimental runs, suggesting the possibility the cold room required a greater energy input. Another possibility is there may have not been enough time between the horizontal and vertical experiment as the gas pump chamber still may not have stabilized at room temperature, although the experiments were performed at least an hour apart to prevent that exact situation. So, the heat gain from the vertical experiment and subsequent heat loss may have been due to competing effects. At 9kV it appears that the EHD flow stabilizes and overcomes the initial higher temperature effects. From here it is clear that at lower applied voltages buoyancy seems to affect the flow in the vertical orientation. While this result suggest a benefit in the gas pump performance being placed in the vertical direction, for extraterrestrial applications gravity will not be present therefore study in the horizontal direction may better reflect gas pump performance in micro-gravity environment.

The peak spot velocity ranged from 0.2-0.7 m/s with the vertical orientation having a higher peak velocity than the horizontal orientation, further suggesting that at the lower voltages the vertical orientation has a stabilizing effect on the flow. To clarify, the peak spot velocity is measured by moving the anemometer sensor across the outlet until a maximum velocity is measured. A temperature

measurement is then taken at the same location. Again runs 3 and 7 have a different pattern than the experiments performed on the other days likely due to different ambient temperatures.

While, this dataset highlighted the flow effects and instabilities at lower voltages (up to 9kV) no observations could be made at higher voltages (>9kV) where the flow from the initial results appears more stable. So it was concluded that for the remaining experiments a larger power supply capable of reaching spark discharge would be used. Secondly, as the steel string electrode had been used previously and was damaged a copper electrode was installed to replace the steel string electrode for the remaining experiments.

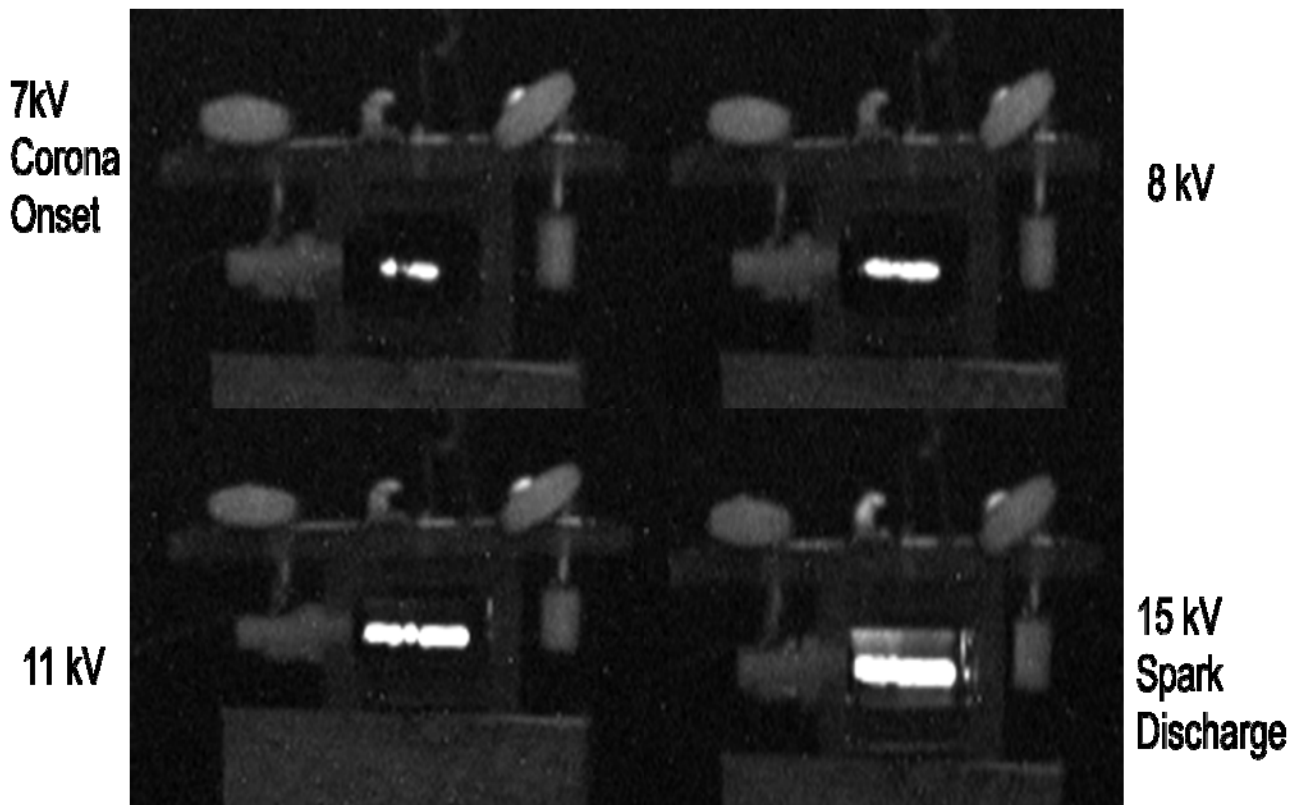


Figure 6.5: Pictures of Corona Formation

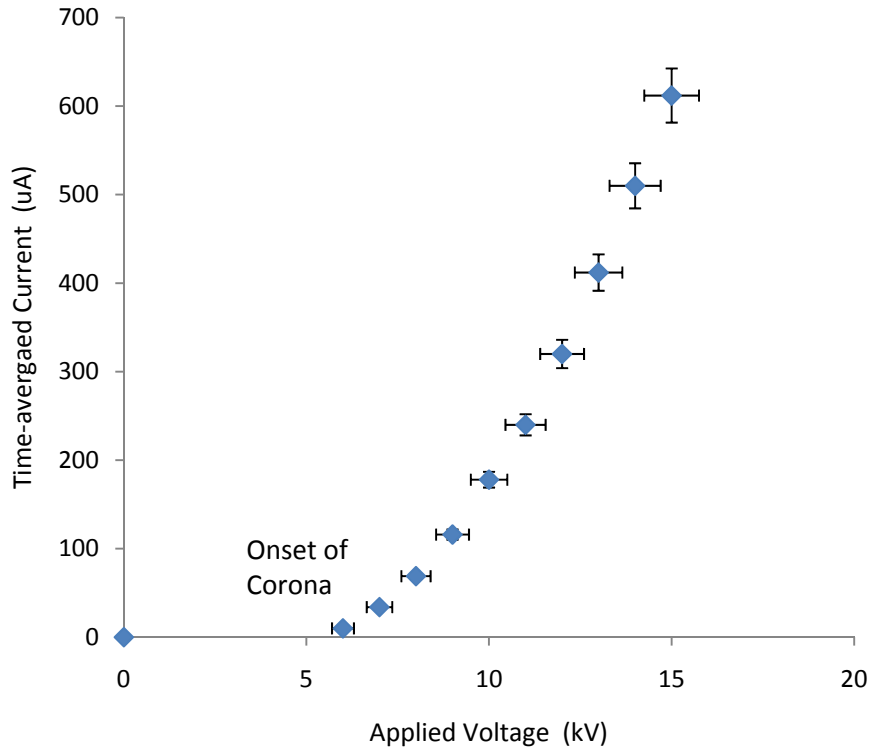


Figure 6.6: VI Characteristics for Gen I EHD Gas Pump with Steel String Electrode

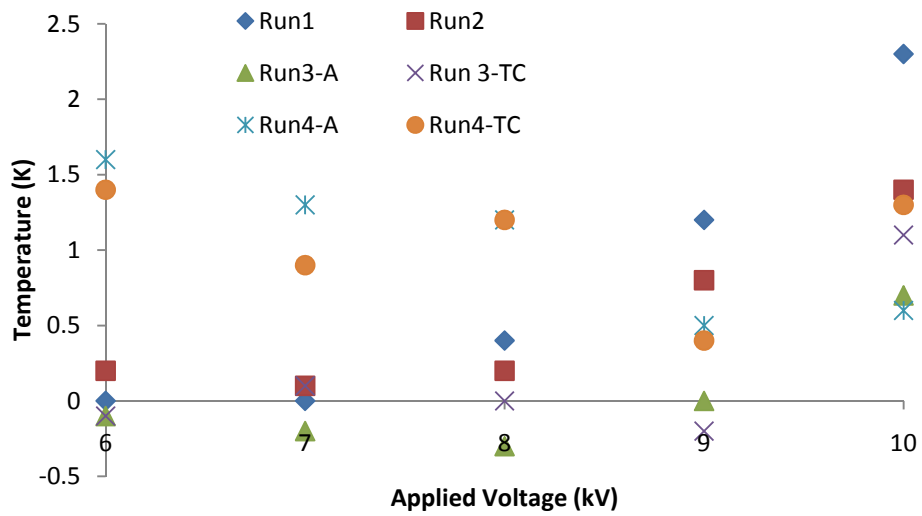


Figure 6.7: Outlet Temperature Change vs. Applied Voltage for Gen I EHD Gas Pump with Steel String Electrode in Horizontal Orientation

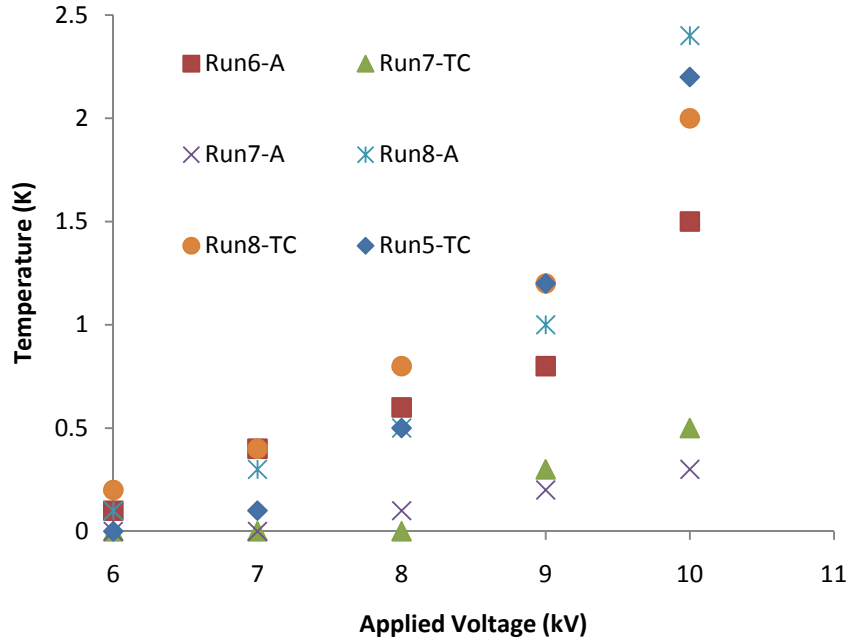


Figure 6.8: Outlet Temperature Change vs. Applied Voltage for Gen I EHD Gas Pump with Steel String Electrode in Horizontal Orientation

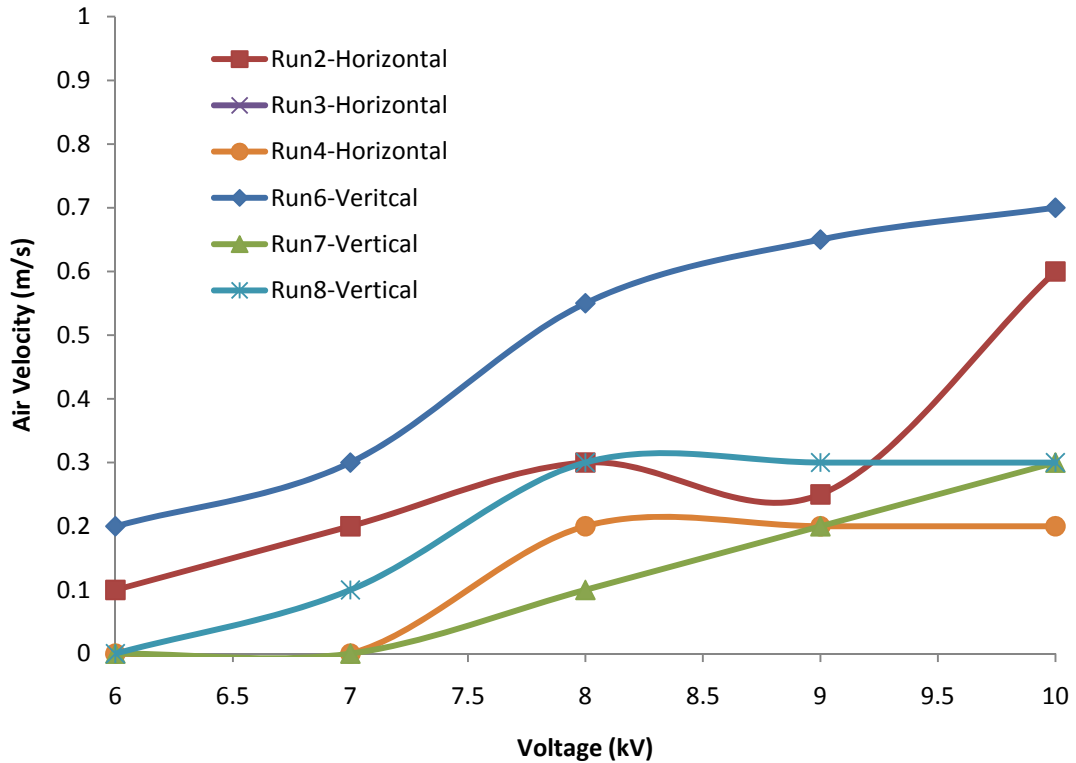


Figure 6.9: Peak Spot Velocity vs. Applied Voltage for Gen I EHD Gas Pump with Steel String Electrode

6.4 Copper Electrode Experiments

With the larger power supply capable of applied voltages up to 40kV, the experiments were performed up to the spark discharge region. An experiment to obtain the current-voltage characteristics from start (0 kV) to spark discharge (15-17kV) was performed for both the steel string and copper electrode with the current-voltage characteristics shown in Figure 6.10.

For both electrode types, corona onset occurs at 6kV suggesting that wire material has no effect on corona onset. The steel string performs slightly better than the copper electrode as it produces a higher power at similar current and voltage settings. However, the steel string electrode was severely stressed and was damaged during earlier experiments, so it must be replaced. Based on these results the copper electrode is a suitable replacement for the remainder of the experiments as the differences between the steel string and copper wire electrode for this particular experiment is negligible. Also the copper electrode initially had a higher spark discharge point, this may be due to the excellent surface condition of the electrode and use of copper wire electrodes may be a factor in gas pump performance where ablation phenomena can deteriorate the surface. Figure 6.11 displays the current-voltage characteristics for the set of experiments involving the copper electrode. The results are consistent with a corona onset of 5-7kV and spark discharge of 15-17kV.

Figure 6.12 presents the peak spot velocity for the copper electrode in the vertical and horizontal orientation. The peak velocity in general rises with voltage to a maximum speed of 0.5-0.8 m/s. The peak velocity also has a pattern of a rise followed by a plateau for up to 13kV followed by a rise until spark discharge is reached. Figures 6.13 and 6.14 present the temperature change at the outlet. The maximum temperature change ranges from 8-12 K. The most noticeable trend is in the instances of Runs 11, 15, and 16 where there was an initial decrease in temperature. In the case of Run 11 the temperature loss is small, less than 1°C while in the other two cases the loss is 1-4°C. In the previous Chapter this loss occurred occasionally in the horizontal orientation and it was

suggested the inner chamber had not been sufficiently cooled between experiments. In these cases there was considerable time between these experimental runs and previous experiments. In Runs 15 and 16, however the experiments were performed at high initial temperatures of 37°C and 50°C. Here the chamber held the heat better in the chamber of the pump than the cage, so heat losses from the pump's chamber between the inlet and outlet to the outside environment were greater than the heat being generated until sufficient heating from the corona occurred and the flow stabilized. For the Run 11 case, similar phenomena could be occurring where the chamber is releasing heat to the environment from both the outlet and the inlet. Another explanation is the initial EHD forces may be drawing in cooler air into the pump and releasing it from the outlet causing what appears to be a temperature loss but is actually just heating cooler air than was measured. Thus the EHD forces are causing a re-circulating of the hotter air that was present in the chamber until the flow is stabilized and the forces then push the hotter air to the outlet. Still, when comparing these results to the previous results they confirm the trends and patterns. The main difference is the instabilities in the flow observed at the lower voltages are not present at the higher voltages nor is there a pronounced difference between horizontal and vertical orientation at higher voltages. This dataset concluded the initial investigation stage of the project. From here, the experiments are organized based upon the phenomena being studied.

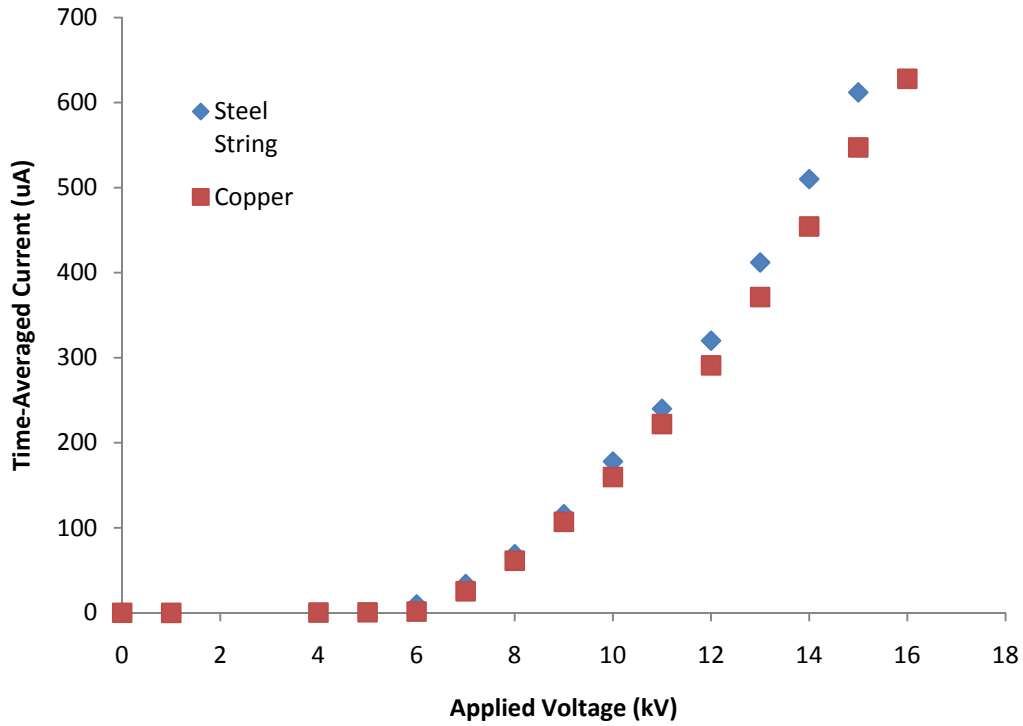


Figure 6.10: Comparison of Copper and Steel String Electrode Time Averaged Power vs. Applied Voltage

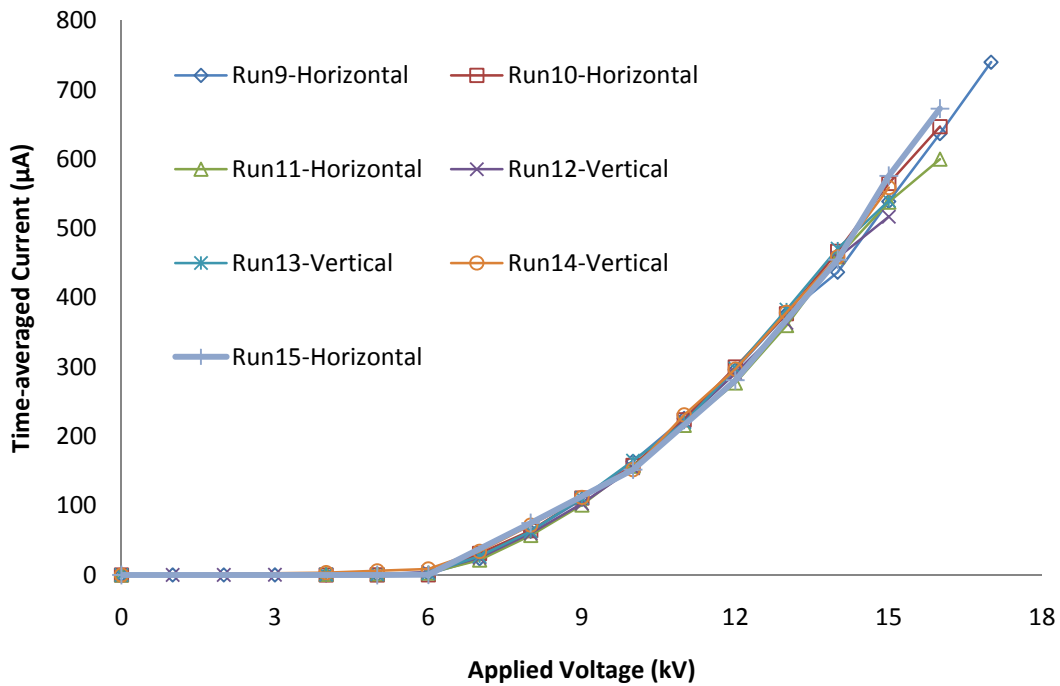


Figure 6.11: Time-averaged-current vs. Applied Voltage for a Copper Electrode at Humidity Range of 50-68% and Ambient Temperature of 23-50°C

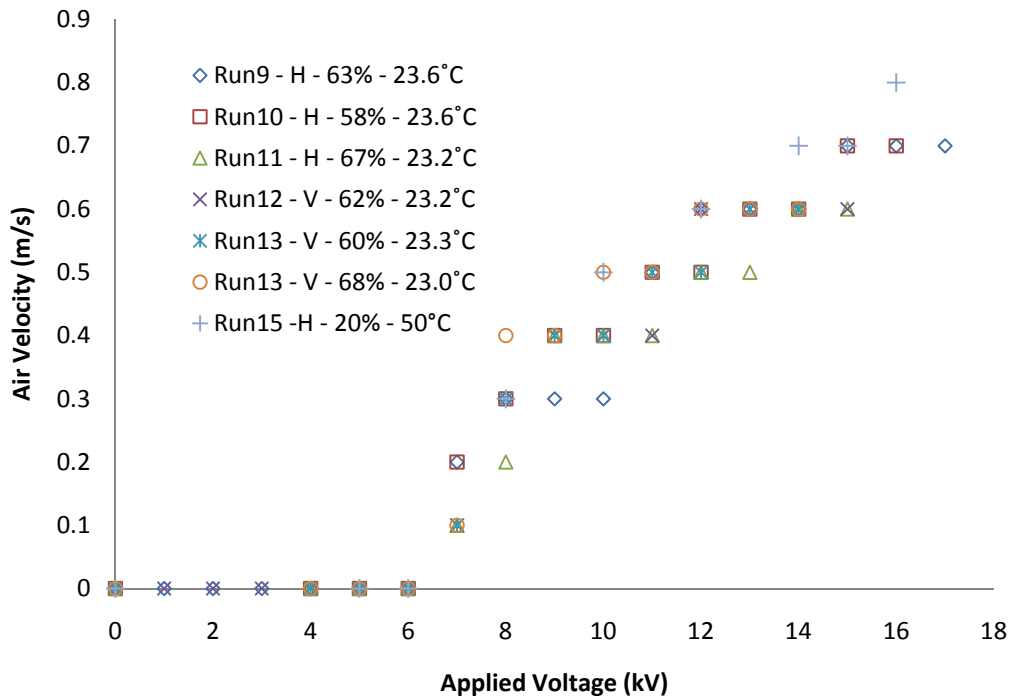


Figure 6.12: Peak Spot Velocity vs. Applied Voltage for a Copper Electrode

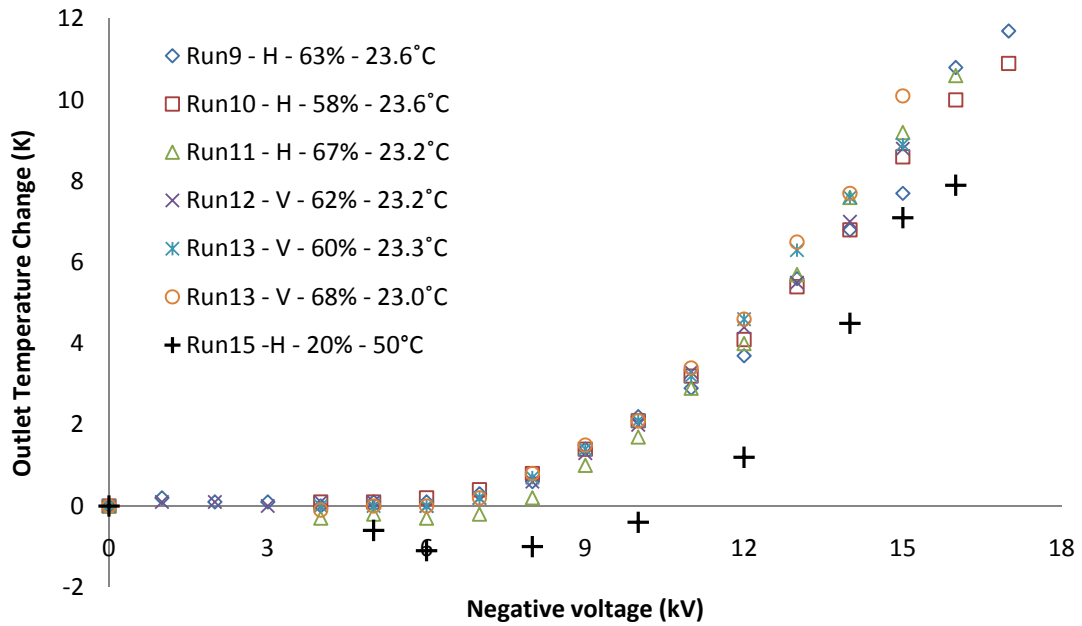


Figure 6.13: Outlet Temperature Change vs. Applied Voltage for a Copper Electrode measured by T-type Thermocouple

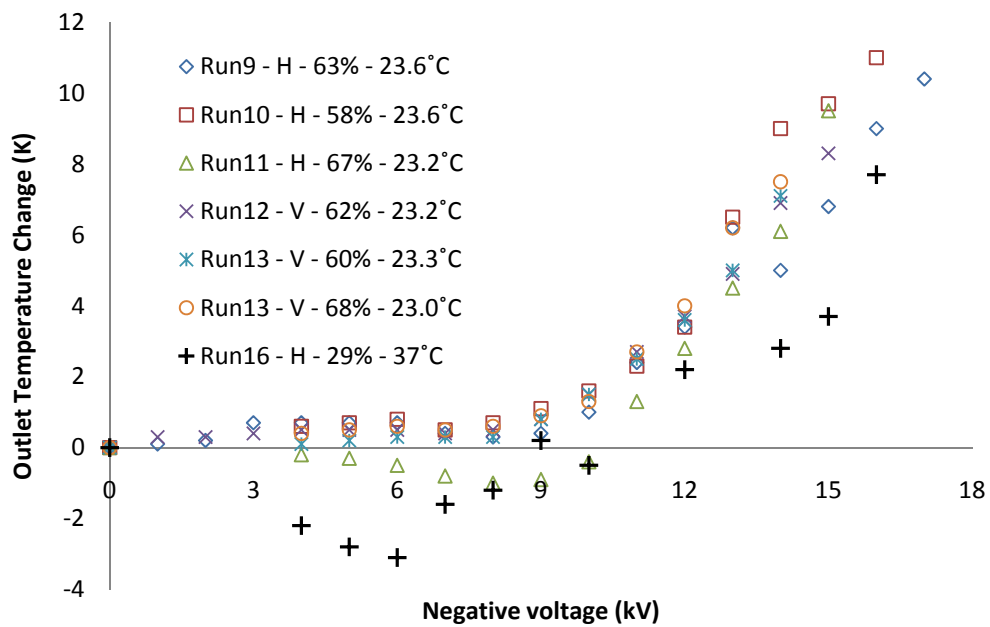


Figure 6.14: Outlet Temperature Change vs. Applied Voltage for a Copper Electrode measured by Hot-wire Anemometer

6.5 EHD Gas Pump Orientation Effect

The orientation of the gas pump, i.e. horizontal or vertical, can have a significant impact on the flow, especially at lower voltages. Figures 6.15 and 6.16 present the current-voltage characteristics for the gas pump in the horizontal and vertical directions respectively. The figures are relatively similar except that the horizontal curves are slightly flatter initially and then slightly steeper towards the spark discharge region. However, both vertical and horizontal oriented pumps achieve similar maximum values for power.

Figure 6.17 compares the peak spot velocity of a typical horizontal dataset to the vertical dataset at 23°C and 67% relative humidity. The figure clearly shows the trend demonstrated by the results of the initial investigation. In vertical orientation the velocity peaks at lower voltages but the horizontal orientation will achieve a similar maximum spot velocity. This result further suggests buoyancy forces are enhancing the flow rate initially at low coronas, but eventually the EHD forces become strong enough that a maximum velocity is reached regardless of orientation.

Figure 6.18 displays a comparison of the change in outlet temperature in both orientations. In the vertical orientation the rise in temperature is steady and consistent, while the temperature change in the horizontal orientation consistently has a decrease and then a sharp rise at higher voltages. The results show that the vertical orientation has a higher outlet temperature gradient at lower voltages due to the buoyancy effect and the horizontal orientation has a higher temperature gradient at higher voltages and a higher maximum outlet temperature. Here, the buoyancy forces are providing the gas with an initial momentum, which is why it enhances flow in the vertical direction. This enhancement occurs when the EHD and buoyancy forces are in the same direction. This initial push by the buoyancy forces therefore appears to help stabilize the flow and immediately generate a heating effect at the outlet in the vertical orientation. In the horizontal direction these buoyant forces are not as strong and not in the direction of the flow so the heat is remaining near the

electrode. The EHD flow near the electrode may even be drawing the heat from the outlet causing a cooling effect in the horizontal orientation. However, as the voltage increase the EHD forces become strong enough to transport the heat and mass flow to the outlet causing a more drastic rise in temperature at the outlet. Also as the heat is being transported to the outlet and removed from the system at lower voltages there is less heat in the system once pump is at the higher voltages. Then it would be expected that in the vertical orientation the maximum temperature is lower than in the horizontal orientation where the air has remained near the electrode longer allowing it to reach higher temperatures. Based on these results the horizontal orientation is the preferred orientation as the buoyancy effects in the vertical orientation clearly have an effect on the results that would not be present if the EHD gas pump was used in a CPL in a micro-gravity or zero-gravity environment.

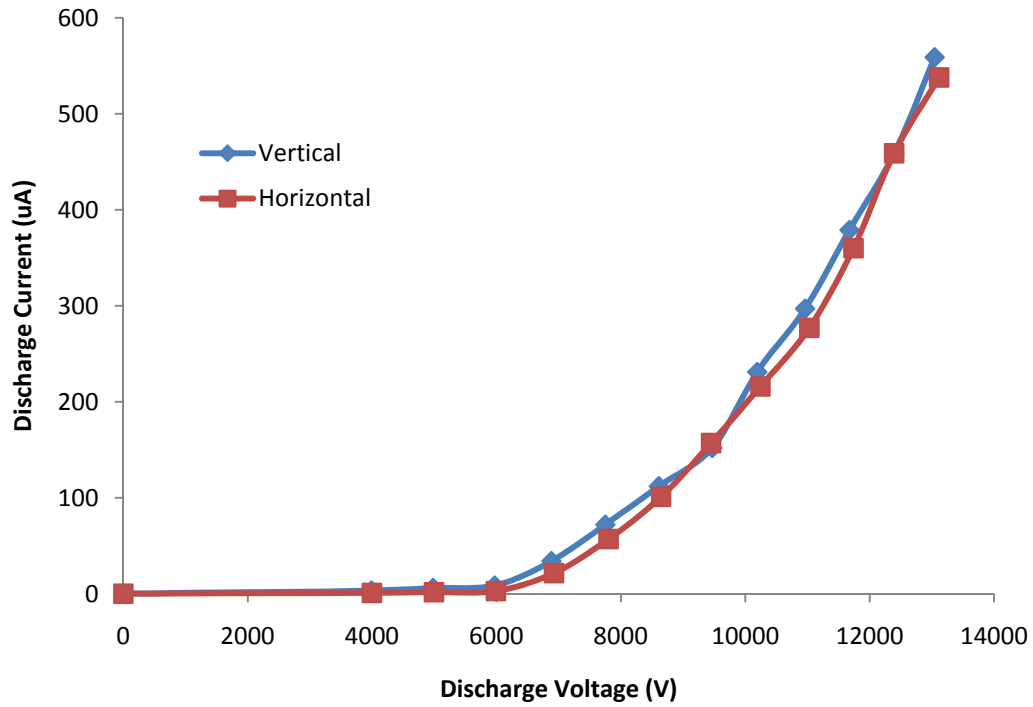


Figure 6.15: Comparison of discharge current of an EHD gas pump in horizontal orientation and vertical orientation at 67% humidity and 23°C

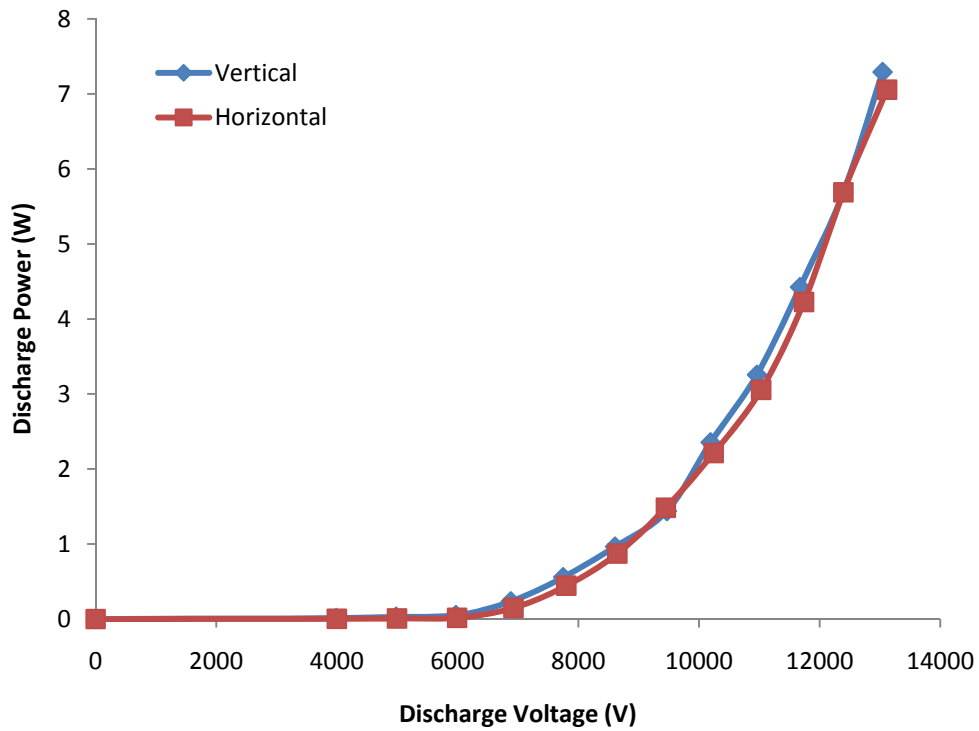


Figure 6.16: Comparison of discharge power of an EHD gas pump in horizontal orientation and vertical orientation at 67% humidity and 23°C

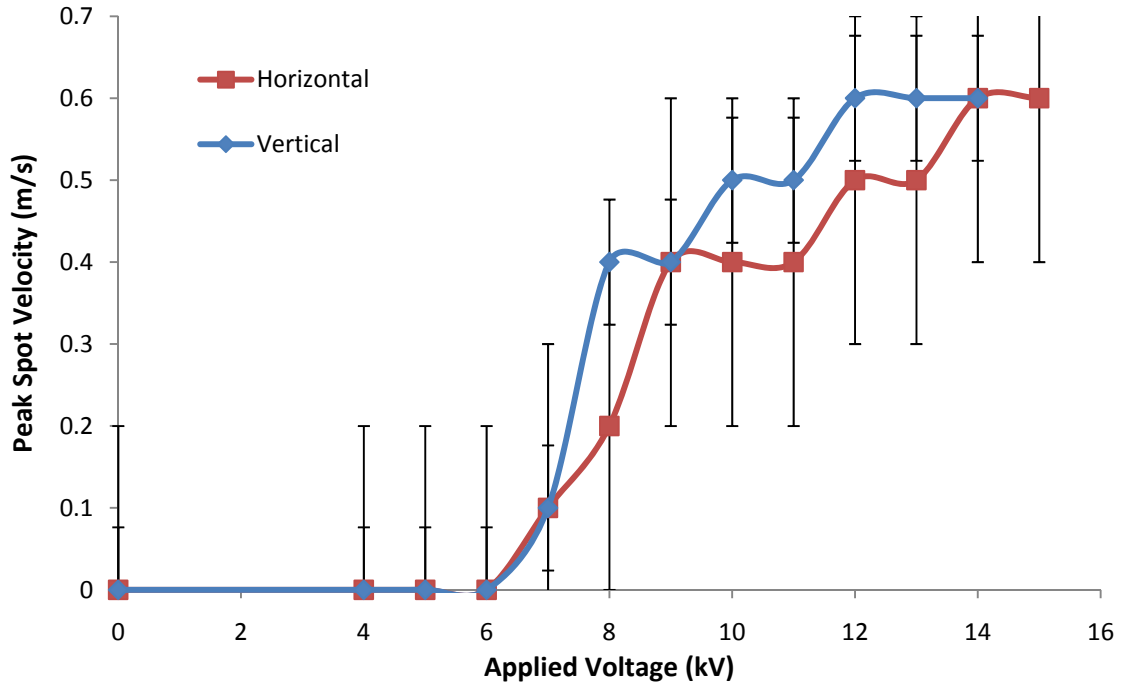


Figure 6.17: Comparison of Peak Spot Velocity of EHD gas pump in Horizontal and Vertical Orientation at 67% humidity and 23°C

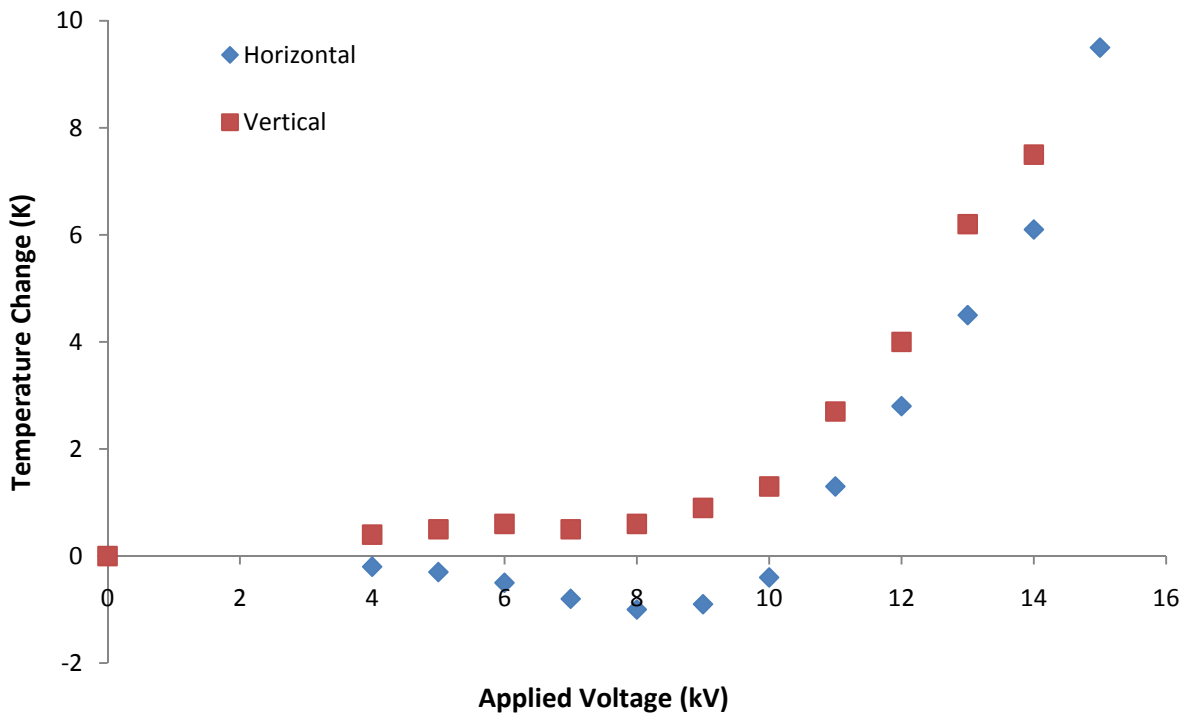


Figure 6.18: Comparison of Outlet Temperature Change of an EHD gas pump in Vertical and Horizontal Orientation at 67% humidity and 23°C

6.6 EHD Gas Pump Humidity Effect

The humidity present in the cage varied considerably over the period of experimentation. The humidity in the cage ranged from 55-70% during normal operating conditions of 1 atmosphere and room temperature due to the change of seasons. To achieve high humidity data points (>70%) and low humidity data points (<40%) the humidity was artificially adjusted using the methods described in Chapter 5. The initial observation of the humidity effect is that the onset of corona and onset of spark discharge occurrence varied with respect to humidity. Figure 6.19 shows the relationship between onset of corona, onset of spark discharge, and humidity. At high humidity, onset of corona and onset of spark discharge occurred at lower applied voltages than under the normal operating conditions humidity range. Under mid-range and low humidity, both corona onset and spark discharge occur at slightly higher applied voltages as the humidity decreases.

Similar patterns exist when comparing peak velocity and outlet temperature to humidity. These results are presented in Figure 6.20. Peak velocity is higher in low humidity at 0.8m/s and decreases with respect to humidity until for high humidity the peak velocity is 0.2m/s. The peak velocity for mid-range humidity does tend to decrease as humidity increases but the trend is not as pronounced in this region. There does appear to be a threshold trend occurring where once water vapour levels become significantly high, it starts to affect the performance of the gas pump, while lower humidity may improve performance. Clearly, the gas pump is more effective at transporting air than water vapour. This may be due to water vapour being heavier and being easier to conduct and hence cause early breakdown of the vapour. The temperature values are more sporadic and no definable trend can be determined, but the results do display the pattern of the mid-range data points grouping together. In this case, the low humidity temperature data has a similar value to the mid-range humidity data. However, the high humidity temperature gradient is significantly smaller than the other data. The results suggest humidity does have a significant effect at high and low range; however in the mid-range region the humidity effect is not as discernible.

Based on these results an EHD gas pump in a CPL have be affected by humidity. The main concern for application in the vapour leg of the CPL is with the working fluid Freon R134a. If concentrations of wet Freon are too high then the environment in the gas pump will be similar to the high humidity case. In this case the performance of the pump may not be significantly affected as the incoming gas velocity will be high and the power requirements will be lower, but premature spark discharge may cause the Freon to break down, which is of concern. Therefore the humidity effect is important in terms of gas pump design and implementation in a CPL.

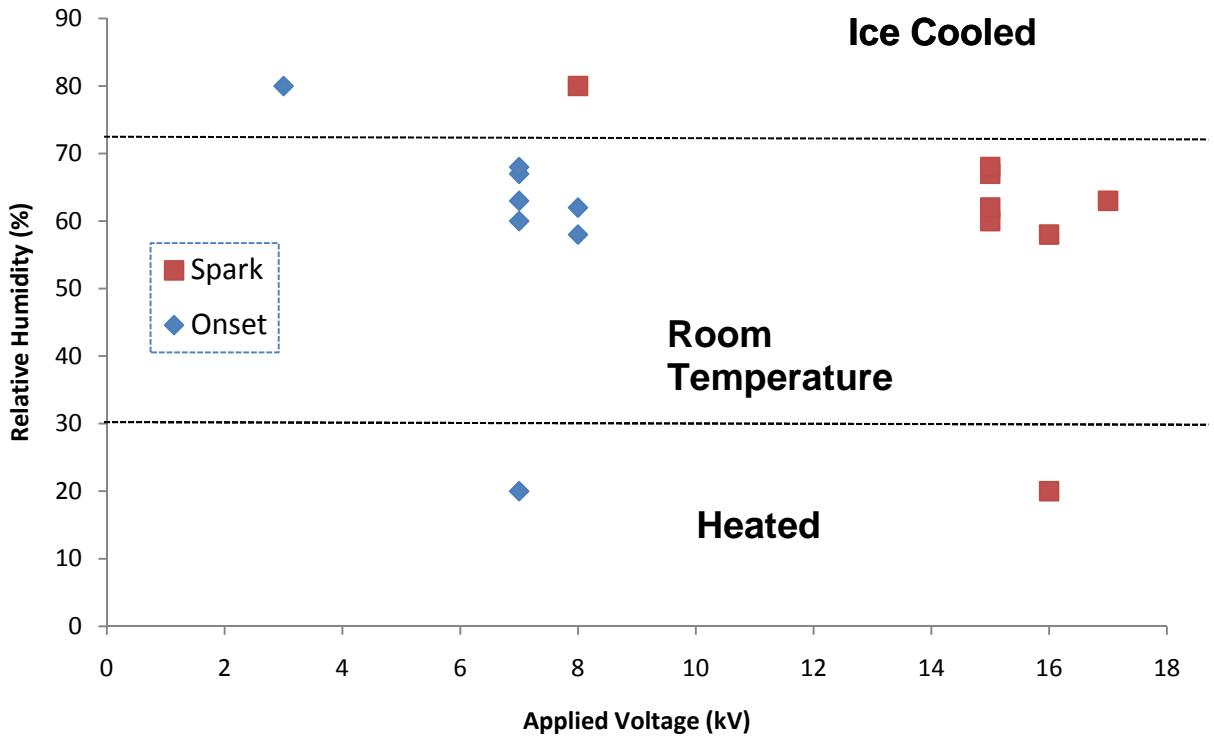


Figure 6.19: Corona onset and spark discharge with respect to relative humidity

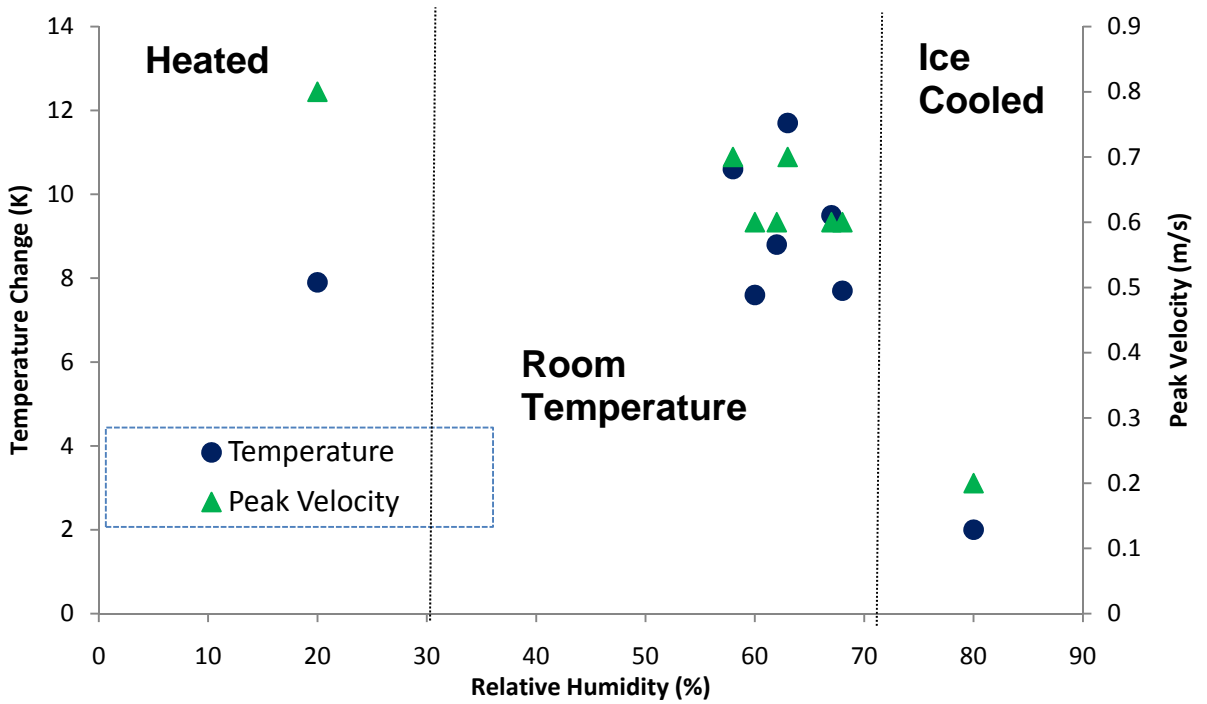


Figure 6.20: Temperature and Flow Velocity vs. Relative Humidity

6.7 Ambient Temperature Effect

The difference in temperature measurements may be less of a humidity effect and more due to the ambient temperature present in the cage during the high humidity and low humidity experiments. Figure 6.21 displays the outlet temperature with respect to ambient temperature and Figure 6.22 displays the peak velocity with respect to ambient temperature. The gas pump was operated at ambient temperatures of 17°C (Cold), 23°C (Room) and 50°C (High). In all experiments the temperature outside the cage was room temperature with the gas pump in horizontal orientation. The room temperature curves display the expected curves for both temperature and velocity. The high temperature velocity curve is significantly different.

The velocity does not plateau but continuously rises and reaches a maximum velocity of 0.8m/s. The temperature change for the high temperature experiment curve resembles the curves of the other data sets in room temperature conditions with an initial drop and then a steep rise after the EHD flow has stabilized. The cold temperature velocity curve resembles the room temperature curve except the velocity declines slightly at 14kV. The velocity decline could be due to a fluctuation in the instrumentation. However, as the colder air starts to heat up the changing the flow pattern may cause a decline in velocity. Further investigation at cold temperatures is needed. The temperature curve however, consistently rises to a 12°C gradient at spark discharge. The greater increase in temperature is probably due to the system taking in heat from outside the cage heating the air inside the cage before it enters the pump on top of the heat generation from the pump itself. From the results it appears higher temperatures may improve velocity, while colder temperatures may allow the pump to reach higher outlet temperature gradients. In a CPL, the Freon will be entering the pump as primarily a vapour in the range 20°C - 25°C if not higher. Therefore it is unlikely the cold temperature scenario would occur and any negative ambient temperature effects are also unlikely. It is possible that at the temperature and pressure in the CPL vapour leg and the gas pump environment would resemble the temperature conditions.

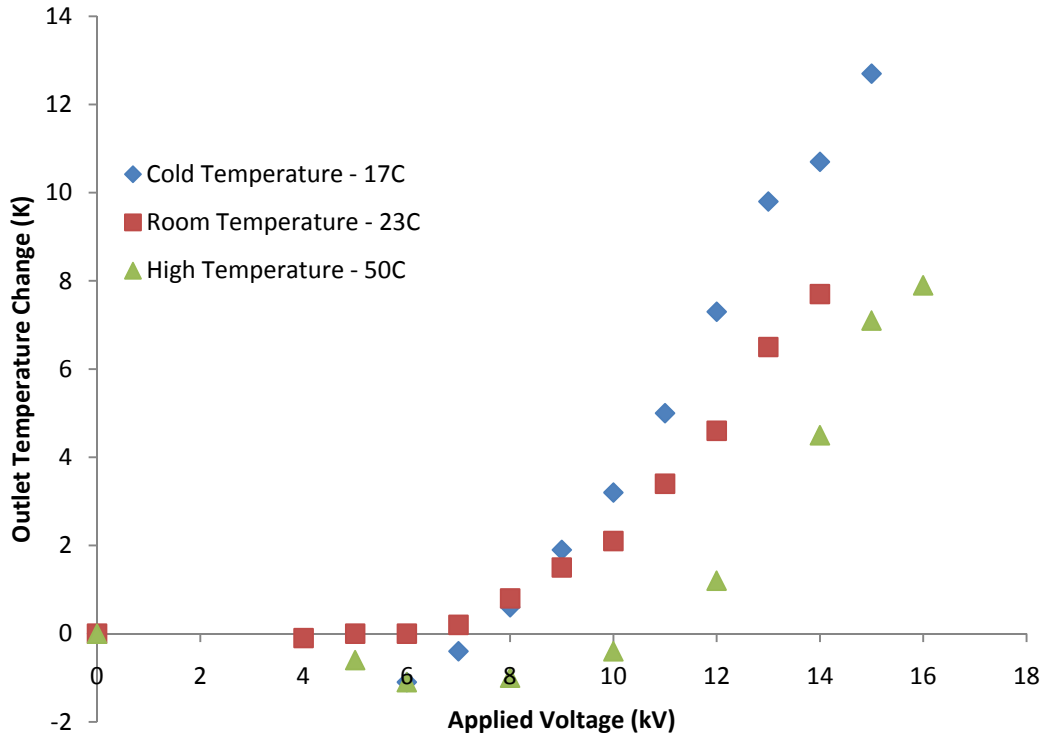


Figure 6.21: Comparison of Outlet Temperatures from differing Ambient Temperatures on an EHD Gas Pump in horizontal orientation

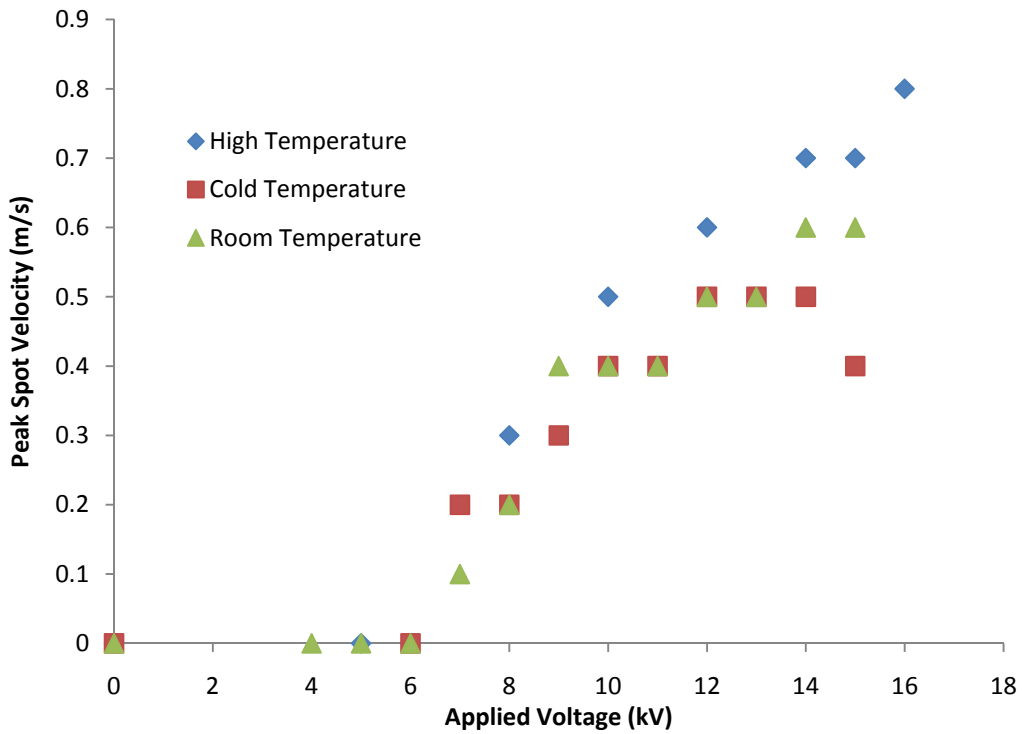


Figure 6.22: Comparison of Peak Spot Velocity from differing Ambient Temperatures on an EHD Gas Pump in horizontal orientation

6.8 Effect of Ehd Number

As discussed in Chapter 3 the Ehd number is the ratio of the electrophoretic force to the viscous forces. As mention previously in the evaporator section the Ehd number is 0 due to an extremely weak current. However, as explain previously the EHD gas pump flow is induced by different EHD phenomena and generates a strong electrophoretic force similar to what is displayed in Figure 3.2. Therefore it is necessary to calculate the Ehd number for the EHD gas pump and determine its relationship to the flow [57]. Figure 6.21 displays the Ehd number to the peak spot velocity, while Figure 6.22 displays the volumetric flow vs. Ehd number. The measured velocity and volumetric flow were performed at the same time for this case so humidity, temperature and time of day are the same for both horizontal datasets and vertical datasets. In Figure 6.21 the Ehd number is calculated at each voltage level for two horizontal orientation datasets and two vertical orientation datasets. In all 4 cases the curves collapse suggesting the Ehd number and therefore the electrophoretic force is the dominant force controlling the flow. Figure 6.22 the volumetric flow and Ehd number is calculated for 2 horizontal orientation datasets and 1 vertical orientation dataset. The volumetric flow results also collapse about the Ehd number further suggesting the Ehd forces are controlling the flow rate. At the expected operating voltage range of the EHD gas pump in the CPL of 11-14kV it is expected an Ehd number of 2×10^5 - 3×10^5 suggesting a strong electrophoretic force is present.

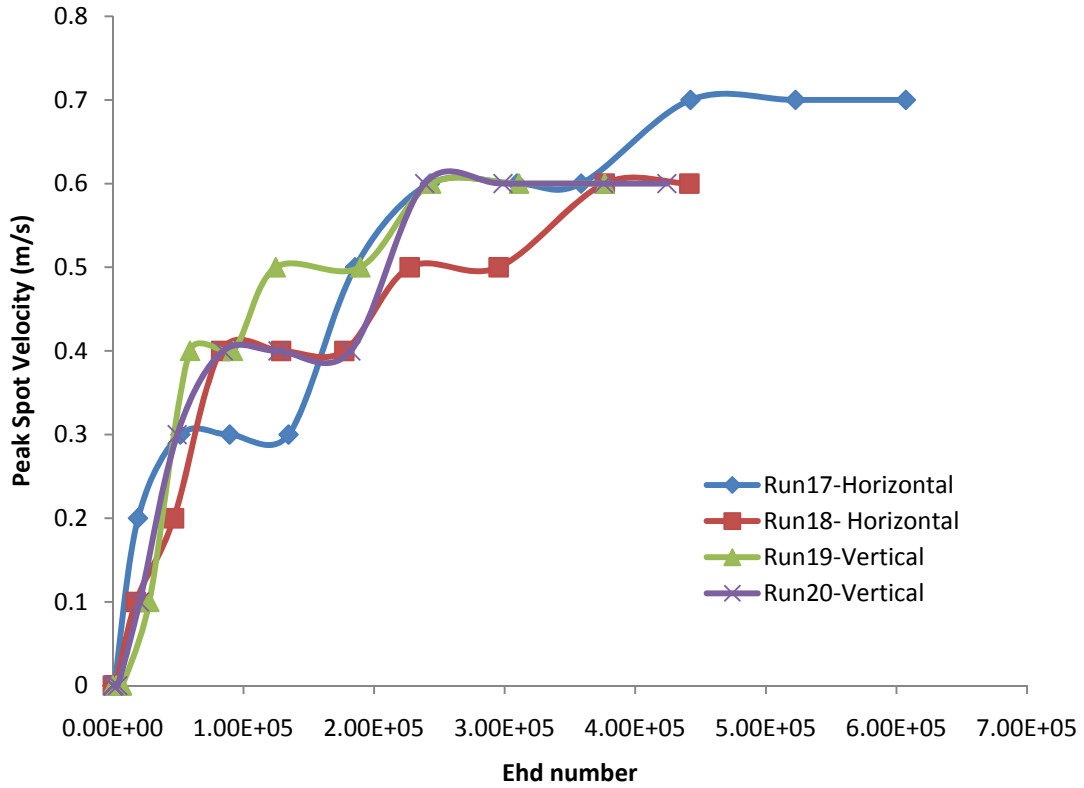


Figure 6.23: Peak Spot Velocity vs. Ehd Number for an EHD Gas Pump

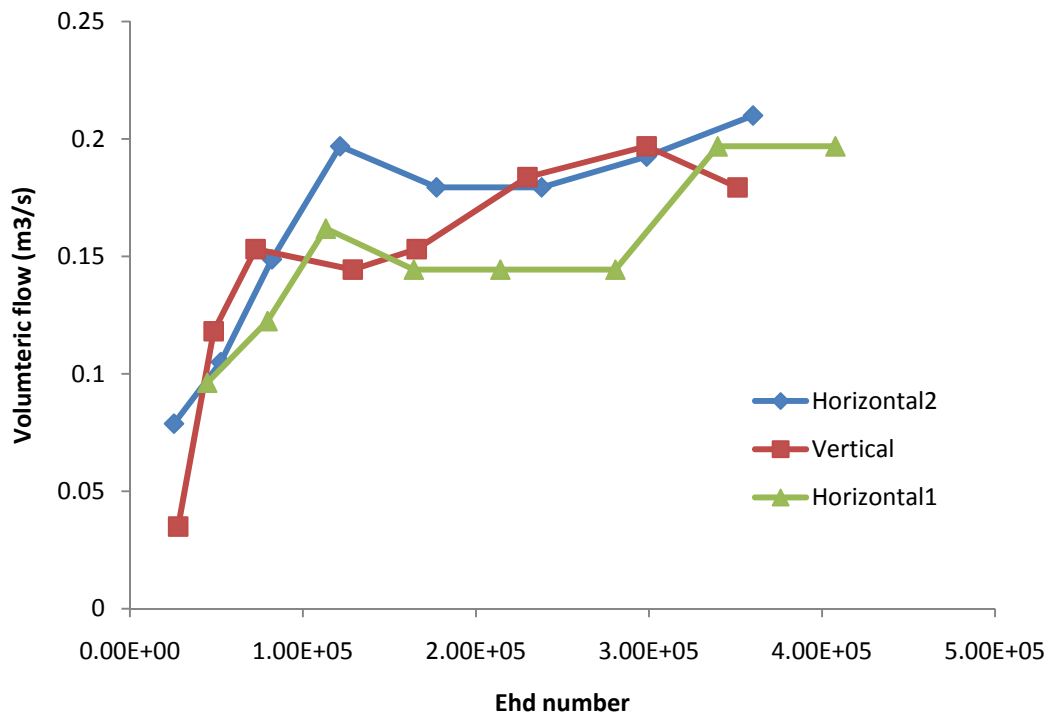


Figure 6.24: Volumetric Flow vs. Ehd Number for an EHD Gas Pump

6.9 Free Convection Flow and Temperature Profiles

The flow and temperature profiles were taken in the x and y direction of both a horizontally and vertically oriented convergent plate rectangular gas pump. The outlet of the gas was divided into 12 equal squares, 4 in the x direction and 3 in the y direction. For each square the temperature and flow velocity were taken using a hot-wire anemometer. The measurement grid applied to the outlet of the gas pump is presented in Figure 5.4. The EHD gas pump is operating under high voltage creating EHD forces the mass and heat is being transported based on the principles of free convection. Measurements were taken every 1kV from onset of corona to onset of spark discharge. The profiles were taken at just after onset of corona, but before EHD flow stabilization (8kV), after EHD flow stabilization (11kV) and at spark discharge (14kV). Video was also taken of the corona wire at each voltage level to examine the corona and compare it to the flow and temperature profiles. Pictures of the corona at each voltage level are presented in Figure 6.5. Also while the picture at 14kV occurred during spark discharge no sparks were captured in the picture, however sparks were observed.

The horizontal flow profiles, Figures 6.25-6.27, all have a similar flow pattern of a peak at the bottom centre to centre right of the gas pump. While, there is little variation in the 8kV flow profiles there is significant variation in the 11kV and 14kV flow profiles between the minimum and maximum measured velocities. The variation of flow velocity means a non-uniform flow is exiting the gas pump. Possibly to the EHD flow which can circulate near the electrode or possibly due the geometry of the pump.

The vertical flow profiles, Figures 6.31-6.33, have a similar result to the horizontal flow pattern the main difference being the pattern is almost a mirror image with the low point being found in the bottom corners, but with a slightly lower flow in the top right as oppose to the top left and the high point being centre left. In comparing these profiles to the pictures the peak velocity seems to occur near where the corona is brightest and the low point where the corona is the dimmest.

Suggesting the corona strength and therefore the EHD forces across the electrode are not equal and produce stronger flows in certain sections of the gas pump compared to others. Also there are clear pegs inside the gas pump near where some of the low velocities were recorded. Clearly both the geometry and condition of the corona electrode affect the flow pattern of the EHD gas pump although the entire gas pump geometry may influence the flow pattern in some respect.

The temperature profiles in the horizontal orientation, Figures 6.28-6.30, display an increasing temperature across the outlet from the low in the top left to a peak in the bottom right of the pump. Furthermore, while there is little variation in temperature at 8kV for any of the profiles again there is a significant gradient in the 11kV and 14kV profile. In the 14kV temperature profile there is over a 10°C difference, which is significant and too large to be from instrumental error or fluctuation.

The vertical orientation temperature profiles, Figures 6.34-6.36, had a similar but less pronounced heating effect. Again the pattern is almost mirrored when compared to the horizontal with the temperature being low in the bottom right and peaking in the top left. Suggesting the heating effect is localized within the pump possible due to the EHD flow forming re-circulating eddies where the EHD forces are strongest allowing the flow in that area to be heated to higher temperatures, while the flow in the other areas are quickly pushed towards the exit before it can absorb much heat. It would also explain the lower temperature gradient in the vertical orientation as the buoyancy forces may inhibit these re-circulating flows from forming. However, the heating could also be from increase wire resistance in one local spot along the corona electrode due to corrosion or possibly a bend in the electrode. Most likely it is a combination of both these factors. The bright spot apparent in the pictures of the corona formation are also near the areas of highest temperature suggesting the wire's condition and geometry is affecting the flow and heat generation. Also it is interesting to note that the bright spot where spark discharge is always first observed. In terms of the EHD gas pump

operating in a CPL this results suggest uneven distribution of the EHD forces would lead to a non-uniform outlet flow pattern. This may be used to optimize the pump performance or could even cause issues in the CPL depending on how it is affected by the incoming flow pattern.

:

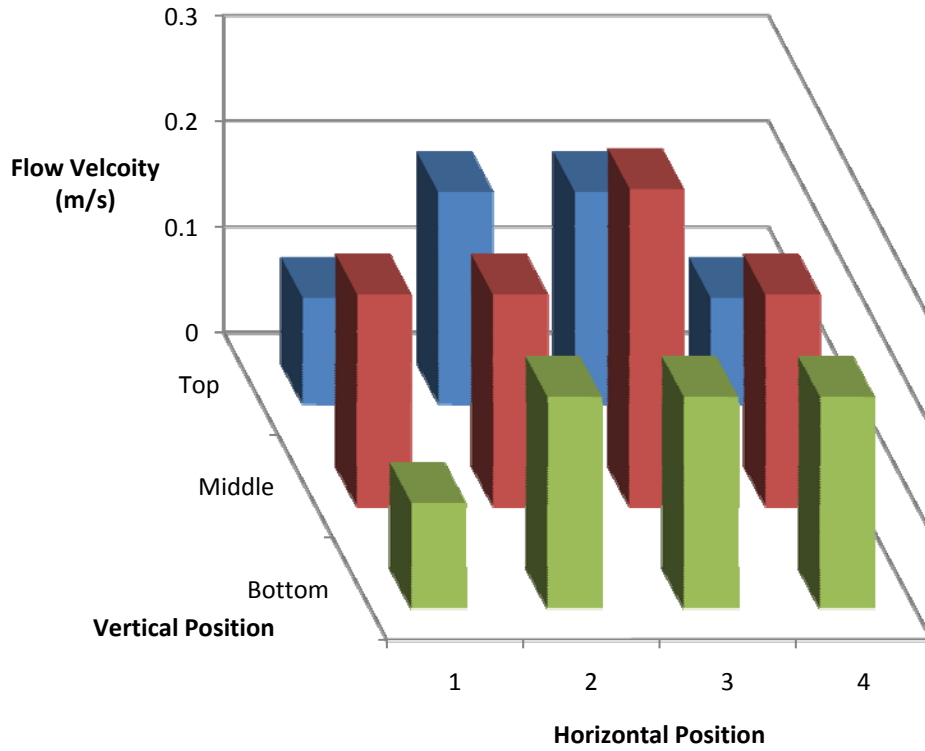


Figure 6.25: Flow Profile for an EHD Gas Pump at 8kV in Horizontal Orientation

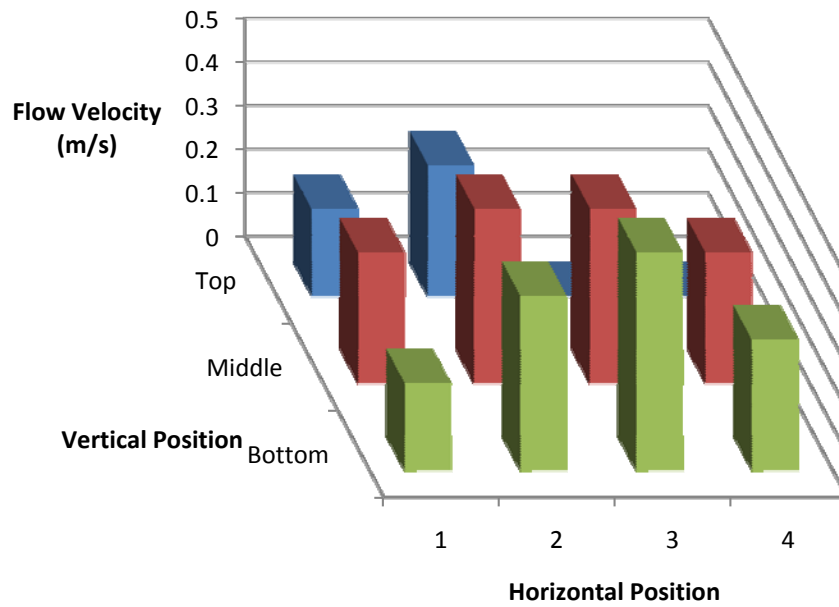


Figure 6.26: Flow Profile for an EHD gas pump at 11kV in Horizontal Orientation

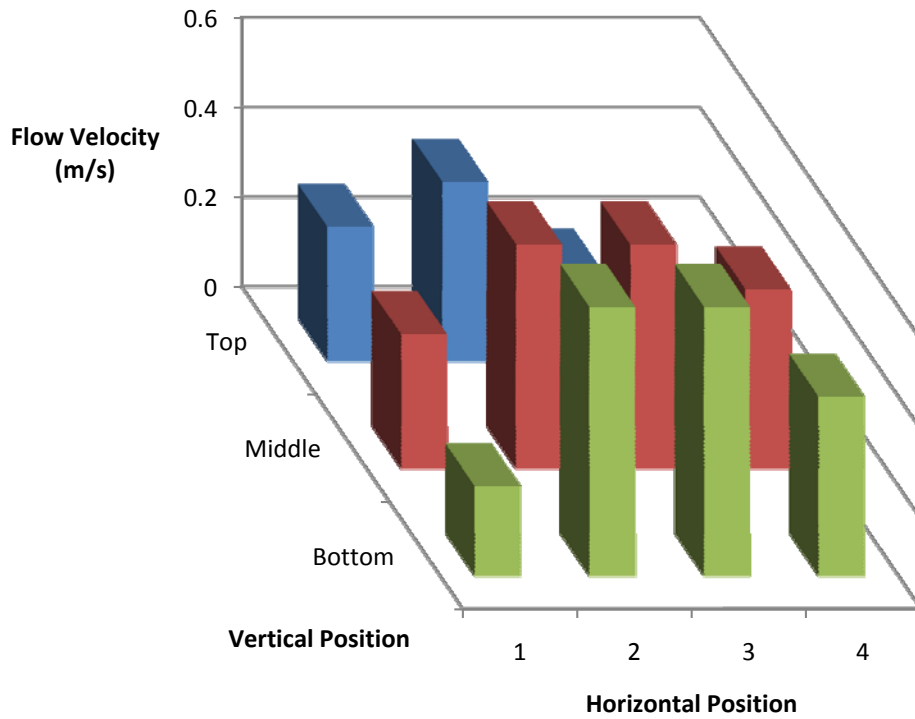


Figure 6.27: Flow Profile for an EHD gas pump at 14kV in Horizontal Orientation

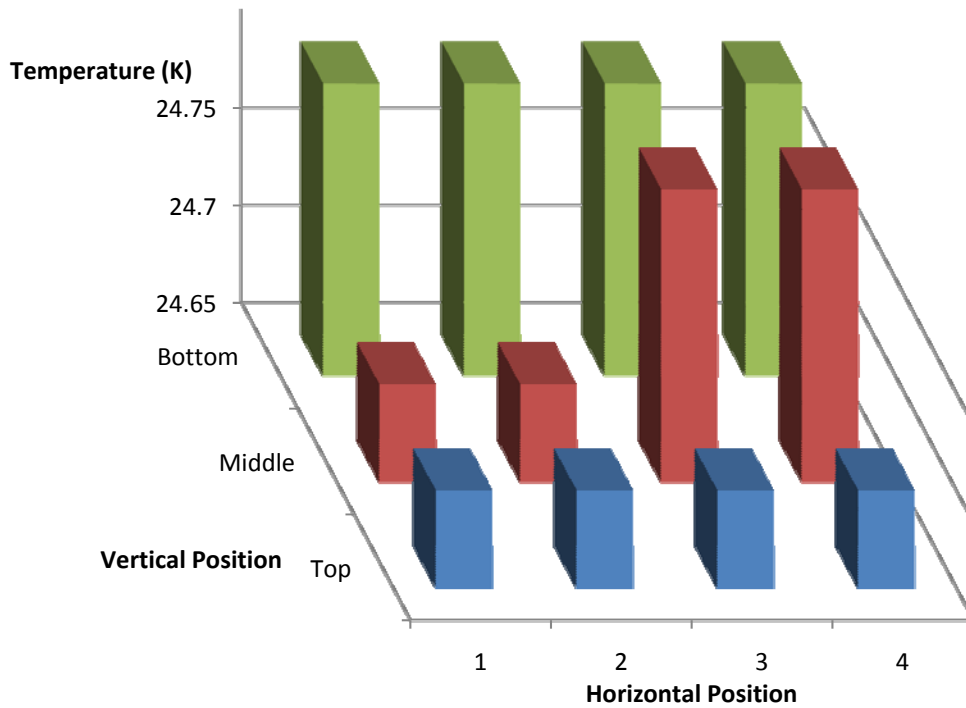


Figure 6.28: Temperature Profile for an EHD Gas Pump at 8kV In Horizontal Orientation

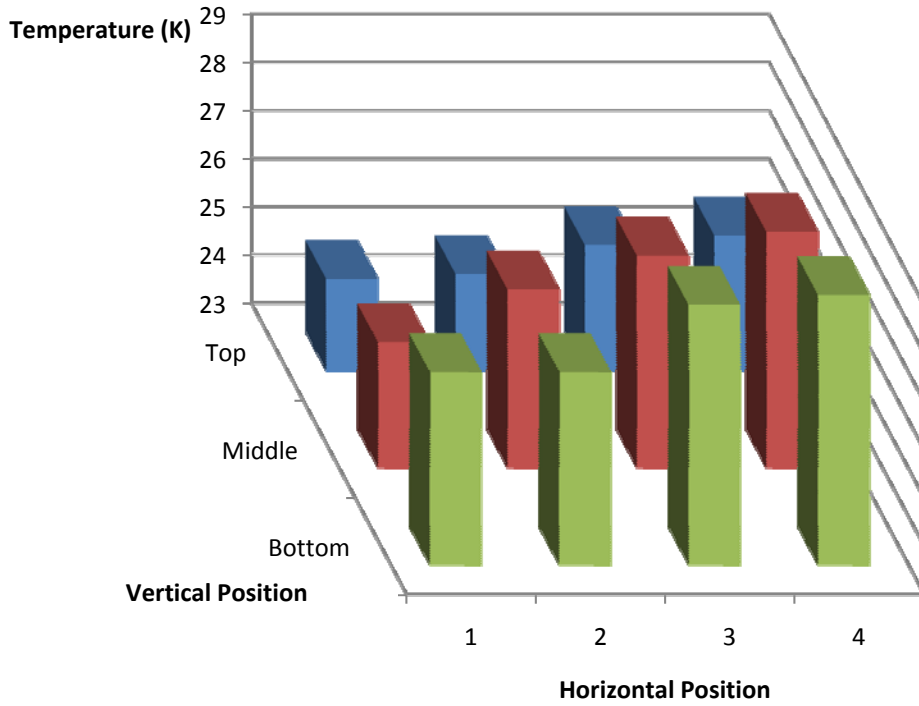


Figure 6.29: Temperature Profile for an EHD Gas Pump at 11kV In Horizontal Orientation

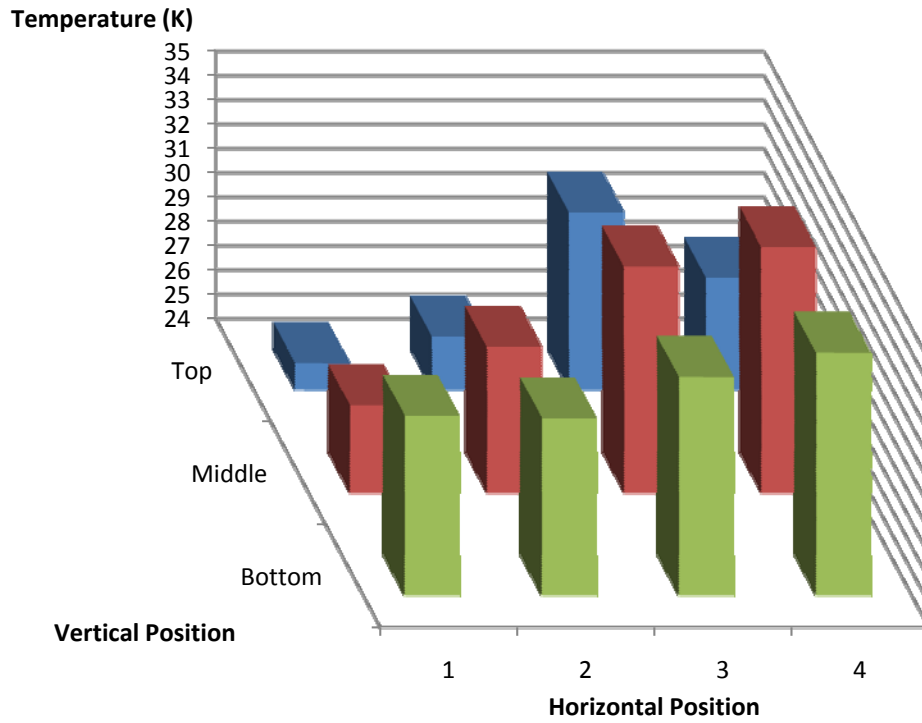


Figure 6.30: Temperature Profile for an EHD Gas Pump at 14kV in Horizontal Orientation

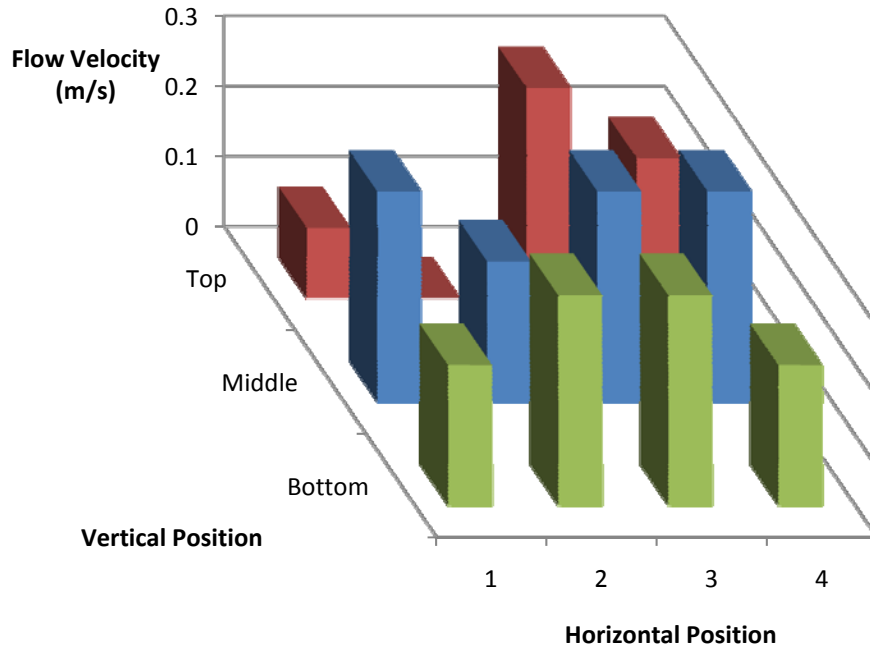


Figure 6.31: Flow Profile for an EHD Gas Pump at 8kV In Vertical Orientation

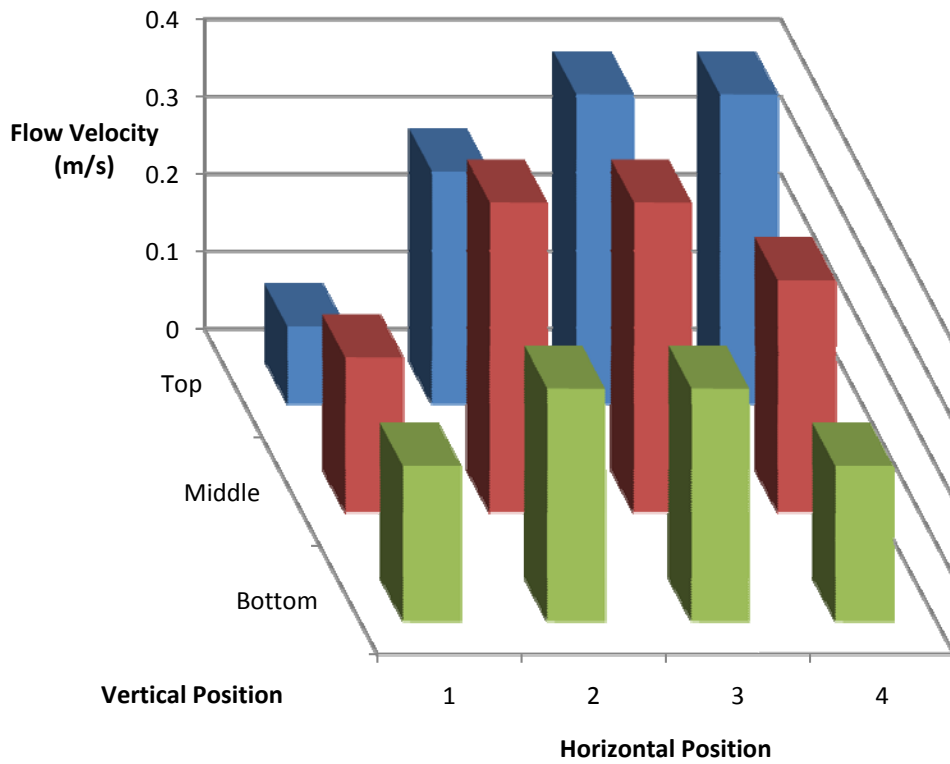


Figure 6.32: Flow Profile for an EHD Gas Pump at 11kV In Vertical Orientation

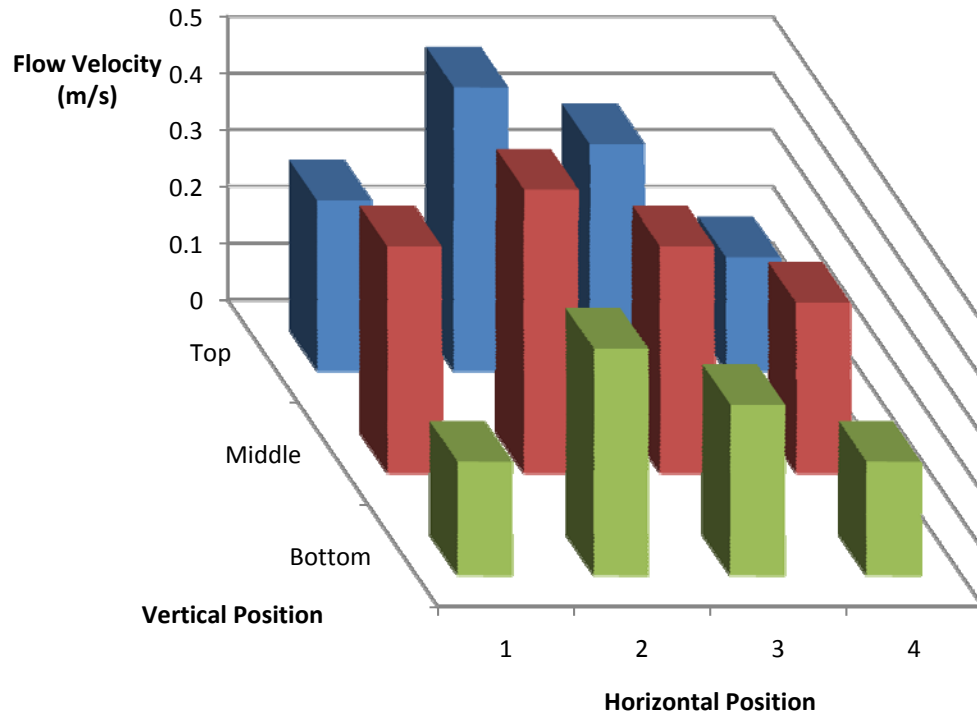


Figure 6.33: Flow Profile for an EHD Gas Pump at 14kV in Vertical Orientation

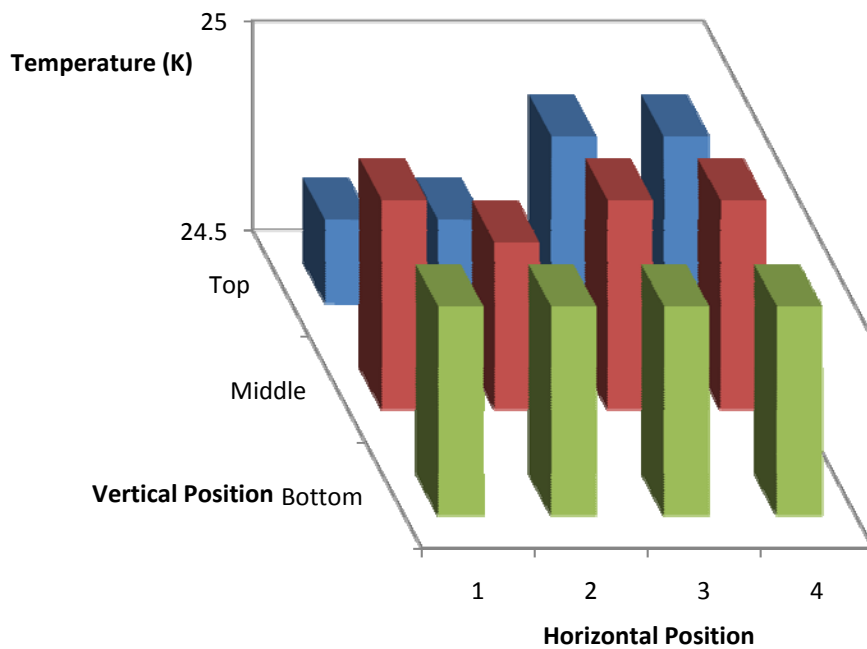


Figure 6.34: Temperature Profile for an EHD Gas Pump at 8kV in Vertical Orientation

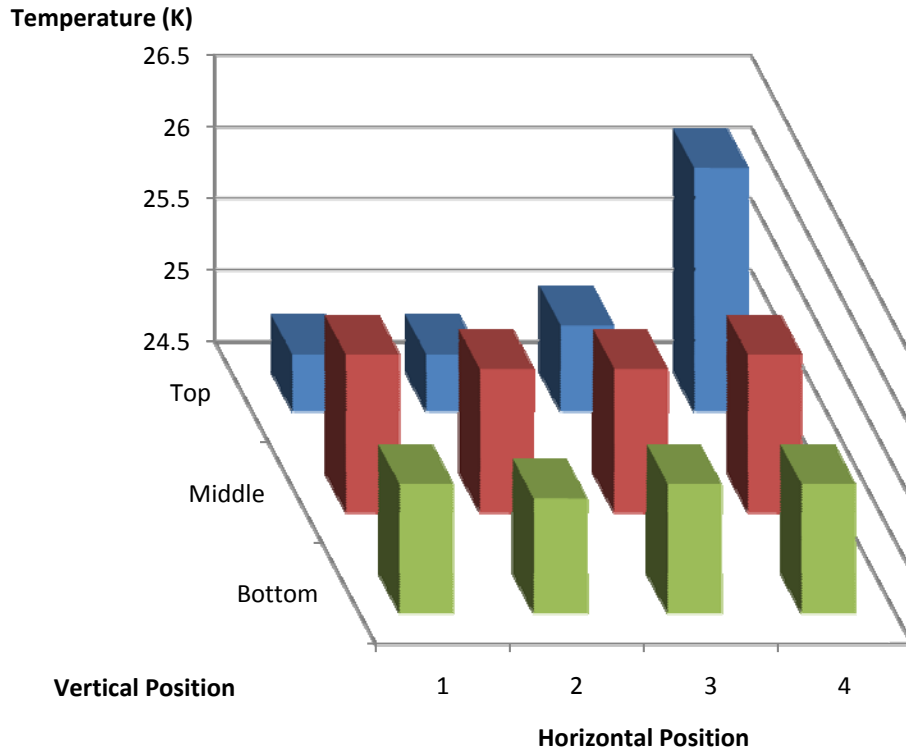


Figure 6.35: Temperature Profile for an EHD Gas Pump at 11kV in Vertical Orientation

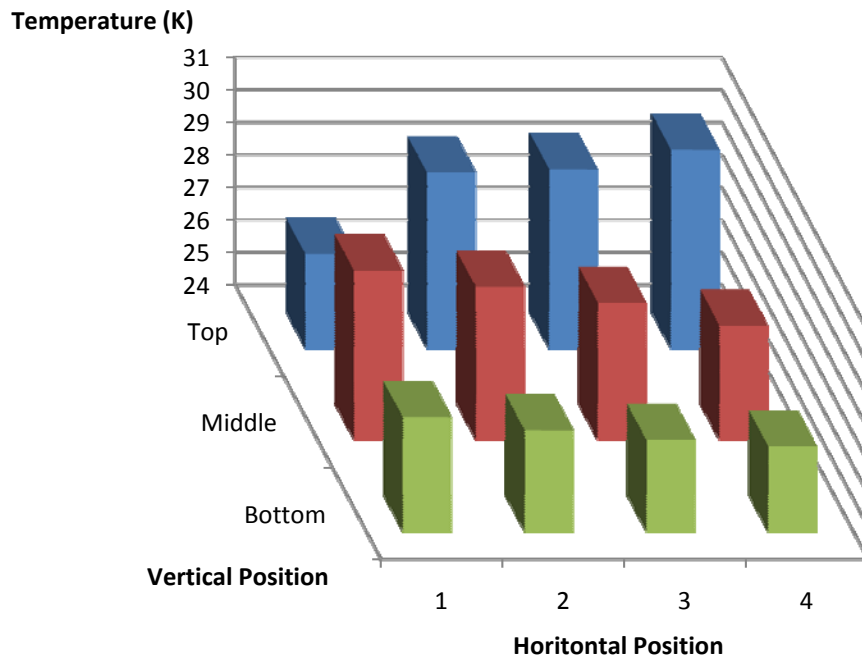


Figure 6.36: Temperature Profile for an EHD Gas Pump at 14kV in Vertical Orientation

6.10 Forced Convection Flow Profile

To determine if the gas pump geometry is affecting the outlet flow pattern an experiment to determine the flow profile for a forced convection situation was performed. An electric fan blew air into the pump without high voltage being applied. Therefore there are no EHD forces present or any Joule heating or heating effects present. As such only the flow profile is presented in Figure 6.38. Two important observations were made from studying the forced convection flow profile. First the flow is reduced from flowing through the gas pump, but seems to naturally flow faster through the bottom of the pump and is slowest along the top confirming some of the observations made from the free convection profiles. Also the flow seems to peak in the centre right similar to the free convection flow pattern. Therefore the gas pump geometry is clearly affecting the flow pattern, which must be a consideration when designing the gas pump for the CPL. However, the forced convection flow pattern does not match the free convection flow patterns of the EHD case. One primary difference between forced convection and EHD is a low spot occurring in the centre left of the outlet. Another difference between the cases is in EHD the flow is typically higher in the centre than to the left of the pump. In the forced convection case there is a consistent low spot on the left centre side of the outlet. Therefore the EHD forces are also to a degree affecting the flow pattern as well as the patterns in the forced convection case and EHD free convection do differ in outlet flow pattern. So, the incoming flow, gas pump geometry, electrode geometry, corona distribution pattern and location of EHD forces will all have a significant impact on the outlet flow pattern. To determine the exact significance of each factor further research needs to be undertaken where incoming flow and outgoing flow is measured for the case when both free and forced convection is occurring.

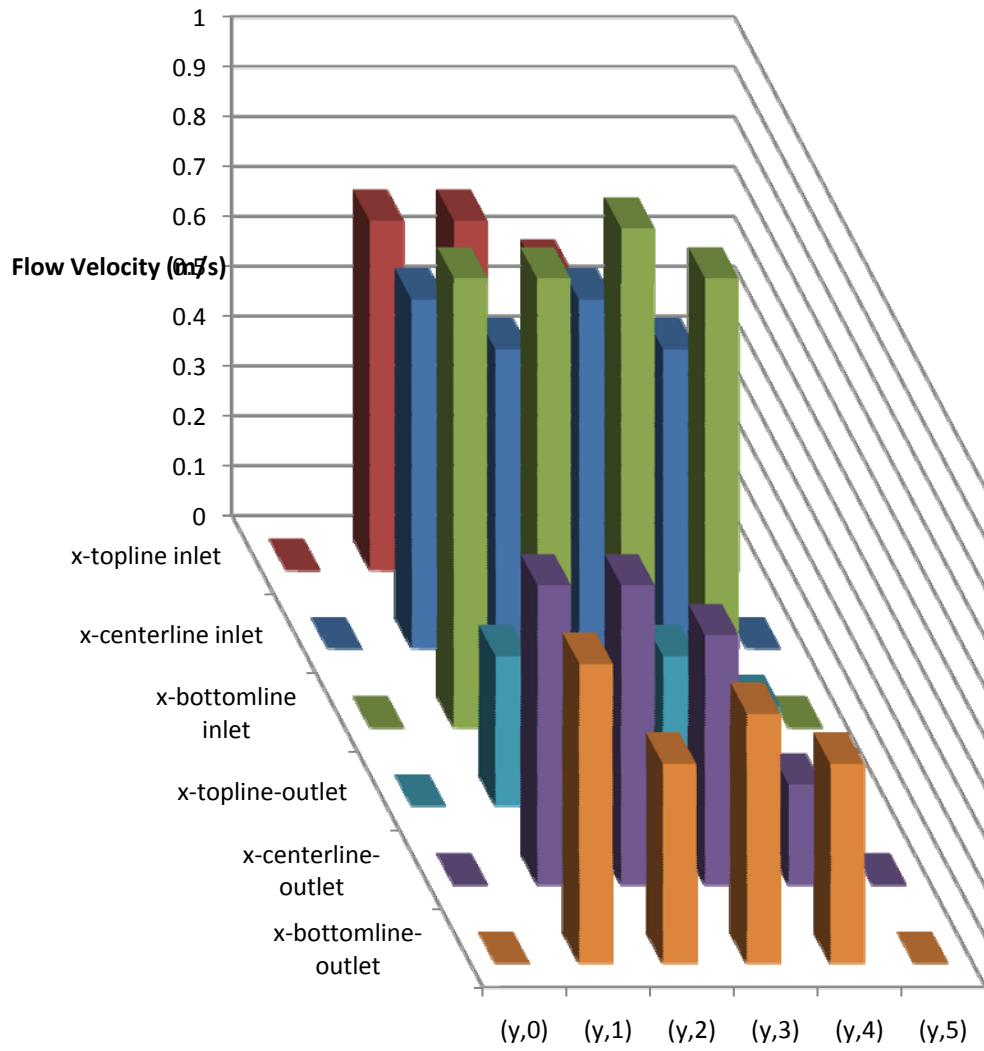


Figure 6.37: Forced Convection Air Flow Velocity Profile

6.11 EHD Gas Pump for Freon Loop

After reviewing the results of the EHD gas pump there are some concerns in terms of implementation in a CPL. Firstly, there are certain conditions such as in the cold temperature case that could reduce the effectiveness of the gas pump. However, these concerns are easy to address as conditions appear to be able to be mitigated or avoided altogether through design. Secondly, there are conditions that could lead to premature spark discharge. Spark discharge is a concern as it would cause the Freon to break down damaging the CPL. None of these conditions however are unavoidable and just will mean the gas pump will have to restrict operation into an acceptable range of humidity. Also the EHD forces seem to have erratic behaviour at lower applied voltages and the gas pump performance seems to be reduced as the flow is unstable. This may cause issues in a start up or shut down scenario, but suggests there is an optimal voltage and power level to operate in and this level needs to be determined through additional experimentation specific to the application. The EHD forces are also affecting the flow pattern beyond just the geometry of the pump as seen from the free and forced convection profiles. Also the geometry of the pump seems to direct the flow towards the stronger EHD forces meaning in forced convection, with EHD and free convection present, there may be an even larger disparity in the outlet flow profiles. In the CPL then with a properly designed gas pump the flow can definitely be enhanced with EHD beyond that possible by forced convection alone. Finally, the gas pump needs to be placed in a horizontal orientation as any angle will either enhance performance due to buoyancy forces or be reduced by gravitational forces if angled in a downward direction, which is not representative of extraterrestrial applications.

7. Concluding Remarks

The experimental results and analysis generated in this work have led to several conclusions. The optimal diameter for an electrode in an EHD enhanced evaporator for use in the current CPL design has been theoretically calculated. The use of the larger diameter should allow for improved efficiency in the evaporator section of the CPL by increasing the EHD forces without significantly increasing the flow resistance without increasing due to the reduction in the flow area.

The gas pump experiments determined that the EHD gas pump is affected by the following factors:

- Orientation with respect to gravity of the gas pump. The buoyancy forces aid in the development of flow at lower voltages generating higher flow rates and lower temperature gradients at the outlet. Impact at high flows is negligible.
- Humidity has a threshold effect on the gas pump. Once humidity nears 80% relative humidity the pump efficiency significantly reduces as the water vapour begin to cause spark discharge before EHD motion can take effect.
- High ambient temperatures improve gas pump performance, while colder temperatures may impair gas pump performance as the fluid is more mobile at higher temperatures.
- The Ehd Number is the dominant dimensionless number in determining how the EHD forces are controlling the flow.
- The geometry of the gas pump and corona electrode will influence where in the gas pump EHD flow develops and stabilizes, and the resulting flow patterns at the exit of the pump. Hence geometry of the design is important for optimizing gas performance.
- Electrode material is important as the resistivity, thermal conduction and other physical properties can offer better current-voltage

characteristics and physical characteristics that will allow for a more consistent flow and may result in a longer life span for the electrode and gas pump.

- Condition of the electrode is an important factor in considering the design of the gas pump as the corona will cause a degradation due to ablation of the electrode which was observed to affect performance.

These factors and the associated effects need to be considered when designing a pump an EHD gas pump for use in a CPL. Use of the Ehd number is an appropriate parameter for designing an EHD gas pump.

Finally, the experimental results and theoretical analysis suggest that with the addition of an EHD gas pump in the CPL there will be an enhancement of the mass flow rate in the vapour leg and an increase in the stability of the flow. Additional improvement of flow efficiency and stability in the vapour leg can also be achieved by optimizing the design of the cooling jacket.

The design of the gas pump for use in an EHD enhanced CPL should be a wire-plate configuration with the geometry of the pump designed specifically for the loop. The design should allow the corona electrode to remain straight and taut. The gas pump should use a corrosion resistant material such as stainless steel although other appropriate materials compatible with Freon have not been investigated. Preferably, the gas pump should be operated in the section of the vapour leg that is fairly dry or of a high quality as condensation will lead to early spark discharge. Therefore the pump should be situated a safe distance from the outlet of the evaporator. The pump should operate in the expected temperature range without issue. The pump should be orientated in a horizontal position to better model a zero gravity environment, this will allow for the beneficial effects of the gas pump to occur at lower power levels and possibly use the same power supply as the evaporator. An operating voltage and current should be based on finding an optimal EHD number that balances the pump's output velocity with its heat generation effects.

8. Recommendations for Future Work

While certain conclusions have been reached additional work is recommended to optimize the performance of the CPL for future experimentation and application to extraterrestrial environments.

First, a gas pump design that is suitable for a Freon environment needs to be finalized with consideration of the proper material choices. The design should incorporate the designs with the best performance from the available literature as well as material choice based on its compatibility with Freon, using the design work and findings presented in this work.

The exploration of charge injection as opposed to electrophoresis effects should also be considered as this may be a more effective mechanism than the gas pump studied in this work, with less chance of sparking. The literature review suggests charge injection may lower the chances of Freon break down in the system.

The new corona electrode needs to be installed in the current experimental CPL. The EHD gas pump also needs to be implemented into a CPL experimental loop to determine the effectiveness of the expected enhancement.

Lastly further experimentation on the CPL should be performed with respect to minimizing the gravitational effects. The experiment should use a horizontal CPL configuration and vary g by changing the elevation of the loop with respect to gravity. The experiment then would simulate a micro-gravity or zero gravity environment reasonably well from a mass transport perspective. Such experiments would be able to determine some of the effects of micro-gravity on the CPL and better describe its effectiveness in these environments.

9. References

1. "VSS Enterprise Completes First Manned Glide Flight" Virgin Galactic News. <http://www.virgingalactic.com/news/item/vss-enterprise-completes-first-manned-glide-flight/>, October 10, 2010.
2. M. El-Genk. "Deployment history and design considerations for space reactor power systems" Acta Astronautic, 2008.
3. F.J. Stenger. "Experimental feasibility study of water-filled capillary-pumped heat transfer loops", NASA TM X-1310, NASA Lewis Research Center, Cleveland, Ohio, USA, 1966.
4. B. Alan Harmon and W. A. Bohne, "A Look Back at Assembly and Test of the New Horizons Radioisotope Power System", AIP conference proceedings, 2008.
5. J. Straub, "The role of surface tension for a two-phase heat and mass transfer in the absence of gravity", Experimental Thermal and Fluid Science **9**:253-273, 1994.
6. S. Benner, G. Durback, K. Kolos and R. Bayt, "A breadboard flight experiment for two-phase flow visualization in microgravity", 33rd AIAA Aerospace Science Meeting and Exhibit, Reno, USA, January 9-12, 1995.
7. M. El-Genk. "Space reactor system with no single point failures", Nuclear Engineering and Design **238**:2245-2255, 2008.
8. T. Schriener and M. El-Genk. "Methods for determining operation life and reactivity depletion for space reactors with fast energy spectra", Progress in Nuclear Energy **51**:366-373, 2009.
9. S. Shelestynsky, Two-Phase Flow in Capillary Pumped Loops, Faculty of Engineering, McMaster University, Hamilton, Ontario, Canada. 2007.
10. K. Jentung. "Heat Pipes and Capillary Pumped Loops". NASA Goddard Space Flight Center: American Society of Mechanical Engineering, Heat Transfer Division. HTD v236, pg.1-17, 1993.
11. Z. C. Liu, W. Liu, and A. Nakayama. "Flow and heat transfer analysis in porous wick of CPL evaporator based on field synergy principle".

Published online: 4 January 2007 Heat Mass Transfer **43**:1273–1281, 2007

12. Y. Yoshida, Y. Honma, T. Narabayashi, and Y. Shimazu. "Study for the space craft for interplanetary cruise examination of the thermal efficiency. Proceedings of the 16th International Conference on Nuclear Engineering ICONE16, 2008
13. F. Maidanik, G. Fershatater, V.G. Psatukhov, K.A. Goncharov, O. Zagar and Y. Golovanov. "Thermoregulation of looped with capillary pumping for space use" SAE Journal **92**:1169, 1992.
14. E. Bazzo and R.R. Riehl. "Operation characteristics of a small scale capillary pumped loop", Applied Thermal Engineering **23**:687-705, 2003.
15. J.S. Chang, A.J. Kelly, J.M. Crowley, Handbook of Electrostatic Process. Marcel Dekker, New York, New York, USA, 1995.
16. H. Tsubone, J. Ueno, B. Komeili, S. Minami, G.D. Harvel, K. Urashima, C.Y Ching, and J.S. Chang, "Flow characteristics of dc wire-non-parallel plate electrohydrodynamic gas pumps", Journal of Electrostatics **66**: 115-121, 2008.
17. B. Komeili, J.S. Chang, G.D. Harvel and C.Y. Ching. Electrohydrodynamically Enhanced Capillary Evaporator. Faculty of Engineering, McMaster University, Hamilton, Ontario, Canada, 2007.
18. G.D. Harvel, B. Komeili, C.Y. Ching and J.S. Chang, "Electrohydrodynamically Enhanced Capillary Evaporator", Transactions on Dielectrics and Electrical Insulation IEEE Vol. **16**(2), 2009.
19. J. S. Chang, H. Tsubone, N. Buenoconsejo Jr., J. Ueno, G.D. Harvel, J. Mizeracyzk and K. Urashima, "Corona Discharge and Flow Characteristics of Wire-Plate Type Electrohydrodynamic Gas Pumps: Ground Plate Convergent Angle Effect", 28th ICPIG, Prague Czech Republic, July15-20 2007.
20. J.S. Chang, J. Ueno, H. Tsubone, G.D. Harvel, S. Minami and K. Urashima, "Electrohydrodynamically induced flow direction in a wire-non-

- parallel plate electrode corona discharge”, *Journal of Physics D: Applied Physics* **40**: 5109-5111, 2007.
21. F. Soetomo, G. M. Colver and K. Forouraghi, “Micro-force measurement of drag on a small flat plate in the presence of a corona discharge”, 4eme Conference Societe Francaise d'Electrostatique 2004.
 22. J. Podlinski, J. Dekowski, J. Mizeraczyk, and J.S. Chang, “EHD flow in a wide electrode spacing spike-plate electrostatic precipitator under positive polarity”, 4eme Conference Societe Francaise d'Electrostatique 2004.
 23. B. Komeli, J. S. Chang and G. D. Harvel, “Polarity Effect and Flow Characteristics of Wire-Rod Type Electrohydrodynamic Gas Pump” Annual Report Conference on Electrical Insulation and Dielectric Phenomena 2006.
 24. B. Komeili, J.S. Chang, G.D. Harvel, C. Y. Ching and D. Brocilo, “Flow characteristics of wire-rod type electrohydrodynamic gas pump under negative corona operations”, *Journal of Electrostatics* **66**:342-353, 2008.
 25. J. S. Chang, G. D. Harvel, H. Tsubone, and K. Urashima, “Narrow flow channel driven EHD Gas Pump for an Advanced Thermal Management of Microelectronics”, *IEEE Transactions on Industry Applications* **46**(3):1151-1158, 2010.
 26. J. Cotton, J. S. Chang, M. Shoukri, and T. Smith-Pollard “Electrohydrodynamically enhanced flow boiling in an eccentric horizontal cylindrical channel”, Annual Report Conference on Electrical Insulation and Dielectric Phenomena 2002.
 27. J. Cotton, D. Brocilo, J.S. Chang, M. Shoukri, and T. Smith-Pollard, “Numerical Simulation of Electric Field Distributions in EHD Two-Phase Flow” *IEEE Transactions on Dielectrics and Electrical Insulations* **10**(1), 2003.
 28. H. Sadek, J. Cotton, C.Y. Ching, and M. Shoukri, “Effect of frequency on two-phase flow regimes under high-voltage AC electric fields”, *Journal of Electrostatics*, 2008.

29. J. Cotton, M. Shoukri, and J. S. Chang, "Oscillatory entrained droplet EHD two-phase flow", Transactions of the ASME **123**, 2001.
30. P.A. Vazquez, C. Soria, and A. Castellanos, "Numerical simulation of EHD flows with finite element and particle methods" 4eme Conference Societe Francaise d'Electrostatique 2004.
31. M. Cabaleiro, G. DiPrimio, and G. Artana, "Filamentary EHD actuation on the surface of bodies contoured by compressible flows" 4eme Conference Societe Francaise d'Electrostatique 2004.
32. F. Pontiga, C. Soria, A. Fernandez-Rueda and A. Castellanos, "The effect of electrode composition on ozone generation", 4eme Conference Societe Francaise d'Electrostatique 2004.
33. P. Atten, "On use of an ionic pump in a convector heater", IEEE Transactions on Industry Applications **32**(1):80-89, 1996.
34. W. Grassi, D. Testi, and M. Saputelli. "Heat transfer enhancement in a vertical annulus by electrophoretic forces acting on a dielectric liquid". International Journal of Thermal Sciences **44**:1072-1077, 2005.
35. M. El-Genk "Space reactor power system concepts with static and dynamic energy conversion", Energy and Conversion Management **49**:402-411, 2008.
36. T. Schriener and M. El-Genk. "Reactivity control options of space nuclear reactors", Progress in Nuclear Energy **51**:2245-2255, 2009.
37. N. Morley and M. El-Genk. "Neutronics and thermal-hydraulics analyses of the pellet bed reactor for nuclear propulsion", Heat Transfer and Fluid Flow, 1994.
38. M. Dumitran, P. Atten, P. V. Notingher, and L. Dascalescu, "Numerical modeling of corona discharges generated in a cylinder-wire-plate electrode arrangement", 4eme Conference Societe Francaise d'Electrostatique 2004.
39. B. Suman. "A steady state model and maximum heat transport capacity of an electrohydrodynamically augmented micro-grooved heat pipe". International Journal of Heat and Mass Transfer **49**:3957-3967, 2006.

40. J. Cotton, A. Robinson, M. Shoukri and C. Y. Chang, Two-phase flow pattern map for annular channels under a DC applied voltage and the application to electrohydrodynamics convective boiling analysis, *International Journal of Heat and Mass Transfer* **48**:5563-5579, 2005.
41. H.G. Wulz and F. Mayinger. "Heat and fluid transport in an evaporative capillary pump", *International Journal of Energy Research* **17**:18, 1993.
42. J.M. Tournier and M. El-Genk. "Reactor lithium reactor heat pipes for HP-STMCs Space Reactor Power System".
43. H.G. Wulz and F. Mayinger. "Heat and fluid transport in an evaporative capillary pump", *International Journal of Energy Research* **16**:879-896, 1992.
44. G. Bayon, "Present applications of neutron radiography in France", *Nuclear Instruments and Methods in Physics Research A* **424**:92-97, 1999.
45. V. Agarwal, A.K. Jana, G. Das, and P.K. Das, "Taylor bubbles in liquid filled annuli: Some new observations", *Physics of Fluids* **19**:10805, 2007.
46. H. Tsubone, J.S. Chang, G.D. Harvel and K. Urashima, "Non-moving component pumping of narrow gas flow channels by an electrohydrodynamic gas pumps", *International Symposium on Electrohydrodynamics*, pg. 151-155, Sarawak, Malaysia, March 25-28 2009.
47. J.S. Chang, G.D. Harvel, H. Tsubone and K. Urashima, "Capillary/Narrow flow channel driven EHD gas pump for an advanced thermal management of micro-electronics", *IEEE-IAS Meeting*, Edmonton, Canada October 5-8 2008.
48. H. Sadek, A. Robinson, J. Cotton, C. Y. Ching, and M. Shoukri, "Electrohydrodynamic enhancement of an in-tube convective condensation heat transfer" *International Journal of Heat and Mass Transfer* **49**:1647-57, 2006.

49. J.T. Dickey and G.P. Peterson. "Experimental and analytical investigation of a capillary pumped loop" *Journal of Thermophysics and Heat Transfer*, **8**(3) : 602-607, 1994
50. J. M. Cimbala, J. S. Brenizer Jr., A. P. Chuang, S. Hanna, C. Thomas Conroy, A.A. El-Ganayni, and D. R. Riley, "Study of a loop heat pipe using neutron radiography", *Applied Radiation and Isotopes* **61**: 701–705, 2004.
51. J.G. Fantidis, G.E. Nicolaou, and N.F. Tsagas, "A transportable neutron radiography system based on a SbBe neutron source", *Nuclear Instruments and Methods in Physics Research A* **606**: 806–810, 2006.
52. International Fusion Research Council (IFRC), Status report on fusion research, *Nucl. Fusion* 45 pg. A1–A28, 2005.
53. B. Ghose and D.K. Kankane, "Estimation of location of defects in propellant grain by X-ray radiography", *NDT&E International* **41**:125–128, 2008.
54. X J Jiang, Z H Wang, H X Sun, X M Chen, T L Zhao, C Y Zhou, G H Yu, and L. Zhang, "Suitability analysis of commercial off-the-shelf components for space application", *Proc. IMechE* **220** Part G: J. Aerospace Engineering, 2006.
55. F. Kharfi, M. Bastuerk, and A. Boucenna, "Characterization of weak, fair and strong neutron absorbing materials by means of neutron transmission: Beam hardening effect", *Nuclear Instruments and Methods in Physics Research A* **565**:416–422, 2006.
56. P. Lamarque, "SRM improved X-rays examination: automatic detection in sight", *Acta Astronautica* **54**: 487 – 492, 2004.
57. J. Zhang, and K. Adamiak, "multi-species DC stationary model for negative corona discharge in oxygen; point-plane configuration", *Journal of Electrostatics* **65**:459-464, 2007
58. J. Maloney, "Space shuttle moves closer to liftoff", *NEWS*.
59. L Natalucci, P. Ubertini, A. Bazzano, E. Caroli, M. Federici, E. Quadrini, and R. Vittori, "High Performance, Low-Dose Radiography Systems for

- Space and Remote Site Applications”, *Wireless Pers Commun* **51**:725–737, 2009.
60. W.C. Priedhorsky and S.M. Ransom, “On-Orbit Radiography of Space Vehicles Using Natural Radiation”, *Proc. of SPIE* **5199**:99-110, 2003.
61. E.G. Riveros, “The digital radiographic and computed tomography imaging of two types of explosive devices”, *Applied Radiation and Isotopes* **57**: 861–865, 2002.
62. P. E. Underhill and R. L. Newacheck, “Miscellaneous Applications of Neutron Radiography”, *Practical Applications of Neutron Radiography and Gaging*, ASTM STP, American Society for Testing and Materials **586**:252-267, 1976.
63. K. Viswanathan, “Neutron radiography in Indian space programme”, *Nuclear Instruments and Methods in Physics Research A* **424**:113-115, 1999.
64. J. White, E.J. Tucholski and R.E. Green, “Nondestructive testing of aircraft and spacecraft wiring”, *Materials Evaluation* **61**:1315-1320, 2003.
65. M. Zawisky, F. Hameed, E. Dyrnjaja, and J. Springer, “Digitized neutron imaging with high spatial resolution at a low power research reactor: I. Analysis of detector performance”, *Nuclear Instruments and Methods in Physics Research A* **587**:342–349, 2008.
66. E. Grayzeck, “Planetary and Lunar Missions Under Consideration”, NASA, 2010. http://nssdc.gsfc.nasa.gov/planetary/prop_missions.html
67. J.S. Chang, “Two-phase flow in electrohydrodynamics” in part V of “Electrohydrodynamics”, *International centre for mechanical sciences courses and lectures – No.380*, A. Castellanos ed., Springer Wein, New York, pg. 279-349, 1998.
68. G.D Harvel, J.S. Chang, and V.S. Krishman, “Determination of time-dependent void fraction distribution of Bubbly two-phase flow by real-time neutron radiography techniques” *Journal of Nuclear Technology* **109**:132-141, 1995.

Appendix A: Future Space Missions

Currently there are several ongoing outer space operations being planned or undertaken by private organizations and public institutions such as NASA (USA), ISAS (Japan), and the ESA (European Union). NASA currently has deep space missions using ion propulsion spacecrafts with nuclear reactors, the Cassini spacecraft and the New Horizons spacecraft. Cassini reached its destination and is currently researching Saturn and its moons, while the New Horizons craft is on its way to Pluto and the Kuiper Belt [1, 4, 7, 56, 58-66].

Privately, space is also opening up to commercial interests. SpaceX has launched the first commercial satellite into orbit and is planning joint programs between public and private interests such as delivering goods to the International Space Station. Virgin Galactic hoping to make outer space the ultimate tourist destination is developing a manned spacecraft that will take tourists around the world in near orbit. The spacecraft is scheduled to launch around 2012 [1]. The X-prize foundation is an organization devoted to encouraging investment into developing non-government technology towards manned space flight. The X-prize has already awarded a multi-million dollar prize for the first non-government manned flight into space. Several other X-prizes are currently being offered. Google is offering a 30 million dollar X-prize for the first non-government developed robot on the moon. NASA lists a company SpaceDev that is developing a spacecraft for exploration of near earth asteroids. The project is called NEAP and will attempt to prospect asteroids for minerals [7, 56, 58-66].

Internationally, The ESA and ISAS are planning a joint mission to Mercury. NASA is planning several missions in the next year mainly to the International Space Station. Chapter A.1 lists the scheduled missions for the next year. NASA is also investigating a deep space mission to the Galilean moons of Jupiter that would use a nuclear reactor powered ion propelled spacecraft. China also is entering the space exploration game has launched a spacecraft to map the Moon and is considering attempting a manned moon mission [7, 66].

A.1 NASA's Shuttle and Rocket Launch Schedule

2010 Launches

Date: Nov. 5

Mission: [STS-133](#)

Launch Vehicle: [Space Shuttle Discovery](#)

Launch Site: [Kennedy Space Center](#) - Launch Pad 39A

Launch Time: 3:04 p.m. EDT

STS-133 Description: Space shuttle Discovery will deliver the Express Logistics Carrier 4 (ELC4), a MultiPurpose Logistics Module (MPLM) and critical spare components to the International Space Station.

Date: Nov. 19 *

Mission: [Commercial Orbital Transportation Services-1](#) (COTS-1)

Launch Vehicle: SpaceX Falcon 9

Launch Site: Launch Complex 40

Launch Window: 8:55 a.m. to 12:05 p.m. EST

Description: The first COTS test flight of the Falcon 9 rocket with the Dragon capsule atop will demonstrate key launch capabilities including on-orbit operation, entry, descent and splashdown of the capsule.

2011 Launches

Date: Feb. 23

Mission: [Glory](#)

Launch Vehicle: [Orbital Sciences Taurus Rocket](#)

Launch Site: [Vandenberg Air Force Base](#) - Launch Pad SLC 576-E

Launch Time: 2:10 a.m. PST/5:10 a.m. EST

Description: The Glory Mission will help increase our understanding of the Earth's energy balance by collecting data on the properties of aerosols and black

carbon in the Earth's atmosphere and how the Sun's irradiance affects the Earth's climate.

Date: Feb. 27 +

Mission: [STS-134](#)

Launch Vehicle: [Space Shuttle Endeavour](#)

Launch Site: [Kennedy Space Center](#) - Launch Pad 39A

Launch Time: 3:35 p.m. EST

STS-134 Description: Space shuttle Endeavour will deliver an EXPRESS Logistics Carrier-3 (ELC-3) and an Alpha Magnetic Spectrometer (AMS) to the International Space Station.

Date: June 9 *

Mission: [Aquarius](#)

Launch Vehicle: [United Launch Alliance Delta II 7320](#)

Launch Site: [Vandenberg Air Force Base](#) - SLC 2

Description: The Aquarius mission will provide the first-ever global maps of salt concentrations in the ocean surface needed to understand heat transport and storage in the ocean.

Date: Aug. 5

Mission: [Juno](#)

Launch Vehicle: [United Launch Alliance Atlas V](#)

Launch Site: [Cape Canaveral Air Force Station, Fla.](#)

Description: The solar-powered Juno spacecraft is to orbit Jupiter's poles 33 times to find out more about the gas giant's origins, structure, atmosphere and magnetosphere.

Date: Sept. 8

Mission: [GRAIL](#)

Launch Vehicle: [ULA Delta II Heavy](#)

Launch Site: [Cape Canaveral Air Force Station, Fla.](#)

Launch Times: 8:35:52 a.m. and 9:14:35 a.m. EDT

Description: The Gravity Recovery and Interior Laboratory mission's primary science objectives will be to determine the structure of the lunar interior from crust to core and to advance understanding of the thermal evolution of the moon.

Date: Oct. 18

Mission: [NPP](#)

Launch Vehicle: [ULA Delta II](#)

Launch Site: [Vandenberg Air Force Base, Calif.](#)

Description: The National Polar-orbiting Operational Environmental Satellite System Preparatory Project (NPP) mission for NASA and NOAA is to measure Earth's atmospheric and sea surface temperatures, humidity sounding, land and ocean biological activity and cloud and aerosol properties.

Date: Nov. 25 *

Mission: [Mars Science Laboratory](#)

Launch Vehicle: [United Launch Alliance Atlas V](#)

Launch Site: [Cape Canaveral Air Force Station](#)

Description: The Mars Science Laboratory is a rover that will assess whether Mars ever was, or is still today, an environment able to support microbial life and to determine the planet's habitability.

Appendix B: Electrohydrodynamic Equations and Theory

Table B.1 summarizes the fundamental equations for EHD and MHD induced motion as developed by J.S Chang [67]. The momentum and energy terms are identified for important multiphase systems and both conducting and non-conducting fluids. In addition, the conditions under which these terms have importance are identified.

Table B.1: Fundamental Equations for EHD and MHD Induced Motion

| Type of Fluid | | Momentum terms due to EMF: $\int_{\epsilon B}$ | Energy terms due to EMF: $q_{\epsilon B}'''$ | Comments |
|---|---------------------------|--|---|---|
| Non-Conducting Fluids ($I \rightarrow \text{small}$) | Gas Single Phase | $1/2 \epsilon_0 (\epsilon_S - 1) \nabla E^2 + 1/2 \mu_0 (\mu_S - 1) \nabla H^2$ | $\nabla \cdot (\bar{E} \times \bar{H}) + [\bar{E} \cdot d(\bar{D}/\rho)/dt + \bar{H} \cdot d(\bar{B}/\rho)/dt] \rho$ | $\mu_S = 1, \epsilon_S = 1$ $\nabla \epsilon \nabla \mu \rightarrow \text{small}$ |
| | Liquid Single Phase | $1/2 E^2 (\partial \epsilon / \partial T)_\rho \nabla T$ | (same as for gas) | $\rho \partial \epsilon / \partial \rho, \rho \partial \mu / \partial \rho$ $\nabla \mu \rightarrow \text{small}$ |
| | Gas-Liquid Two-Phase | $-1/2 E^2 \nabla \epsilon - 1/2 H^2 \nabla \mu$ (for each phase) $+ \nabla (1/2 E^2 \rho \partial \epsilon / \partial \rho + 1/2 \rho H^2 \partial \mu / \partial \rho)$ | (same as for gas but for each phase) | $\rho_v = \alpha_v \rho_v + (1 - \alpha_v) \rho_l$ $\epsilon_l, \mu_l \gg \epsilon_v, \mu_v$ |
| Conducting Fluids ($I \neq 0$) | Gas Single Phase | $\rho_e \bar{E} + \bar{J} \times \bar{B}$ $+ \nabla (1/2 E^2 \partial \epsilon / \partial \rho + 1/2 \rho H^2 \partial \mu / \partial \rho)$ | $\bar{J} \cdot \bar{E} + \nabla \cdot (\bar{E} \times \bar{H}) +$ $[\bar{E} \cdot d(\bar{D}/\rho)/dt + \bar{H} \cdot d(\bar{B}/\rho)/dt] \rho$ | $\rho_e \neq 0, \nabla \epsilon, \nabla \mu \rightarrow 0$ $\bar{J} = \bar{u} n \pm \mu' n \bar{E} - D \bar{\nabla} n$ |
| | Liquid Metal Single Phase | $\bar{J} \times \bar{B}$ | $\bar{J}^2 / \sigma_e + \nabla \cdot (\bar{E} \times \bar{H}) +$ $\rho \bar{H} \cdot d(\bar{B}/\rho)/dt$ | $\rho \partial \epsilon / \partial \rho, \rho \partial \mu / \partial \rho \rightarrow 0$ $\bar{J} = \mu \bar{E}, \rho_e = 0$ $\nabla \epsilon, \nabla \mu \rightarrow 0$ |
| | Liquid Single Phase | $\rho_e \bar{E} + \bar{J} \times \bar{B} + 1/2 E^2 (\partial \epsilon / \partial T)_\rho \nabla T$ | (same as for gas) | $\nabla \mu, \rho \partial \epsilon / \partial \rho, \rho \partial \mu / \partial \rho \rightarrow 0$ $\rho_e = \rho_+ - \rho_-$ |
| | Gas-Liquid Two-Phase | $-1/2 E^2 \nabla \epsilon - 1/2 H^2 \nabla \mu +$ $\nabla (1/2 \rho E^2 \partial \epsilon / \partial \rho + 1/2 \rho H^2 \partial \mu / \partial \rho)$ $+ \bar{J} \times \bar{B} + \rho_e \bar{E}$ (for each phase) | (same as for gas but for each phase) | $\bar{J}^* = \sigma \bar{E}^*$ $\bar{E}^* = \bar{E} + \bar{U} \times \bar{B}$ $\bar{H}^* = \bar{H} - \bar{U} \times \bar{D}$ |

Appendix C: Capillary Pumped Loop with EHD Enhanced Evaporator

The CPL experimental apparatus consists of a condenser with cooling jacket, EHD evaporator with heater bands, charging tank, a storage tank, connected piping and the associated instrumentation. A picture of the setup is present in Figure C.1.

In the figure the condenser, evaporator, tanks, piping and instrumentation is identified. The evaporator on closer inspection can be seen to consist of several further components. The outer shell of the evaporator is attached to the electrical heater bands, which provides the heat source for evaporation. The inside of the evaporator contains a stainless steel electrode, spring, Teflon plug and polyethylene wick. Figure C.2 displays the components of the evaporator.

Ultrasonic measurements are taken using the pulse-echo method. The method is explained in detail in Chapter 5. The ultrasonic receivers are placed on the condenser and the charging tank. The CPL experimental setup used an automated data acquisition system to record the remainder of the experimental data and is presented in the next Chapter.

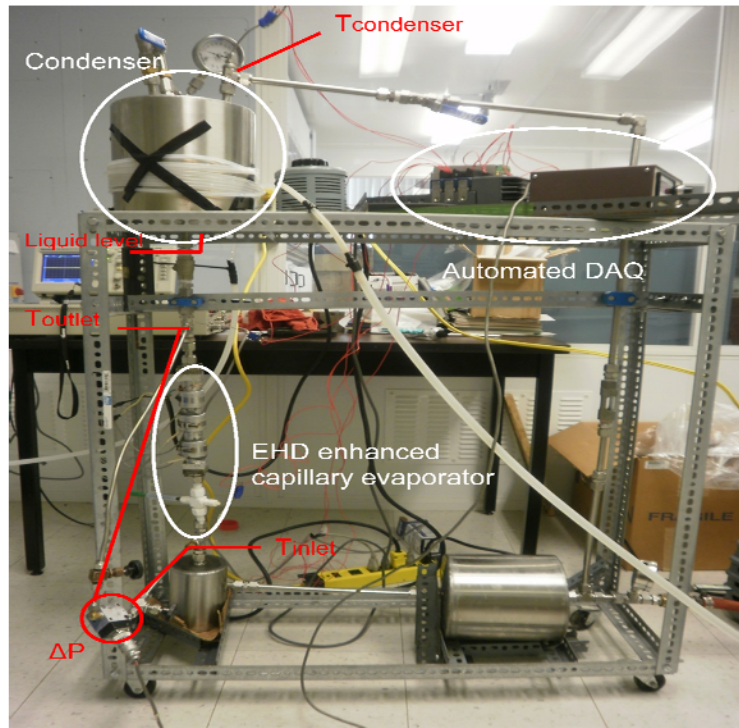


Figure C.1: Experimental Capillary Pumped Loop

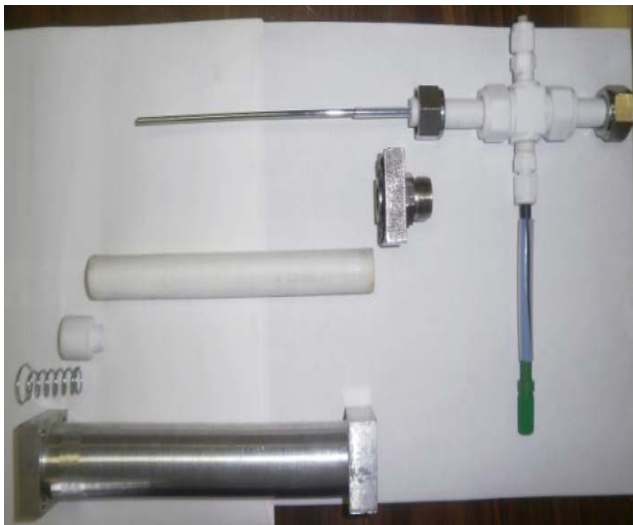


Figure C.2: Evaporator Components, Left) Electrode, End Cap, Wick, Teflon Plug, Spring and Metal Casing, Right) Assembled Evaporator with Heater Bands attached

Appendix D: Neutron Radiography Analysis

To better understand the unexpected weak performance of the CPL in previous work, the evaporator was taken to the McMaster Nuclear Reactor and placed in the dynamic neutron radiography facility in beam port 3. The shutter is opened remotely allowing a collimated neutron beam, with a flux of approximately 10^7 neutrons/cm²-s, to be in contact with the evaporator. After passing through the evaporator the unattenuated neutrons impinge upon a Li-doped ZnS neutron to photon converter [68]. A CCD camera is focused on the converter plate imaging a neutron radiograph of the evaporator in real-time. A diagram of the beam port is shown in Figure D.1, while a diagram of the test loop setup is displayed in Figure 4.5.

The evaporator was exposed to the neutron beam for two minutes. The activity of the evaporator and the beam port was measured by a meter located in the beam port. The evaporator was not activated during the experiment. The process is then repeated to produce a radiograph of the background. The neutron radiographs are recorded on DVD.

The DVD was then uploaded to a computer at UOIT. Then the HImage+ software was used to then take several still images of both the evaporator and the background radiograph. These images were then imported to MATLAB where a frame averaging program was used to average the images of each object together to produce one image of higher quality. The frame averaging program was created in MATLAB and is listed at the end of this Appendix in Chapter A.1. The frame averaged images are then transferred to Image Pro Plus 5.0 for image analysis. This part of the experiment involves the image capture and frame averaging performed at UOIT. The image capture from the DVD to the computer was effective. There was no noticeable loss in quality from the DVD to the computer. However, the image capture software did not have the ability to take several frames and save them at once. Each frame had to be save individually using a time consuming process. So, only 5 frames of each video

were captured. The 5 frames were then averaged together using a program created specifically for this experiment using MATLAB. The frame averaged image will have less noise and improve the quality of the radiograph when compared to a single frame. A still image is needed for image processing and analysis. The frame average program successfully produces frame averaged images of the background and evaporator. However, due to the limited amount of frames being averaged the noise was only slightly reduced when compared to the still frames. Still, there is a noticeable improvement in quality. In future a 100-1000 frames would be preferred to produce the best possible image. The program could be easily adapted to average that many frames.

The background image is subtracted from the evaporator image using a background correction with a black level of 15. The image then uses 3 passes of a 3x3 rank filter with a 0 threshold setting to sharpen the image. The image then undergoes a best fit equalization to optimize the contrast. Initial visual analysis of the image is now performed. Next, a Sobel filter edge detection technique is used to produce a new image to identify the edges of the object. Lastly, the image is compared to previous radiographs taken of the evaporator at the same beam port.

The initial visual inspection determined that both videos produced the expected images. The object in the evaporator radiograph is clearly identifiable. The images then underwent image analysis. The images were subtracted to produce a single image of the evaporator. The subtracted image then was processed using a rank filter and best fit equalization. The radiograph of the evaporator after image analysis is displayed in Figure D.2. The image processing techniques were used to further reduce the noise and improve the clarity and contrast in the image.

The processed radiograph then underwent a Sobel filter to help confirm the edges of the object. The Sobel filter image is displayed in Figure D.3. A line profile analysis of the radiograph is also used to determine the elimination of the

gap in the evaporator. The results of the line profile are presented in Figure D.4. The edge detection highlights the edges clearly displaying the outline of the evaporator.

The digital radiography performed at the McMaster Nuclear Reactor produced two radiographs of high-quality, however the date and time label was not removed during filming for the entire video of the evaporator. This was not discovered until the videos were uploaded at UOIT. So, the date and time then appears in the processed image of the evaporator. However, this did not affect the results of the experiment as the label does not interfere or reduce the visibility of the object in the image. Also, the evaporator was able to be safely radiographed without activation. This was expected due to previous radiographs having never caused any activation of the evaporator, the material composition of the evaporator (steel, Teflon and polyethylene), and the short exposure time. As such the experimental design of the radiography at McMaster is considered effective and can be used for future dynamic radiography of the EHD evaporator.

Next the radiograph is analyzed and discussed as the experimental results are compared to those results to previous radiographs of the evaporator. The image is then processed using image analysis software. A rank filter was used to even further reduce noise and improve the clarity of the image. The noise appears on the radiography as white specks or streaks. In this case, no combination of filters or single filter that was attempted was found to reduce the noise any further than the rank filter did. However, the image quality would be improved by an improved image capture process. Regardless, the processed image produced a clear well contrasted image that is more than sufficient for the purposes of this experiment.

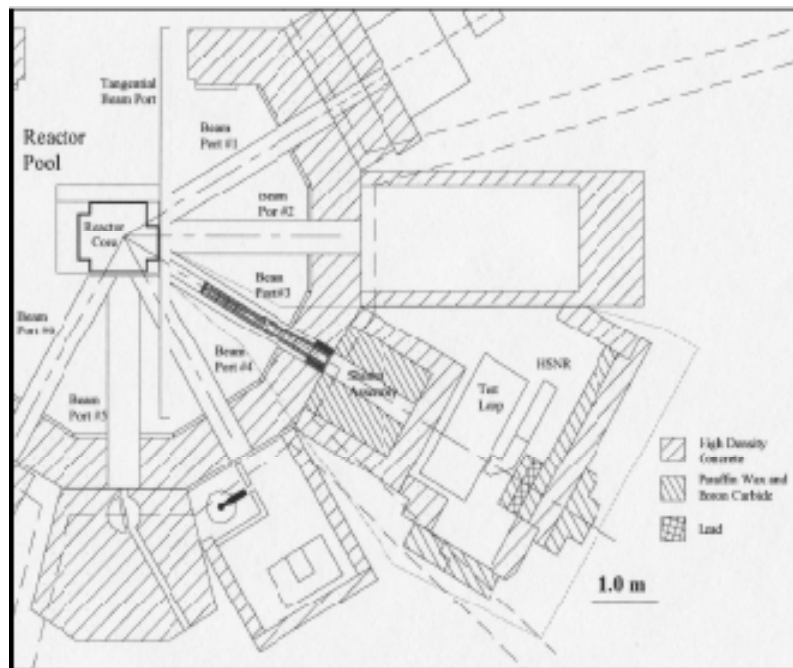


Figure D.1: Diagram of Beam Port 3



Figure D.2: Radiograph of evaporator after image analysis

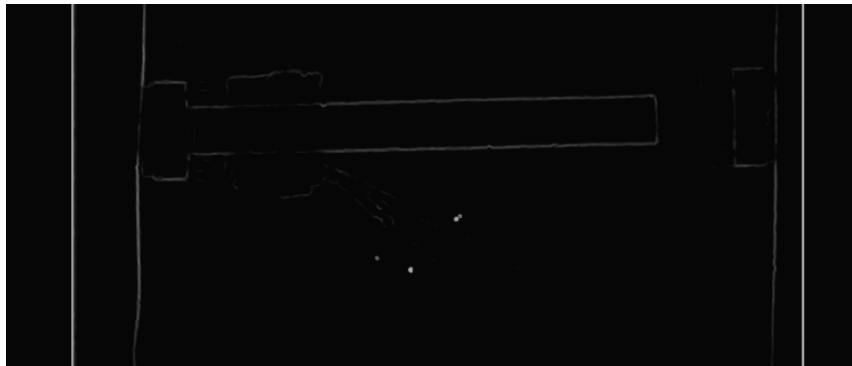


Figure D.3: Edge detection image of evaporator using a Sobel filter

D.1 Frame Average Program

The frame average program created for the neutron radiography analysis was generated in MATLAB to average the stills taken of the radiograph videos.

```
clc

%import background images as matrix

BG1a = imread('D:\My Documents\MATLAB\Radiography Picture\bg1.bmp');
BG2a = imread('D:\My Documents\MATLAB\Radiography Picture\bg2.bmp');
BG3a = imread('D:\My Documents\MATLAB\Radiography Picture\bg3.bmp');
BG4a = imread('D:\My Documents\MATLAB\Radiography Picture\bg4.bmp');
BG5a = imread('D:\My Documents\MATLAB\Radiography Picture\bg5.bmp');

%covert to double

BG1 = double(BG1a);
BG2 = double(BG2a);
BG3 = double(BG3a);
BG4 = double(BG4a);
BG5 = double(BG5a);

%evaporator images

EV1a = imread('D:\My Documents\MATLAB\Radiography Picture\ehdevap.bmp');
EV2a = imread('D:\My Documents\MATLAB\Radiography
Picture\ehdevap2.bmp');
EV3a = imread('D:\My Documents\MATLAB\Radiography
Picture\ehdevap3.bmp');
EV4a = imread('D:\My Documents\MATLAB\Radiography
Picture\ehdevap4.bmp');
EV5a = imread('D:\My Documents\MATLAB\Radiography
Picture\ehdevap5.bmp');

EV1 = double(EV1a);
EV2 = double(EV2a);
EV3 = double(EV3a);
```

```
EV4 = double(EV4a);  
EV5 = double(EV5a);  
%Averaging matrices  
BG = (BG1 + BG2 + BG3 + BG4 + BG5)/5;  
EV = (EV1 + EV2 + EV3 + EV4 + EV5)/5;  
%display images  
imshow(BG,[0,256])  
imshow(EV,[0,256])
```

Appendix E: Data Acquisition System

The data acquisition system (DAQ) is used to simultaneously measure and record the following parameters for the CPL experimental apparatus

- Differential Pressure (kPa)
- Temperature (°C)
- Time (s)

The program uses the cRIO FPGA to receive the data and then sends the information to the host program on the cRIO, which converts the data from voltage signals to the appropriate units and then records the data either onto its hard drive or to a flash drive in the form of a spreadsheet. The following diagram describes the program logic for the DAQ.

The program works in real-time with the cRIO and the computer but requires an interface to be able to start and stop the program. And therefore needs to be connected to a computer while in operation either wirelessly to the desktop in the lab or directly to a laptop, either the operator's laptop or a laptop specifically designated for data acquisition. It also allows for real-time changes to be made to the program during operation and reduces the time to edit and compile the program. Therefore, a computer must be open and running the program while the DAQ is in operation. The DAQ has the ability to connect wirelessly to the desktop in 1040 to measure and record data, however the preferred and current method in operation is to have a DAQ laptop installed with LabVIEW and the associated modules to use as an interface for the DAQ system. The backup files are be saved to the laptop, while the data spreadsheets saved to the USB flash drive and saved for analysis. Table E.1 describes the components of the DAQ. The program is displayed at the end of the Appendix.

The DAQ is able to accurately measure record time, temperature and pressure in real-time. Figures E.2 and E.3 demonstrate the response time and functionality of the DAQ. The experiment was performed where the pressure was varied using the pressure calibrator and was measured and recorded using the DAQ. Temperature was also measured and recorded simultaneously with the pressure. 3 thermocouples were used. 1 was held at room temperature, while the other two thermocouples were placed in beakers filled with water where they were heated and cooled by adding hot and cold water. The data is recorded in spreadsheet format and then transferred to excel and analyzed. The results clearly demonstrate the DAQ is functioning properly and able to record and measure data in the experimental loop.

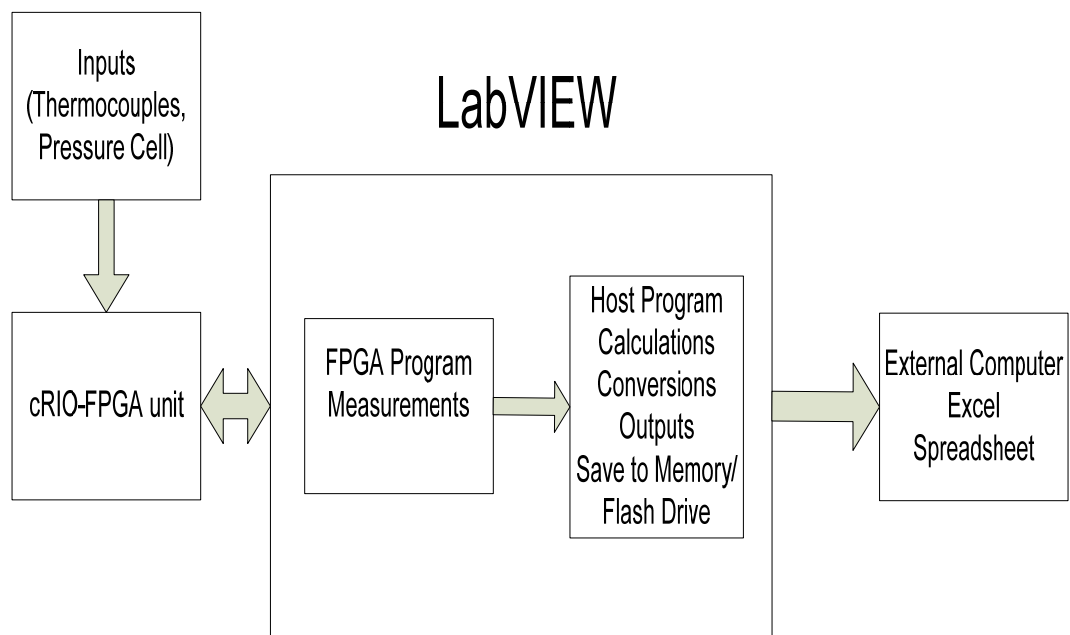


Figure E.1: Data Acquisition System for the CPL

Table E.1: Data Acquisition System Components

| Component | Manufacturer | Model | Description |
|--|--|-------------|---|
| Compact Reconfigurable Inputs Outputs (cRIO) | National Instruments (NI) | 9012 | -Real-time Field-Programmable Gates Array (FPGA) integrated -Eight sockets for I/O Modules |
| Power supply | Phoenix Connection | Quint Power | -Input: AC 100-240V -Output: DC 24V 5A |
| I/O Module | NI | 9215 | -2 units of Four \pm 10V simultaneous-sampling analog inputs/outputs (8 total) |
| I/O Module | NI | 9211 | -Four \pm 80mV thermocouple inputs |
| Thermocouple | Omega | C series | -Copper / constantan - -200 to 350 °C range |
| Pressure cell | Validyne Engineering Corporation (VEC) | DPI5TL | With a 13.8 kPa (2psi) ranged diaphragm |
| Demodulator | VEC | CD23 | |
| Pressure calibrator | Fluke | 719 100G | -Electrical pump integrated -Range: -82.7 to 689 kPa (-12 to 100psi) -Resolution: 0.01psi |

| | | | |
|----------------|-----|-------|--|
| | | | -Accuracy: $\pm 0.025\%$ of range |
| Computer | Any | Any | -Acts as cRIO interface |
| <i>LabVIEW</i> | NI | 8.6.1 | -Real-time and FPGA modules 8.6.1 on the computer and cRIO -cRIO driver: NI-RIO 3.3.4 |

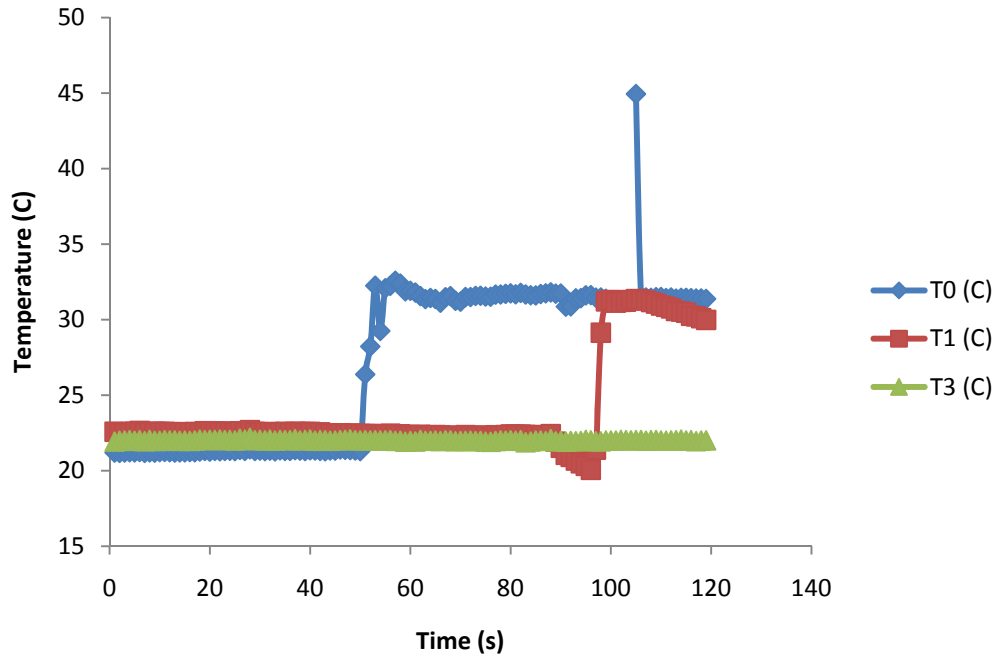


Figure E.2: Temperature vs. Time measured by the DAQ System

Note: spike from T0 is due to interference from when it came into contact with T3

Pressure vs Time using DAQ

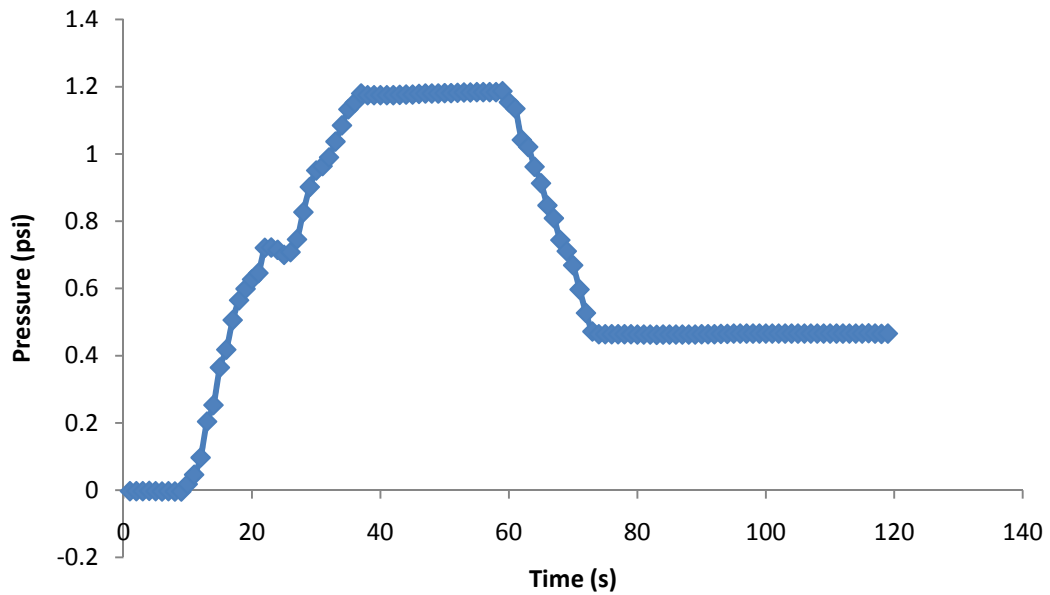
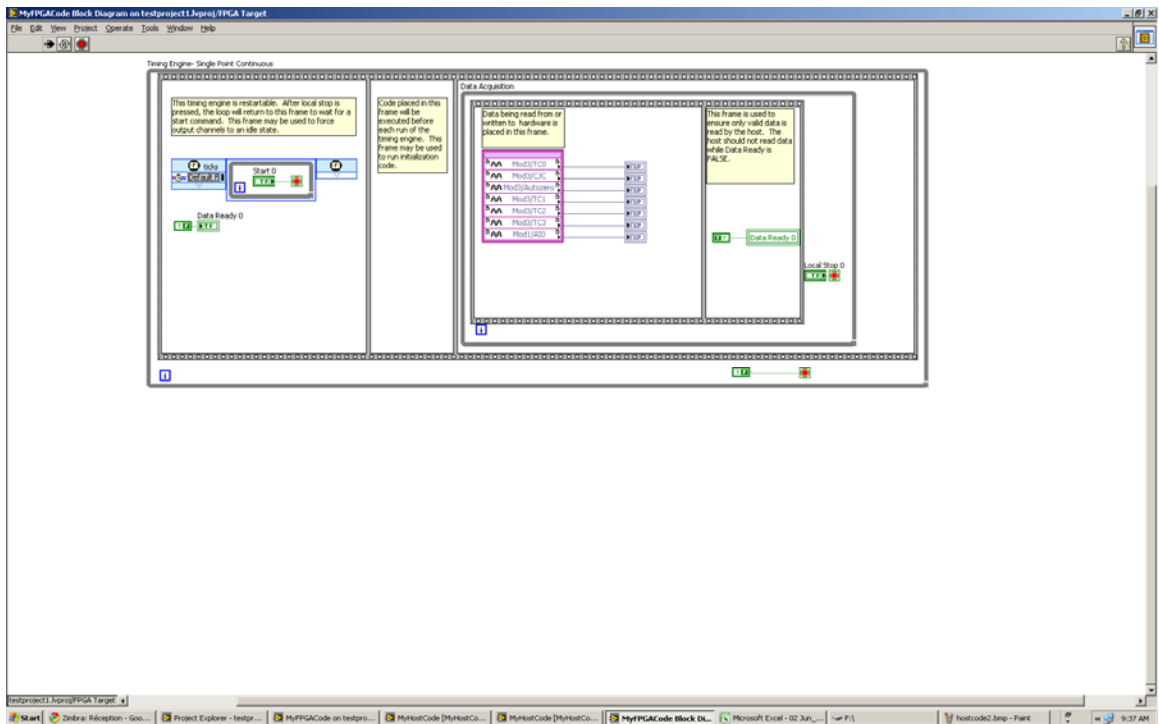
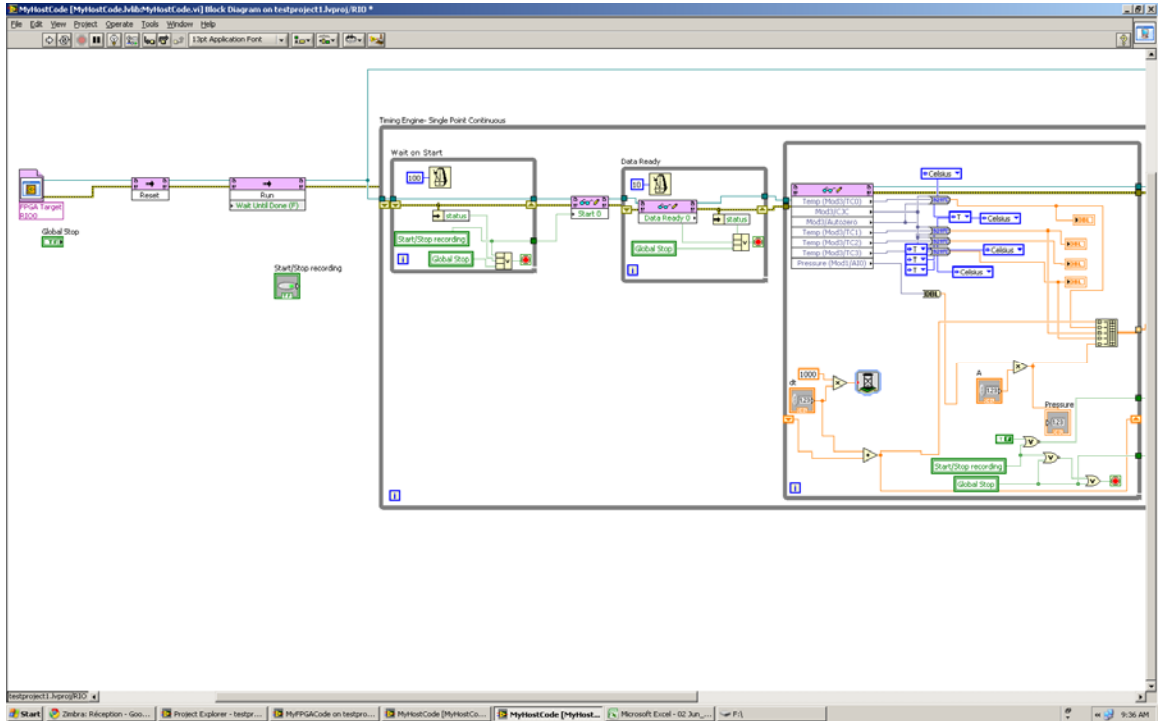
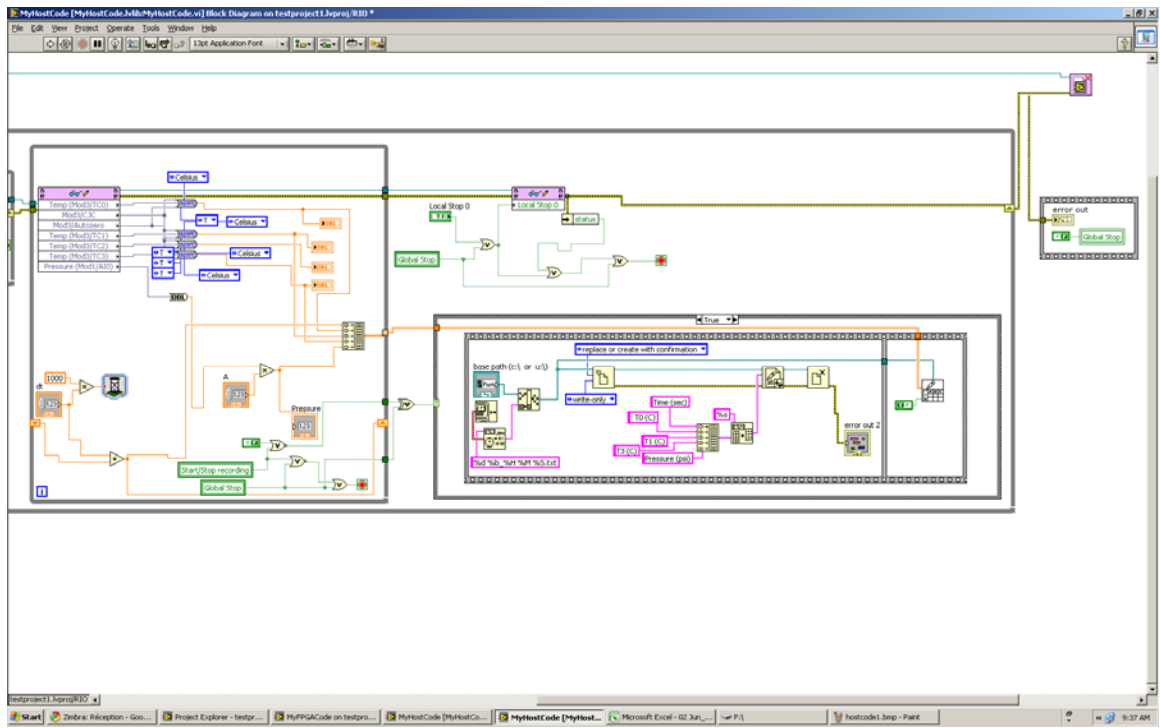


Figure E.3: Pressure vs. Time using the DAQ system

E.1 LabView DAQ Program





Appendix F: Freon 134a Properties

The working fluid of the experimental CPL Freon R134a, chemical name 1,1,1,2-Tetrafluoroethane ($C_2H_2F_4$), is a well documented refrigerant. The appendix characterizes the expected properties of Freon R134a for the CPL. The CPL will operate in temperatures of 19-25°C and in pressures of 350 - 550kPa. Both vapour and liquid will be present in the CPL. In these conditions, Freon will have the properties presented in Table F.1. Figure F.1 displays a R134a property figure relating pressure to enthalpy.

Table F.1: Expected Freon R134a Properties for Experimental CPL

| Property | Value |
|-------------------------------|------------------------|
| Density Liquid | 1203 kg/m ³ |
| Density Gas | 30 kg/m ³ |
| Thermal Conductivity Liquid | 0.0824 W/mK |
| Thermal Conductivity Gas | 0.0145W/mK |
| Viscosity Liquid | 200 uPas |
| Viscosity Gas | 11.7 uPas |
| Specific Heat Capacity Liquid | 1.42 kJ/kgK |
| Specific Heat Capacity Gas | 0.854 kJ/kgK |

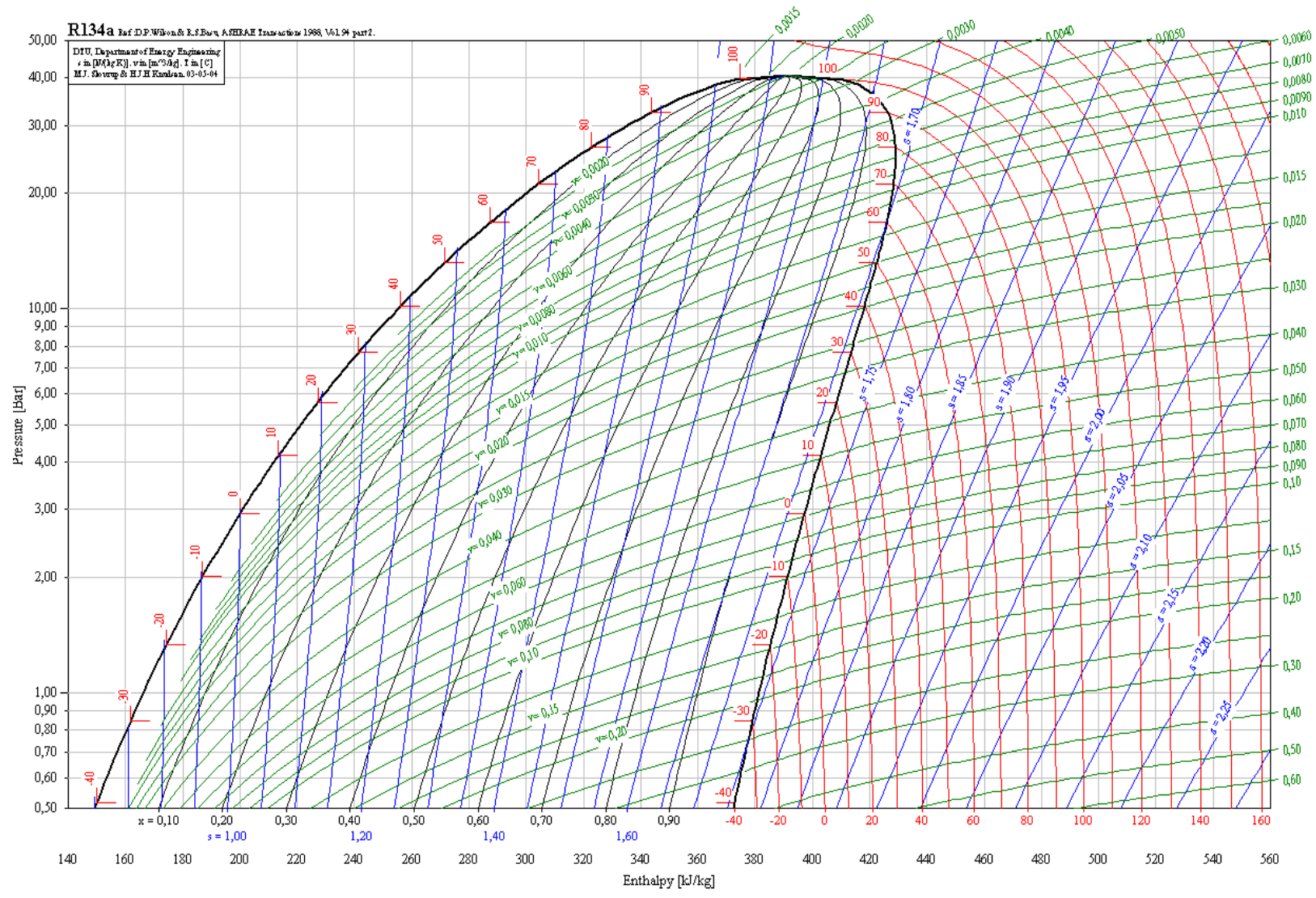


Figure F.1: Freon R134a Property Table

Appendix G: Publications and Presentations

1. A. Lipchitz & G. Harvel, "Characterization of electrohydrodynamic heat transport components in a space-type nuclear reactor", Canadian Nuclear Society Annual Conference, May 2010.
2. A. Lipchitz & G. Harvel, "Electrohydrodynamic Capillary Pumped Loop" Presentation to International Panel on Electrohydrodynamics, EHD Workshop, International Symposium on Non-Thermal Plasmas 7, July 2010.